Cell
Leading Edge

CellPress

Primer

Fluorescence imaging of large-scale neural ensemble dynamics

Tony Hyun Kim[1,2,3,*] and Mark J. Schnitzer[1,2,3,*]
[1]James Clark Center for Biomedical Engineering & Sciences, Stanford University, Stanford, CA 94305, USA
[2]*CNC* Program, Stanford University, Stanford, CA 94305, USA
[3]Howard Hughes Medical Institute, Stanford University, Stanford, CA 94305, USA
*Correspondence: kimth@stanford.edu (T.H.K.), mschnitz@stanford.edu (M.J.S.)
https://doi.org/10.1016/j.cell.2021.12.007

SUMMARY

Recent progress in fluorescence imaging allows neuroscientists to observe the dynamics of thousands of individual neurons, identified genetically or by their connectivity, across multiple brain areas and for extended durations in awake behaving mammals. We discuss advances in fluorescent indicators of neural activity, viral and genetic methods to express these indicators, chronic animal preparations for long-term imaging studies, and microscopes to monitor and manipulate the activity of large neural ensembles. Ca^{2+} imaging studies of neural activity can track brain area interactions and distributed information processing at cellular resolution. Across smaller spatial scales, high-speed voltage imaging reveals the distinctive spiking patterns and coding properties of targeted neuron types. Collectively, these innovations will propel studies of brain function and dovetail with ongoing neuroscience initiatives to identify new neuron types and develop widely applicable, non-human primate models. The optical toolkit's growing sophistication also suggests that "brain observatory" facilities would be useful open resources for future brain-imaging studies.

INTRODUCTION

Over the past century, neuroscientists chiefly relied on electrophysiological recording techniques to monitor neuronal spiking dynamics in live animals. Soon after green fluorescent protein (GFP) emerged as the first genetically encodable fluorescent marker (Chalfie et al., 1994), neuroscientists and protein engineers began to create genetically encodable fluorescent indicators of neuronal Ca^{2+} and voltage activity (Siegel and Isacoff, 1997). Since then, neuroscience has witnessed an explosive growth of optical indicators and imaging techniques that has enabled studies of neural ensemble dynamics in hundreds to thousands of individual neurons in behaving mammals, with imaging studies of even more neurons likely coming soon (Demas et al., 2021).

The expanding capabilities for large-scale neural recordings have opened new possibilities to study the coding and computational properties of neural populations, rather than of individual cells (Yuste, 2015). Unlike in years past, the number of neurons that can now be imaged concurrently in behaving animals far surpasses the dimensionality of the sensory, cognitive, or motor tasks that are typically used in neuroscience experiments. This technical achievement has created unprecedented experimental opportunities to explore the fundamental principles by which large population of neurons represent and transform behaviorally relevant variables through their collective dynamics (Jazayeri and Ostojic, 2021) as well as a need for new theoretical frameworks and analytic methods to evaluate the high-dimensional recordings (Gao and Ganguli, 2015).

For such studies of neural dynamics, large-scale optical recordings routinely exceed the numbers of cells that can be monitored simultaneously by cutting-edge electrophysiological methods (Steinmetz et al., 2021). Optical imaging can also provide information about brain activity that remains infeasible or very challenging to obtain with electrical approaches. Specifically, with optical methods one can record activity in dense sets of neurons selected by their genetic identities or axonal projection patterns; reveal sub-cellular neural dynamics, such as in axons, dendrites, or spines (Cornejo et al., 2021); monitor cells that are too quiescent or have insufficient electric dipole moments to record with extracellular electrical recordings; and track large numbers of cells for weeks to months for time-lapse studies, such as of learning and memory, brain development, aging, or disease progression (Hamel et al., 2015; Jercog et al., 2016). It has even become possible to image the dynamics of extracellular neurotransmitter and neuromodulator levels in behaving animals (Patriarchi et al., 2018; Sabatini and Tian, 2020).

This is not to say that optical imaging obviates the need for electrical methods in neuroscience. To the contrary, electrical recording techniques are also progressing and allow certain recording geometries, such as those obtainable with penetrating electrodes, that optical methods cannot yet match. To this point, electrophysiological studies can readily sample neural activity in multiple brain areas in freely moving animals. While the introduction of head-mounted miniature microscopes brought many advantages of imaging to studies in freely moving animals (Flusberg et al., 2008; Ghosh et al., 2011; Helmchen et al., 2001), such

experiments have used one or at most two mini-microscopes (de Groot et al., 2020) that each image a single brain area. On the other hand, novel fluorescence mesoscopes have emerged recently for imaging much of the cortical surface at cellular resolution in head-fixed rodents. Neuroscientists are still bringing this approach to full fruition, but it seems unlikely that electrical recordings will be able to sample single-cell activity patterns at a comparable density across the cortical mantle in the near future.

Until recently, electrical recordings retained clear superiority in the time domain, since the dominant method for imaging neural activity, fluorescence Ca^{2+} imaging, provides only an indirect and temporally low-pass filtered version of neural spiking dynamics. Rapid progress in voltage imaging is challenging this superiority by providing optical traces of membrane potential dynamics in genetically or projection-targeted neuron types with sub-millisecond spike-timing precision and sensitivity to subthreshold voltage activity. Nevertheless, high-speed voltage imaging studies of neural spiking still have small fields of view (FOVs) due to limitations in instrumentation and short recording durations due to indicator photobleaching, but the technology is progressing swiftly.

An important strength of both Ca^{2+} and voltage imaging is their compatibility with other optical methods. For instance, the combination of either Ca^{2+} or voltage imaging with optogenetic approaches enables "all-optical physiology" studies that concurrently image and manipulate the same individual neurons with light (Emiliani et al., 2015). Other techniques that are naturally combined with *in vivo* optical brain-imaging include the use of photoactivatable fluorescent proteins or light-activated recombinases to mark cells of interest for post-mortem tracing or gene sequencing (Lee et al., 2019; Yao et al., 2020) as well as imaging-based immunohistological (Khan et al., 2018) or spatially resolved transcriptomic analyses in post-mortem brain slices (Close et al., 2021). These methods allow fine discriminations of different cell types and explorations of their gene or protein expression patterns; the combination of such methods with *in vivo* imaging of neural activity allows studies in which one first images the dynamics of individual neurons and then probes, e.g., RNA expression in the very same cells, to uncover relationships between the two cross-registered datasets (Xu et al., 2020). Overall, fluorescence imaging studies of neural activity are blossoming, and we expect continued progress in this area and further integration with other imaging-based technologies that provide complementary information.

This primer explains recent advances in fluorescence imaging of large-scale neural activity for readers new to the field. We focus exclusively on techniques that provide cellular resolution, with a predominant focus on imaging of the mammalian brain. We first present basic notions from signal detection theory that are helpful for understanding optical detection of neural activity. Next, we introduce fluorescent Ca^{2+} indicators, methods for expressing these indicators in specific neural populations, and animal preparations for large-scale imaging studies. Fluorescence microscopy has undergone many recent developments, and we assess state-of-the-art optical instrumentation for large-scale neural Ca^{2+} imaging studies, with emphasis on new methods for imaging across wider FOVs, at faster speeds, and to greater depths in brain tissue. We then examine the integration of two-photon Ca^{2+} imaging with two-photon optogenetic manipulations and describe recent progress in voltage imaging. Given the important role of primate species in ongoing neuroscience initiatives in several countries, we discuss optical imaging of the monkey brain. We conclude with some considerations for how the field may benefit from the establishment of "brain observatory" facilities that aim to engineer and integrate next-generation imaging techniques and to make the most sophisticated, state-of-the-art imaging methods openly available to neuroscience researchers.

NEURAL ACTIVITY IMAGING FROM A SIGNAL DETECTION PERSPECTIVE

The basic goal of neural activity imaging is to produce a record of the brain's physiological state and how it changes with time. Using various optical contrast mechanisms, different features of the brain state—e.g., ion concentrations, neural transmembrane voltages, levels of neurotransmitters or neuromodulators—can be encoded in optical signals. The task of the microscopist is to elicit and detect those signals and thereby to infer the underlying physiological dynamics. To benchmark the success or failure at this task, signal detection theory provides a framework by which one can quantitatively evaluate experimental capabilities for enabling proper inferences (Hamel et al., 2015; Sjulson and Miesenböck, 2007; Wilt et al., 2013).

By capturing the net effects of all the factors that influence optical detection—the attributes of a neural activity indicator, the fluorescence labeling pattern, and the capabilities of the microscope—signal detection theory shows how these factors affect imaging performance, enables principled comparisons of different indicators and instruments, and allows assessments of the statistical confidence with which one can infer neural activity patterns. Mathematically, signal detection theory treats the optical detection of a neural spike as an instance of hypothesis testing.

Given an optical measurement, namely a set of detected photons, the two hypotheses to be tested against each other are that these photons either do or do not represent a neural spike. The intrinsic stochasticity of photon generation and detection, often termed "photon shot noise," implies that, no matter how favorable the optical conditions, neither hypothesis can be ruled out absolutely. Thus, signal detection theory computes the relative likelihoods that the observed set of photons reflect a neural spike or not, taking into account the fluctuations from shot noise. By comparing the statistical distributions of these likelihood ratios across cases in which there actually is or is not a spike, the theory provides a statistical measure of the fidelity, known as d', with which one can correctly distinguish optical measurements that represent a spike from those that do not. Given an experimenter's willingness to tolerate a certain rate of false-positive detection events, d' sets the true-positive detection rate. Thus, d' characterizes the trade-off between false-positive and false-negative detection events (Hamel et al., 2015; Wilt et al., 2013).

Across a wide range of optical conditions, d' can be expressed in simple mathematical form. Given a cell from which photons are detected at a mean rate, F_0, when the cell is at rest, and

for which this rate increases by an amount, ΔF, at spike onset and then decays exponentially with time-constant, τ, d' is approximately $(\Delta F/F_0)\cdot\sqrt{F_0\tau/2}$ (Wilt et al., 2013). This expression has key implications. For instance, it shows that d' rises linearly with increases in the relative fluorescence change in response to a neural event, $\frac{\Delta F}{F_0}$, but only with the square root of increases in τ or the baseline fluorescence, F_0. Note that here $\frac{\Delta F}{F_0}$ is the measured change in fluorescence under real experimental conditions, not a value obtained from *in vitro* biochemical characterizations of an indicator; thus, labeling strategies that improve $\frac{\Delta F}{F_0}$, such as by reducing background fluorescence or mistrafficked indicator molecules, can substantially improve d'. Such considerations have motivated the use of sub-cellular protein targeting methods that reduce background fluorescence by confining Ca^{2+} or voltage indicator molecules to within or nearby the neuronal cell body, where neural-spiking-related signals are pronounced (Chen et al., 2020; Shemesh et al., 2020). By comparison, rises in d' from greater illumination intensity, improvements in photon capture efficiency, or prolonged fluorescence responses are muted by the square root. However, even modest improvements in d' can have an enormous effect on the quality of an optical study, because the rate of false-negative detection declines faster than exponentially with rises in d' (Wilt et al., 2013). This mathematical fact points to the importance of continued incremental improvements in optical indicators and instruments.

These considerations highlight different strengths and weaknesses of one- and two-photon fluorescence imaging for detecting neural activity. Since standard wide-field one-photon fluorescence microscopy uses a camera, it typically samples the fluorescence from each cell for nearly the entire interval between image frame acquisitions (e.g., ~30 ms for video-rate imaging). In laser-scanning two-photon microscopy, an individual cell is sampled for only a fraction of this interval—namely, when the laser sweeps across the pixels the cell occupies, which takes ~0.05–3 μs. This difference can lead to greater photon counts (F_0) in one-photon fluorescence imaging. On the other hand, since wide-field fluorescence microscopy lacks optical sectioning, background fluorescence from structures outside the focal plane is generally much higher than in two-photon microscopy, leading to diminished $\frac{\Delta F}{F_0}$ values for one-photon imaging under identical labeling conditions.

As an example for how these factors can interact, Wilt et al. (2013) reported comparable d' values for the detection of Ca^{2+} spikes in cerebellar Purkinje neurons with the two imaging modalities, but with $\frac{\Delta F}{F_0}$ values of ~30% for two-photon imaging and ~0.5%–1.5% for one-photon imaging, showing that the greater flux of detected photons per cell in one-photon imaging had compensated for its lesser dynamic range of signaling. In our own experience with Ca^{2+} imaging of multiple different neuron types, d' values for spike detection are often comparable between the two modalities, suggesting that such approximate compensation may be commonplace.

This discussion does not diminish the virtues of two-photon microscopy, which penetrates more deeply and provides images of greater contrast and finer spatial resolution in thick tissue than one-photon microscopy. The optical sectioning and volumetric imaging capabilities of two-photon microscopy can also make it easier to computationally extract individual neurons and their activity traces from raw videos of neural activity, whereas the background fluorescence in one-photon images can necessitate cell extraction algorithms that are robust to background contaminants and signals from out-of-focus cells (Inan et al., 2021). Nevertheless, users of one-photon Ca^{2+} imaging should be reassured that d' values for spike detection are generally comparable to those from two-photon Ca^{2+} imaging.

INTRODUCTION TO FLUORESCENT CA^{2+} INDICATORS OF NEURAL ACTIVITY

As several reviews cover Ca^{2+} indicators (Grienberger and Konnerth, 2012; Lin and Schnitzer, 2016; Rose et al., 2014), it is not our aim to discuss this topic in depth. Rather, we seek to provide basic information that will make the rest of this primer accessible and aid the use of these indicators by readers who are new to optical methods.

Many past studies examined the brain's intrinsic optical signatures of neural activation or used synthetic fluorescent reporters of neural activity, but today most imaging studies of neural activity use genetically encoded indicator proteins that modulate their fluorescence signals in response to chemical or electrical events in the brain. Fluorescence Ca^{2+} imaging, which can track forms of neural excitation that alter intracellular [Ca^{2+}] levels, is the most widely used optical method to image neural activity. Over the past decade, the signaling dynamic range and response kinetics of genetically encoded Ca^{2+} indicators (GECIs) have improved substantially. Along with new methods for delivering these indicators and microscopes for imaging large ensembles of individual cells (see following sections), advancements in GECI performance have propelled studies of neural population dynamics.

Neurons' resting intracellular [Ca^{2+}] levels are very low (~50–100 nM), but [Ca^{2+}] rises during a variety of neuronal events, many of which have been studied extensively. For instance, in presynaptic terminals Ca^{2+} influx triggers neurotransmitter release, and in dendritic spines Ca^{2+} influx contributes to postsynaptic depolarization (Grienberger and Konnerth, 2012). Given the focus here on large-scale neural activity, we are chiefly concerned with somatic [Ca^{2+}] rises that accompany action potentials. Due to voltage-gated Ca^{2+} channels in nearly all neuron types, membrane depolarization during an action potential leads to an increase in somatic [Ca^{2+}] up to the ~1 μM range. GECIs report this rise via changes in their photophysical attributes. To accomplish this, GECIs generally comprise a Ca^{2+}-binding protein fused to one or more fluorescent proteins. Binding of one or more Ca^{2+} ions to a GECI alters its light absorption spectrum, fluorescence quantum yield, emission spectrum, or a combination thereof, leading to detectable changes in emission intensities, or absorption or emission wavelengths. GECIs are typically insensitive to hyperpolarization of the cell membrane below its resting potential, as this usually does not cause large reductions in cytosolic [Ca^{2+}], but they can report a reduction in a neuron's rate of spiking due to the accompanying reduction of depolarization-induced Ca^{2+} influx. For more background on the different forms of Ca^{2+} excitation, how they vary across distinct neuron types, and biochemical mechanisms for coupling

Ca^{2+} binding to fluorescent changes, we refer readers to the reviews noted above.

Most recent neural Ca^{2+} imaging studies use a GECI from the GCaMP family of indicators (Nakai et al., 2001), of which there is now an eighth generation (GCaMP8) (Zhang et al., 2021). GCaMPs constitute a Ca^{2+}-binding calmodulin domain and a Ca^{2+}/calmodulin-binding domain that are fused to opposite termini of a circularly permuted GFP. GCaMPs generally increase their fluorescence intensity monotonically as a function of cytosolic [Ca^{2+}], but there are also a few GECIs in the GCaMP family that dim at higher [Ca^{2+}] (Inoue et al., 2019). Red spectral variants, such as RCaMP, R-GECO, and XCaMP-R, substitute the GFP with a red fluorescent protein (Dana et al., 2016; Inoue et al., 2019; Zhao et al., 2011). There are also blue, yellow, and infrared GECIs (Mohr et al., 2020; Qian et al., 2019; Shemetov et al., 2021). The green fluorescent Ca^{2+} indicators generally perform the best, but having these other color options allows users to simultaneously image the Ca^{2+} activity of distinct cell types in different colors or to choose GECIs that are spectrally compatible with other indicators or actuators used in their experiment.

Within recent generations of GCaMPs, there are versions with distinct kinetics, dissociation constants of Ca^{2+} binding, and fluorescence levels when bound or unbound to Ca^{2+} (Dana et al., 2019). These parameters shape fluorescence waveforms in response to one or more neural spikes, although the neuron's own Ca^{2+} excitation, buffering, and clearance mechanisms are also important influences. Ca^{2+} physiology varies substantially across different neuron types, but nonetheless fluorescence waveforms from spiking activity are nearly always subject to an important trade-off between GECI sensitivity and speed. Namely, a GECI that binds Ca^{2+} more tightly will be more sensitive to the [Ca^{2+}] changes from single spikes, but the resulting optical waveform will decay more slowly. A longer decay time-constant, τ, provides more photons for detection but also implies that Ca^{2+} activity traces are subject to greater temporal low-pass filtering of the neuron's underlying spike train. In the GCaMP8 generation, waveforms corresponding to single spikes have rise times of ~10 ms and decay times of ~50–200 ms (Zhang et al., 2021), whereas the previously widely used GCaMP6 GECIs have rise and decay times of ~50–200 ms and ~150–500 ms, respectively (Chen et al., 2013). In an imaging experiment, the decay time-constant and the frame acquisition time both limit the temporal resolution of the acquired Ca^{2+} activity traces. However, frame rates faster than the indicator decay time-constant are helpful for avoiding aliasing, as dictated by the Nyquist sampling criterion, and for post hoc computational corrections for brain motion during imaging. When optimizing spike-timing estimation, the rise time-constant becomes the more important limiting factor, and a modest level of super resolution in the temporal domain is attainable by using fast frame rates (Wilt et al., 2013).

In addition to GECI kinetics, the temporal resolution of Ca^{2+} readout is also affected by intracellular [Ca^{2+}] buffering (Helmchen et al., 1996). They both delay the peak of a Ca^{2+} transient relative to the spike or spike burst that evoked the transient, and the individual spikes in a burst are usually hard to discern from Ca^{2+} activity traces. Instead, the number of spikes in a burst is approximately reflected in the Ca^{2+} transient amplitude, although there is still considerable variability due to the stochasticity of intracellular Ca^{2+} dynamics, fluorescence emission, and photon detection. Thus, making precise deductions about the number of spikes that gave rise to an observed Ca^{2+} transient is usually challenging, especially in cells with high baseline rates of spiking, such as fast-spiking interneurons (Rupprecht et al., 2021). Other imperfections in how spike trains are conveyed stem from the nonlinear relationship between [Ca^{2+}] and fluorescence intensity. For instance, [Ca^{2+}] levels much above the GECI's binding constant lead to saturation effects, resulting in prolonged fluorescence waveforms in response to large bursts of spikes that elicit high [Ca^{2+}] levels. Moreover, many members of the GCaMP family have Hill coefficients for Ca^{2+} binding that are greater than unity, which makes them less sensitive to one or a few spikes but amplifies their responses to larger bursts (Rose et al., 2014) (discussed further below; see also Figure 4C). An advantage of the X-CaMP variants is their Hill coefficient of one (Inoue et al., 2019), which aids detection of isolated spikes and facilitates analyses of Ca^{2+} activity traces that deconvolve the indicator's response toward estimating the constituent spikes and their precise times of occurrence in the underlying spike train. Notwithstanding the above nonlinearities, the expression $d' \approx (\Delta F/F_0) \cdot \sqrt{F_0 \tau/2}$ from signal detection theory still provides useful guidance for how different GECI attributes impact Ca^{2+} event detection.

In addition to indicators of Ca^{2+}, there are also fluorescent indicators of neurotransmitter and neuromodulator release. Indicators of extracellular glutamate, GABA, acetylcholine, dopamine, norepinephrine, serotonin, cannabinoid concentrations are now available and have been used in live animals (Dong et al., 2021; Sabatini and Tian, 2020; Unger et al., 2020; Wang et al., 2018a). Novel combinations of a GECI and another spectrally compatible indicator open up the possibility of jointly monitoring the release of neurotransmitters and neuromodulators and their effects on recipient neural populations (Patriarchi et al., 2020; Sun et al., 2020). Looking ahead, we expect further expansion of the spectral palette of GECIs and other indicators, better computational methods to infer spike trains from Ca^{2+} activity (Rupprecht et al., 2021), and next-generation GECIs with more favorable trade-offs between speed and sensitivity (Zhang et al., 2021).

GENETIC EXPRESSION OF MOLECULAR TOOLS FOR LARGE-SCALE OPTICAL STUDIES

Optical studies using genetically encoded indicators of neural activity or optogenetic actuators often require uniform expression of these tools over broad areas of tissue, at levels that are stable over the long term, while also minimizing side effects that impair cell or animal health. There are transgenic and viral approaches to satisfy these criteria as well as hybrid strategies.

In general, an advantage of transgenesis is the consistency of gene expression across cells and animals, whereas with viral injections it can be hard to reproduce precisely the anatomic site and number of viral particles injected. The relative uniformity and predictability of gene expression across transgenic animals of the same line facilitates complex imaging studies, improves

reproducibility, and allows systematic evaluations of indicator performance (Daigle et al., 2018; Huang et al., 2020). By comparison, viral methods for gene expression reduce or eliminate the need to maintain transgenic animal colonies, can be selectively targeted to neurons with specific axonal projection patterns, and are readily adaptable for use with new molecular tools. Hybrid strategies can make use of the advantages of both approaches, for example, to combine the cell-type specificity of a well-characterized transgenic line with the convenience of being able to quickly evaluate different virally expressed neural activity indicators.

Although many viral labeling methods have recently emerged, transgenesis remains a potent way to express molecular tools. Knock-in transgenic mice have steadily become easier and cheaper to create, and many academic and commercial services exist to make customized mice. Further, there are several widely applied mouse genetic systems that use site-specific DNA recombinases to express transgenes by crossing driver and reporter mouse lines in a modular fashion (Figure 1A). Driver mouse lines express the recombinase under the control of a specific promoter; reporter lines enable recombinase-dependent expression of a molecular tool. By crossing driver and reporter lines, one can easily create a transgenic mouse to express the tool via the selected promoter (Figure 1A, inset). This modularity permits a diverse array of molecular tools to be expressed in many different genetically defined neural populations (Daigle et al., 2018; Gerfen et al., 2013; Madisen et al., 2015; Taniguchi et al., 2011). When a new molecular tool arises, a single reporter line can be made to express the tool when crossed to any of the extant driver lines. Conversely, each driver line can be crossed with many different reporter mice, allowing a broad range of experiments.

Presently, the two most commonly used mouse genetic systems are those based on the Cre- or Flp-recombinases, although other recombinases are also used (Fenno et al., 2020). Initially, the inefficiency of Flp recombinase in mammalian cells slowed its adoption; today, mouse-optimized variants of Flp can achieve recombination efficiencies comparable to that of Cre (Raymond and Soriano, 2007). For neuroscience studies, many reporter mouse lines exist for Cre- or Flp-dependent expression of fluorescent indicators or optogenetic actuators (Figures 1A–1C) (Daigle et al., 2018). For concurrent imaging and control of neural activity, two reporter lines can be crossed to express an indicator and an opsin in one brain area (Figure 1C). To enable gene expression in more than one cell class, a reporter line can be jointly crossed with more than one driver line, such as for concurrent Ca^{2+} imaging of multiple cell types in a pair of areas (Wagner et al., 2019). There are also intersectional strategies in which transgene expression is dependent on the action of more than one recombinase (Fenno et al., 2020). In addition to transgenic mice, there are also transgenic rats (Scott et al., 2018) and marmosets that express GCaMP (Park et al., 2016), but to date most Ca^{2+} imaging and optogenetics studies in monkeys have relied on viral expression methods (Bollimunta et al., 2021; Kondo et al., 2018; Nandy et al., 2019).

Among viral techniques, the most common involve vector forms of adeno-associated virus (AAV), which comes in multiple serotypes with varying tropism for different cell types (Bedbrook et al., 2018; Haery et al., 2019). Until recently, AAVs were typically used for gene delivery near the site of virus injection. However, directed evolution of AAV capsids has yielded new serotypes with improved transduction and novel trafficking properties, which can efficiently deliver transgenes across large volumes of the mammalian brain. For example, AAV-PHP.eB is a derivative of AAV9 that efficiently crosses the blood-brain barrier following intravascular injection (Figure 1D) (Chan et al., 2017), providing a convenient way to express novel indicators throughout multiple regions of the rodent brain (Allen et al., 2017).

For studies of intercommunication between brain areas, viral labeling can target neurons via their axonal projection patterns (Figure 1E). For instance, the serotype AAV2-retro was evolved from AAV2 for enhanced uptake at axon terminals and retrograde transport to neural cell bodies (Tervo et al., 2016). Earlier approaches for retrograde targeting, such as rabies (Wickersham et al., 2007) or canine adenovirus (CAV) (Soudais et al., 2001), often were more toxic, harder to manufacture, or had reduced labeling efficiency in many neuron types. There are now less toxic rabies variants for expressing a Cre-recombinase (Chatterjee et al., 2018). There are fewer options for anterograde viral labeling, but AAV1 expressing Cre-recombinase can target neurons in an anterograde transsynaptic manner (Zingg et al., 2017). Direct, AAV1-driven expression of the indicator or actuator may not work as well, but the use of AAV1 as a way to achieve transsynaptic anterograde labeling remains promising, due to the wide availability of viral constructs and transgenic animals designed to allow Cre-dependent gene expression.

In the mouse, strategic combinations of viral and transgenic gene expression methods have become commonplace. For instance, injection of a Cre-expressing retrograde virus into GCaMP reporter mice can enable studies of somatic Ca^{2+} activity in neurons with a defined axonal projection pattern (Chatterjee et al., 2018). Alternatively, driver mouse lines allow cell-type-specific expression of virally delivered molecular tools; for example, injection of an AAV-PHP.eB reporter virus into Cre driver mice allows brain-wide expression of new indicators or opsins for which suitable reporter mouse lines are not yet available. To target neurons via both connectivity and genetic identity, one can inject a AAV2-retro virus into a Cre driver line to label neurons with a particular axonal projection in a Cre-dependent manner (Figure 1F).

Overall, there are established transgenic, viral, and hybrid techniques for brain-wide expression of molecular tools in neural populations defined by one or more facets of their genetics or connectivity. We anticipate that new expression methods will provide even greater specificity, such as via genetic enhancers (Blankvoort et al., 2018; Graybuck et al., 2019) and sophisticated intersectional approaches (Fenno et al., 2020), plus improved applicability of such methods to mammalian species beyond mice (see section below on primates).

ANIMAL PREPARATIONS FOR *IN VIVO* OPTICAL BRAIN IMAGING

Skin, bone, and overlying brain tissue impede light delivery and propagation due to scattering, absorption, and wavefront distortions. Thus, cellular-resolution imaging in the live brain usually

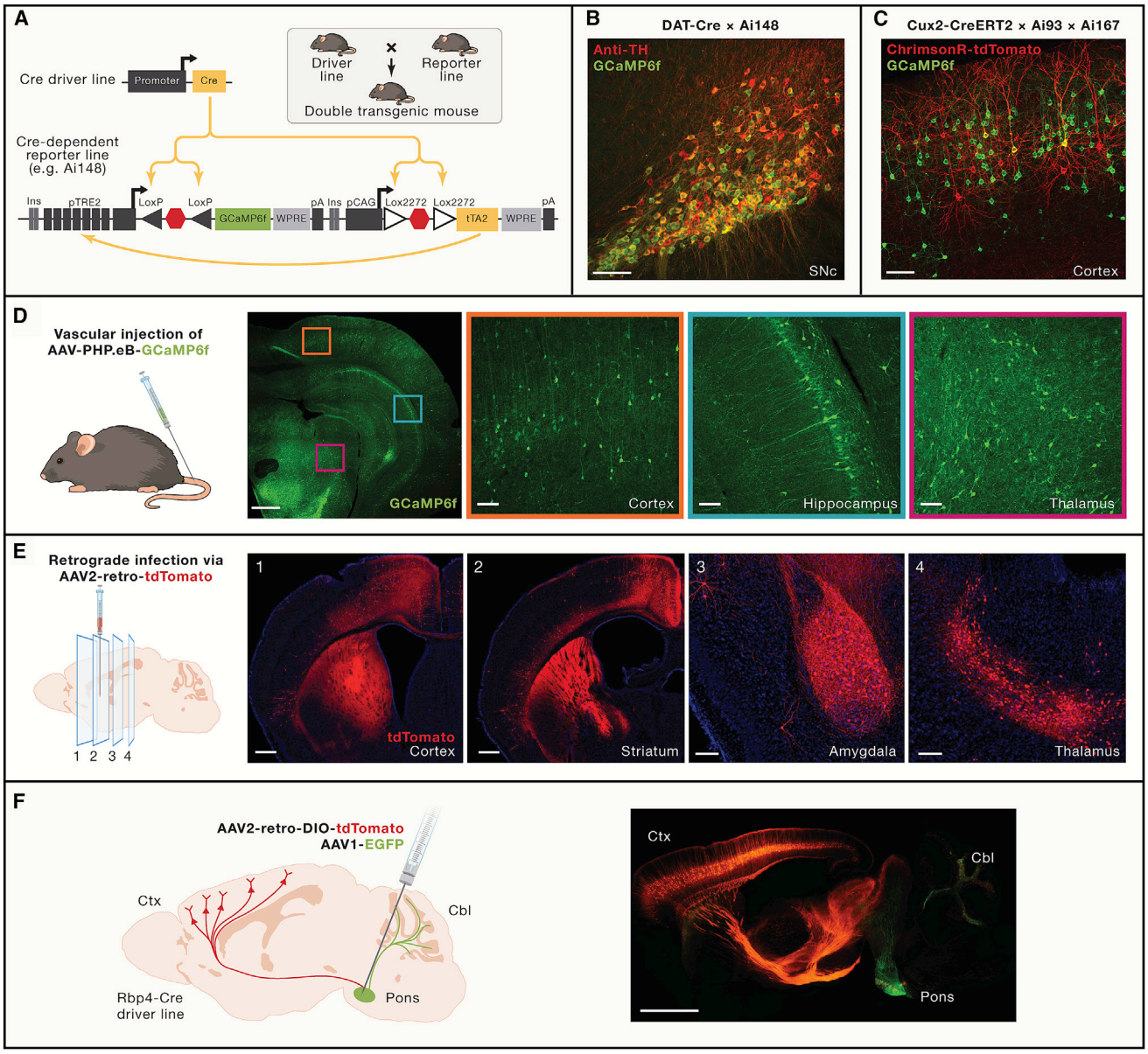

Figure 1. Viral and transgenic techniques for labeling neurons across the mammalian brain

(A) The TIGRE2.0 mouse transgenic strategy can achieve bright expression of a fluorescence label in a chosen cell class via the use of a genetic reporter construct that expresses both the fluorophore and a transactivator to amplify expression. The diagram illustrates this for a double transgenic that expresses the Ca^{2+} indicator, GCaMP6f, in a Cre-recombinase-dependent manner using the Ai148 reporter mouse line from the Allen Institute for Brain Science. Cre-recombinase is expressed via a selected genetic promoter (top) and then excises two different *lox-stop-lox* sequences in the reporter construct (bottom). After excision, the tetracycline-regulated transactivator (tTA2) binds to the Tet-responsive element (pTRE2) and drives amplified transcription of GCaMP6f.

(B) Example fluorescence image showing dopamine neurons of the substantia nigra pars compacta (SNc) from a double transgenic mouse that is a cross of the DAT-Cre driver line (DAT, dopamine transporter) and the TIGRE2.0 GCaMP6f reporter mouse line (Ai148, shown in A). Fluorescence immunostaining (anti-TH; red) confirms selective expression of GCaMP6f (green) within dopaminergic neurons. Scale bar, 100 μm. TH, tyrosine hydroxylase.

(C) By crossing more than two transgenic mouse lines, one can express both a fluorophore and an optogenetic actuator. To illustrate, the image shows a neocortical slice from a triple transgenic mouse that is a cross of the Cux2-CreER^{T2} driver line, which targets layer 2/3 cortical pyramidal neurons, and two different reporter mouse lines that conditionally express GCaMP6f (green; Ai93 line) and the red-shifted opsin ChrimsonR (red; Ai167 line). Only a few cells express both constructs (yellow cells). Scale bar, 100 μm.

(D) Left: a recently developed form of adeno-associated virus, AAV-PHP.eB, crosses the blood-brain barrier in many rodent strains and thus enables genetic targeting of neurons across the brain following intravascular virus injection. Diagram depicts injection of AAV-PHP.eB into the tail vein. Right: fluorescence immunostaining reveals brain-wide expression patterns of the Ca^{2+} indicator, GCaMP6f, in a coronal section of the rat brain containing neocortex, hippocampus, and thalamus. Colored boxes atop the brain section enclose areas that are magnified at right. Scale bars, 1 mm and 100 μm in the low- and high-magnification images, respectively.

(E) Left: retrograde viral labeling methods allow targeting of neurons according to their axonal projection patterns. For example, using the adeno-associated virus AAV2-retro, one can label neurons with axons near the site of virus injection, irrespective of whether their cell bodies are nearby or far away. The diagram

(legend continued on next page)

requires creation of a transparent optical "port," such as a cranial window or an implanted microendoscope. In parallel to the development of new microscopes, neuroscientists have created animal preparations that are well matched to the capabilities and requirements of the new instruments. Here we review means to gain long-term optical access to a variety of brain areas.

Implantation of a glass window into the cranium is the most common way to image cells in tissue near the brain surface (Holtmaat et al., 2009), including in many parts of the neocortex, cerebellum, and olfactory bulb (Figure 2A). Such "cranial windows" provide stable optical access for months (or even a year) for longitudinal imaging. Alternative approaches leave the skull intact but render it translucent via mechanical thinning or chemical treatment (Drew et al., 2010). However, in these preparations the skull still induces some light scattering and wavefront distortions that make it harder to resolve cells and sub-cellular processes. The skull also re-grows, making long-term studies more challenging (Yang et al., 2010). An advantage of thinned skull over cranial window preparations is the reduced chance of injuring the brain during the initial surgery (Xu et al., 2007). However, cranial windows can be installed while leaving the dura mater intact, which, when skillfully performed, does not activate detectable glial responses in the underlying brain tissue (Kim et al., 2016). With the addition of a microprism (Andermann et al., 2013), cranial windows can also provide optical access to hard-to-reach areas such as the entorhinal cortex (Low et al., 2014).

Since the characteristic $(1/e)$ attenuation lengths of visible or near-infrared light propagation in brain tissue are ~50–200 μm (Lecoq and Schnitzer, 2011), cranial windows are insufficient for imaging most of the brain's internal volume. The most common way to image cells in deep areas is to implant an optical microendoscope, with one end of the microendoscope lying within or just above the brain area of interest and the opposite end protruding through the cranium (Barretto et al., 2011, 2009; Jung et al., 2004; Jung and Schnitzer, 2003; Levene et al., 2004). Due to the difficulty of fabricating microlenses with curved refractive surfaces, the most commonly used microendoscopes comprise one or more gradient refractive index (GRIN) lenses, which have flat external faces and guide axial light propagation via internal variations of the optical refractive index (Jung et al., 2004; Jung and Schnitzer, 2003). The microendoscope is usually designed to relay a real optical image of the focal plane in tissue to a plane just above its external glass face (Figure 2B).

Either one- and two-photon fluorescence imaging can be performed through GRIN microendoscopes, using a benchtop microscope in head-fixed animals (Barretto et al., 2011, 2009; Jung et al., 2004; Levene et al., 2004) or a head-mounted, miniaturized one-photon microscope for studies in freely moving animals (Flusberg et al., 2008; Ghosh et al., 2011). To access a variety of brain areas, microendoscopes come in a range of lengths and diameters, which has allowed one-photon Ca^{2+} imaging in freely moving animals within the neocortex (Pinto and Dan, 2015), hippocampus (Cai et al., 2016; Ziv et al., 2013), striatum (Klaus et al., 2017; Owen et al., 2018; Parker et al., 2018), nucleus accumbens (Scribner et al., 2020), amygdala (Corder et al., 2019; Grewe et al., 2017; Gründemann et al., 2019; Li et al., 2017b), thalamus (Hornung et al., 2020), substantia nigra (da Silva et al., 2018), parabrachial nucleus (Jarvie et al., 2021), habenula (Lecca et al., 2020), and hypothalamus (Remedios et al., 2017). In many of these studies, researchers tracked the Ca^{2+} activity of individual neurons across multiple sessions spanning weeks (Jercog et al., 2016; Sheintuch et al., 2017). Although the chronic implantation of a microendoscope into brain tissue is invasive, there are scant reports of changes in animal behavior or abnormalities in neural activity after the animal has fully recovered from the implantation surgery. Nonetheless, researchers should confirm that the animal behavior of interest and neural activity under view are not adversely affected by microendoscope installation. Notably, bilateral implants within the same brain structure may increase the risk of behavioral deficits (Grewe et al., 2017).

A key goal of recent work has been to extend the above preparations to allow imaging of multiple brain areas at once. To this end, the "Crystal Skull" preparation for mice provides long-term optical access to cells across most of the dorsal neocortex (Figure 2C), or about 30–40 cortical areas, by replacing most of the dorsal cranium with a curved glass window whose lateral radius of curvature matches that of the adult brain (Kim et al., 2016). With large cranial windows of this kind, a concern has been the change in brain temperature that results from removal of the overlying skull. Brain tissue under even a small (e.g., 4 mm^2) cranial window is a few degrees below physiological temperatures, which can alter neural function (Kalmbach and Waters, 2012; Podgorski and Ranganathan, 2016). Interestingly, the increased cooling under a cranial window can be beneficial for offsetting the heat delivery from optical illumination (Rumyantsev et al., 2020; Zhang et al., 2019). Ideally, researchers should balance the magnitudes of these effects, to promote physiological neural activity patterns and ensure long-term brain health.

To reach two or more distally located or deep brain areas, one can install optical ports at multiple locations (Lecoq et al., 2014; Yang et al., 2019). For instance, installation of 4 optical ports (2 cranial windows and 2 multi-mode fibers; Figure 2D) enabled simultaneous Ca^{2+} imaging in motor cortex and cerebellum and bilateral optogenetic manipulations in the basal pontine nuclei (Wagner et al., 2019). Preparations with 2 ports allowed concurrent Ca^{2+} imaging in the premotor and cerebellar cortices

illustrates an example in which AAV2-retro is injected at a site in one coronal plane (2; in the striatum), allowing the virus to label the cell bodies of neurons in other coronal planes that project axons to the injection site. Right: example images taken at 4 different coronal planes (numbered as at left) revealing expression of the red fluorescent marker, tdTomato, in the cortex, amygdala, and thalamus after AAV2-retro injection in the striatum. Scale bars, 800 μm (1, 2) and 200 μm (3, 4). (F) Left: viral and transgenic methods can be combined to enhance targeting of specific neural populations. For instance, in a Cre driver mouse line that targets layer 5 cortical pyramidal neurons (Rbp4-Cre), injection into the pons of a AAV2-retro virus that allows Cre-dependent expression of tdTomato (red) selectively labels layer 5 neurons in the cortex (Ctx) that project axons to the pons. AAV1-EGFP virus (green) that is co-injected into the pons labels pontine axonal output to the cerebellum (Cbl). Right: fluorescence image illustrating this hybrid approach, showing cortico-pontine axons in red and ponto-cerebellar axons in green. Scale bar, 1 mm.

(A)–(C) are adapted from Daigle et al. (2018). (D) is adapted from Challis et al. (2019). Fluorescence images are courtesy of M. Fabiszak/W. Freiwald lab. (E) and (F) are adapted from Tervo et al. (2016).

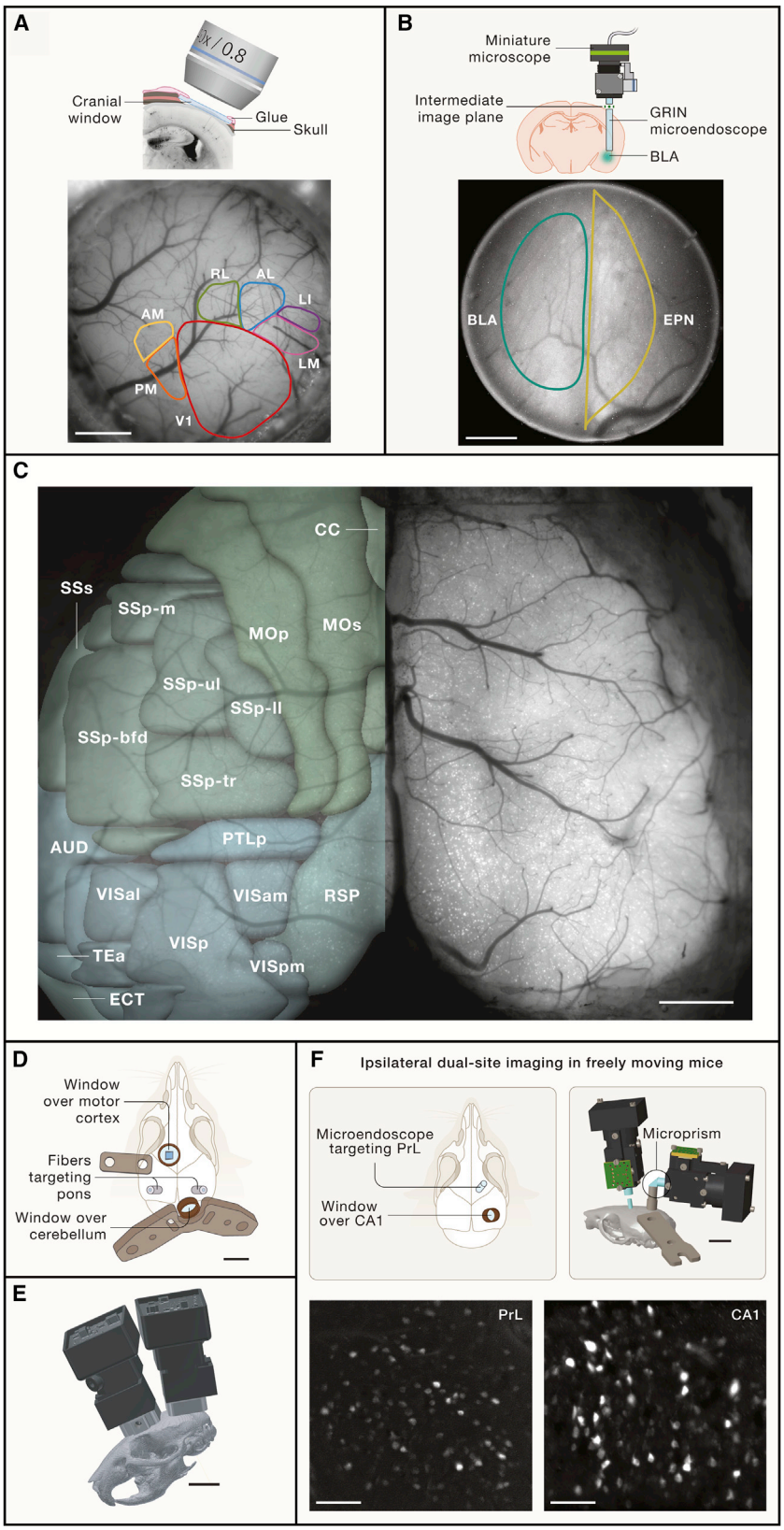

Figure 2. Chronic preparations for imaging neural activity in multiple brain areas

(A) Top: to implant a cranial window, a portion of the skull is removed and permanently replaced by a glass coverslip (typically 3–7 mm in diameter). Bottom: large windows provide access to multiple cortical areas, as illustrated here with a bright-field image of the brain taken through a window atop the primary visual (V1) and higher-order visual cortical areas (AM, PM, RL, AL, LM, LI). Scale bar, 1 mm.

(B) Top: to image deep brain regions, gradient refractive index (GRIN) microendoscopes can be inserted to the area of interest, as illustrated here for the basolateral amygdala (BLA). Teal shading beneath the microendoscope denotes fluorescence labeling. Microendoscopes typically have diameters of 0.5–2.0 mm and lengths of 2–10 mm and project a real image of the specimen plane to just above the microendoscope's external face. Microendoscopes are compatible with a variety of imaging modalities, including the miniature integrated fluorescence microscope depicted in the figure. Bottom: a bright-field image of the BLA and endopiriform nucleus (EPN) taken through an implanted microendoscope. Scale bar, 200 μm.

(C) In the "Crystal Skull" preparation, the entire dorsal portion of the mouse cranium is permanently replaced with a curved glass window with a radius of curvature that matches that of the cortical surface. The fluorescence image shown here is a maximum projection of a 20 s recording of neural Ca^{2+} activity acquired on a one-photon epifluorescence macroscope in a transgenic mouse (Rasgrf2-2A-dCre/CaMKIIa-tTA/Ai93) expressing GCaMP6f in layer 2/3 cortical pyramidal cells. Individual cells are visible as discrete puncta in this low-magnification image. Atop the left cerebral hemisphere is a map of >30 cortical areas as demarcated in the Allen Brain Atlas (https://mouse.brain-map.org/static/brainexplorer). Scale bar, 1 mm.

(D) For simultaneous access to two or more distally separated brain areas, multiple optical ports can be created on the cranium. For example, to enable simultaneous two-photon Ca^{2+} imaging of neural activity in premotor cortex and the contralateral cerebellum, Wagner et al. (2019) installed a pair of 3-mm-diameter windows, one above each of these two brain areas. To allow concurrent optogenetic manipulations of the disynaptic cortico-cerebellar pathway, a pair of multimode fiber implants was also implanted bilaterally targeting the pontine nuclei. Figure 1F shows the cortico-ponto-cerebellar circuit. Scale bar, 3 mm.

(E) A pair of windows, installed similarly to (D), allowed concurrent one-photon fluorescence Ca^{2+} imaging of motor cortical and cerebellar neural activity in freely moving mice using a pair of miniaturized microscopes. Scale bar, 5 mm.

(F) Dual-site Ca^{2+} imaging in two brain areas in the same cerebral hemisphere of a freely moving mouse. Top: one GRIN microendoscope targets the prelimbic cortex (PrL), and another microendoscope targets the CA1 sub-field of the ipsilateral hippocampus. To allow the joint use of two mini-microscopes, the hippocampal microendoscope has a right-angle microprism atop its external face, allowing the two microscopes to be oriented orthogonally to avoid collision. Scale bar, 5 mm. Bottom: a pair of maximum-intensity projection images of Ca^{2+} movies taken simultaneously in the two brain areas in a transgenic mouse expressing GCaMP6f (Rasgrf2-2A-dCre/CaMKIIa-tTA/Ai93). Scale bars, 100 μm.

(A) is adapted from Holtmaat et al. (2009) and Stirman et al. (2016). (B) is adapted from Grewe et al. (2017). (C) is from Kim et al. (2016). (D) is from Wagner et al. (2019). (E) is from de Groot et al. (2020). (F) was provided by Tony H. Kim and Yanping Zhang.

(de Groot et al., 2020) or in both hippocampi (Gonzalez et al., 2019) in freely moving mice bearing a pair of mini-microscopes, one mounted atop each cerebral hemisphere (Figure 2E). Joint imaging of the neocortex and hippocampus in the same hemisphere is also feasible with two mini-microscopes that are mounted perpendicularly to one another (Figure 2F).

As animal preparations grow more sophisticated, implanted microendoscopes or glass windows may incorporate ancillary elements that facilitate neuroscience experiments. The inclusion of transparent electrodes within the aperture of a cranial window allows concurrent optical and electrophysiological recordings (Thunemann et al., 2018). To improve the ease and success rate of Ca^{2+} imaging, coating a microendoscope with an AAV to express the Ca^{2+} indicator can ensure that expression is centered at the imaging site and reduce background fluorescence from unwanted expression beyond the specimen plane (Jackman et al., 2018). Future additions to extant animal preparations might facilitate temperature control or automated drug delivery (McCall et al., 2017).

CHOOSING AN IMAGING MODALITY FOR MONITORING LARGE-SCALE NEURAL ACTIVITY

Prior reviews have discussed the factors that determine whether a given brain-imaging study might be best performed with freely moving animals and miniaturized microscopes, or with head-fixed animals and a benchtop microscope, using either one- or two-photon fluorescence imaging (Hamel et al., 2015; Yang and Yuste, 2017). Here, we provide an overview of the key considerations.

A first issue is whether the animal behavior of interest is best studied in unrestrained or in head-restrained subjects. While the field has made substantial progress in adapting many behavioral assays to a head-fixed format, many forms of naturalistic behavior are better exemplified in freely behaving animals and hard to study well in head-fixed subjects. In cases in which a behavior can be studied in either format, there can also be practical reasons to use freely moving animals. For instance, studies of spatial navigation can be done with head-fixed rodents navigating in a virtual reality (Dombeck et al., 2010; Harvey et al., 2009), but training animals to navigate in virtual mazes generally takes much longer than in real environments. Many researchers may also prefer to use established behavioral apparatus and assays for unrestrained animals that have been widely validated by numerous labs and pharmaceutical companies and for which there are pre-existing datasets and publications. The capacity to add optical imaging of neural activity to these existing assays is often highly attractive.

On the other hand, some behaviors are best studied in experiments in which the animal is presented with a large number of sensory stimuli under uniform conditions or performs a large number of highly stereotyped actions, which head-fixation often facilitates. Examples of such instances include studies of visual processing and of targeted reaching movements, respectively. Moreover, the use of head-fixation frees one to use complex optical instrumentation without having to miniaturize it. For example, while head-mounted and tabletop microscopes have incorporated one-photon optogenetic capabilities (Stamatakis et al., 2018; Wagner et al., 2019), to date only tabletop instruments have integrated imaging with two-photon optogenetics, for optical manipulations of user-selected cells targeted on the basis of their imaged activity patterns (see the section below on this topic). Similarly, high-speed voltage imaging studies at single-spike resolution have only been achieved to date in head-fixed animals.

Given a decision to image in freely moving animals, in most cases this leads to the use of a one-photon, miniature fluorescence microscope that integrates a light-emitting diode (LED), image sensor chip and miniaturized optics within a head-mounted device that is ~2 g in mass. Since their introduction (Ghosh et al., 2011), such integrated miniature microscopes have been used extensively for Ca^{2+} imaging studies in freely moving mice and rats (~200 publications) and are also applicable to birds and monkeys (Bollimunta et al., 2021; Kondo et al., 2018; Roberts et al., 2017). These systems now enable Ca^{2+} imaging at frame rates up to ~60 Hz and can track hundreds of neurons at a time across FOVs up to ~0.5 mm^2 (Ziv et al., 2013). When combined with an appropriate microendoscope, integrated miniature microscopes can access a wide variety of brain areas, as cited above. Recent versions of the integrated miniature microscope incorporate fast electronic focusing, which facilitates time-lapse imaging and allows multi-plane image acquisition, and a second LED for dual-color imaging or optogenetic manipulations within the imaging FOV (Stamatakis et al., 2018).

A few studies have used fiber-optic two-photon microscopes that have been miniaturized (5–25 g mass) for use in freely moving rats (Helmchen et al., 2001), enabling Ca^{2+} imaging of ~16 cortical layer 2/3 neurons at 11 Hz frame rates (Sawinski et al., 2009). A miniature, fiber-optic three-photon microscope for use in rats tracked the Ca^{2+} activity of a similar number of cells in cortical layer 5 at 28 Hz (Klioutchnikov et al., 2020). Mice require even smaller head-mounted devices (~4 g or less). Building off the design of miniature (2–3 g) microscopes that used a silicon micromachined scanning mirror for two-photon imaging (Piyawattanametha et al., 2006, 2009; Zong et al., 2017), a recent study performed 5 Hz multi-plane Ca^{2+} imaging in >350 cortical neurons in freely moving mice using a 4.2 g two-photon microscope (Zong et al., 2021). The use of this system to image subcortical brain areas via microendoscopes has not yet been demonstrated, and it remains unclear whether future versions will attain FOVs and frame rates comparable to one-photon miniaturized systems. However, perhaps the biggest drawbacks of miniaturized multiphoton systems concern the technical complexity of delivering ultrashort optical pulses in fiber optics and a reliance on tabletop lasers and optical instrumentation that may not fit into typical animal behavior rooms.

For experiments in head-restrained animals, the facets of brain activity that one aims to monitor will generally dictate the most suitable imaging modality. To image the transmembrane voltage dynamics of individual neurons, a one-photon epifluorescence microscope equipped with a high-speed camera can presently sample more neurons than high-speed two-photon microscopy (see section on voltage imaging). Similarly, for cellular-level Ca^{2+} imaging across multiple cortical regions, a one-photon epifluorescence macroscope can image larger FOVs at faster

frame-acquisition rates than two-photon microscopes but usually cannot penetrate beyond cortical layer 2/3 in the mouse (see next 4 sections). Two-photon microscopy also has significant strengths. In addition to offering greater penetration depth, two-photon microscopes are generally superior for volumetric imaging, resolving fine neuronal processes, and integration with two-photon optogenetics. Three-photon microscopy achieves even greater penetration into tissue. In the sections that follow, we explore these optical considerations in greater detail.

ADVANCES IN TWO-PHOTON MICROSCOPY FOR MONITORING LARGE-SCALE CA^{2+} ACTIVITY

As prior reviews cover the principles of laser-scanning two-photon microscopy (Helmchen and Denk, 2005; Zipfel et al., 2003), we assume readers are familiar with laser-scanning two-photon microscopy as a means of imaging up to ~800 μm deep in opaque tissue. Unlike confocal fluorescence microscopy, which uses a pinhole in the detection pathway to block emissions generated outside the focal plane, two-photon microscopy achieves optical sectioning via nonlinear excitation of fluorescence through the coincident absorption of two illumination photons. This nonlinear process confines fluorescence generation to the vicinity of the laser focal spot and is typically induced using infrared ultrashort-pulsed lasers that provide extremely brief (~100 fs), intense pulses of light. Due to the infrared illumination, which scatters less than visible light, and wide-field detection of both ballistic (i.e., un-scattered) and scattered fluorescence photons, two-photon microscopes can acquire high-resolution images from deep within scattering media such as the mammalian brain.

After the initial demonstration of two-photon imaging (Denk et al., 1990), subsequent work aimed to improve the capabilities of this imaging modality. For example, later research sought to expand the FOV (Tsai et al., 2015), enable rapid steering of the illumination beam in three dimensions (Botcherby et al., 2012; Grewe et al., 2011; Kong et al., 2015), and increase data acquisition rates by multiplexing different illumination beams in time and/or space (Cheng et al., 2011; Kim et al., 2007). Building on these efforts, work of the past few years has enabled large-scale two-photon Ca^{2+} imaging studies encompassing multiple brain areas.

Motivated by the emergence of large cranial window preparations (Figure 2), several groups created two-photon mesoscopes that use a large objective lens to image neural Ca^{2+} activity across ~4–35 mm^2 tissue areas (Ota et al., 2021; Rumyantsev et al., 2020; Sofroniew et al., 2016; Stirman et al., 2016). Designing a microscope of this kind presents notable challenges, due to the needs to correct for optical aberrations in the illumination pathway over a much wider FOV than in conventional systems, design and fabricate large-aperture filters and light collection optics that are commensurate with the use of a large objective lens, and develop a laser-scanning mechanism and sampling protocol to interrogate a broad FOV while maintaining frame rates that are fast enough to capture neural Ca^{2+} dynamics. Addressing this last challenge presents important design choices that trade-off between the FOV size, the image pixel size, the image frame-acquisition rate, and the "cellular duty ratio"—i.e., the fraction of time per image frame devoted to collecting fluorescence from an individual cell.

Given a maximum speed with which the laser focus can be swept across the specimen plane, sampling a wider FOV at a fixed resolution (e.g., 1 μm per pixel) will plainly increase the time needed to acquire an image frame. Alternatively, a wider FOV can be sampled without lowering the frame rate by sacrificing spatial resolution. In both cases, increasing the FOV decreases the cellular duty ratio, which, given a fixed illumination power, reduces the number of fluorescence photons excited per cell per second, a key determinant of the microscope's sensitivity to Ca^{2+} events (see next section). Presently, most two-photon mesoscopes require users to choose among different laser-scanning modes that constitute different compromises between these parameters.

Thus, while the engineering to attain sub-cellular spatial resolution across a 5-mm-wide FOV using a large, custom-designed objective lens was a notable achievement for two-photon microscopy (Sofroniew et al., 2016), there is still no laser-scanning mechanism that can acquire images across this system's full FOV at both fine spatial resolution (e.g., ~1 μm per pixel) and fast imaging rates (~30 Hz). Instead, one can sample the full FOV with micron-sized pixels at <1 Hz frame rates (pattern 1, Figure 3A), with ~12-μm-wide pixel spacing at ~4 Hz (pattern 2), or with intermediate values between these. The system can also sample a conventional 0.6-mm-wide FOV using 0.6-μm-wide pixels at a 21 Hz frame rate (pattern 3). To perform multi-area imaging, the user typically selects two or more regions of interest within the available FOV (Figure 3B). The laser scans each region and successively hops among them such that the net imaging rate declines with the number of regions (pattern 4, Figure 3A).

An alternative strategy for sampling multiple brain areas with a single large objective lens involves spatiotemporal multiplexing. Instead of using one laser beam to serially sample two or more sub-regions of a wide FOV, these schemes employ two or more laser illumination pathways, each with its own laser scanner, that are configured such that the laser pulses from each pathway arrive at the sample in a temporally interleaved manner (Stirman et al., 2016; Voigt et al., 2015). Using high-speed photodetection electronics, the fluorescence signals excited by the interleaved illumination pulses are demultiplexed and assigned to the appropriate sub-region. This approach enabled Ca^{2+} imaging at up to ~30 Hz in a pair of ~250-μm-wide regions in the S1 and S2 somatosensory cortical areas in behaving mice (Condylis et al., 2020).

A basic limit to spatiotemporal multiplexing is set by the fluorescence lifetime of the activity indicator. After excitation by an ultrafast laser pulse, GCaMP fluorescence decays with a $1/e$ time of ~2.7 ns (Akerboom et al., 2012). Thus, given a conventional Ti:sapphire laser that emits pulses at 80 MHz, or once every 12.5 ns, only ~2–3 pulse trains can be interleaved without crosstalk between fluorescence signals excited by the different pulse trains. One way to increase the number of pulse trains that can be interleaved is to decrease the repetition rate of the laser. For example, building on past studies that used temporally interleaved pulse trains to image multiple axial planes in tissue

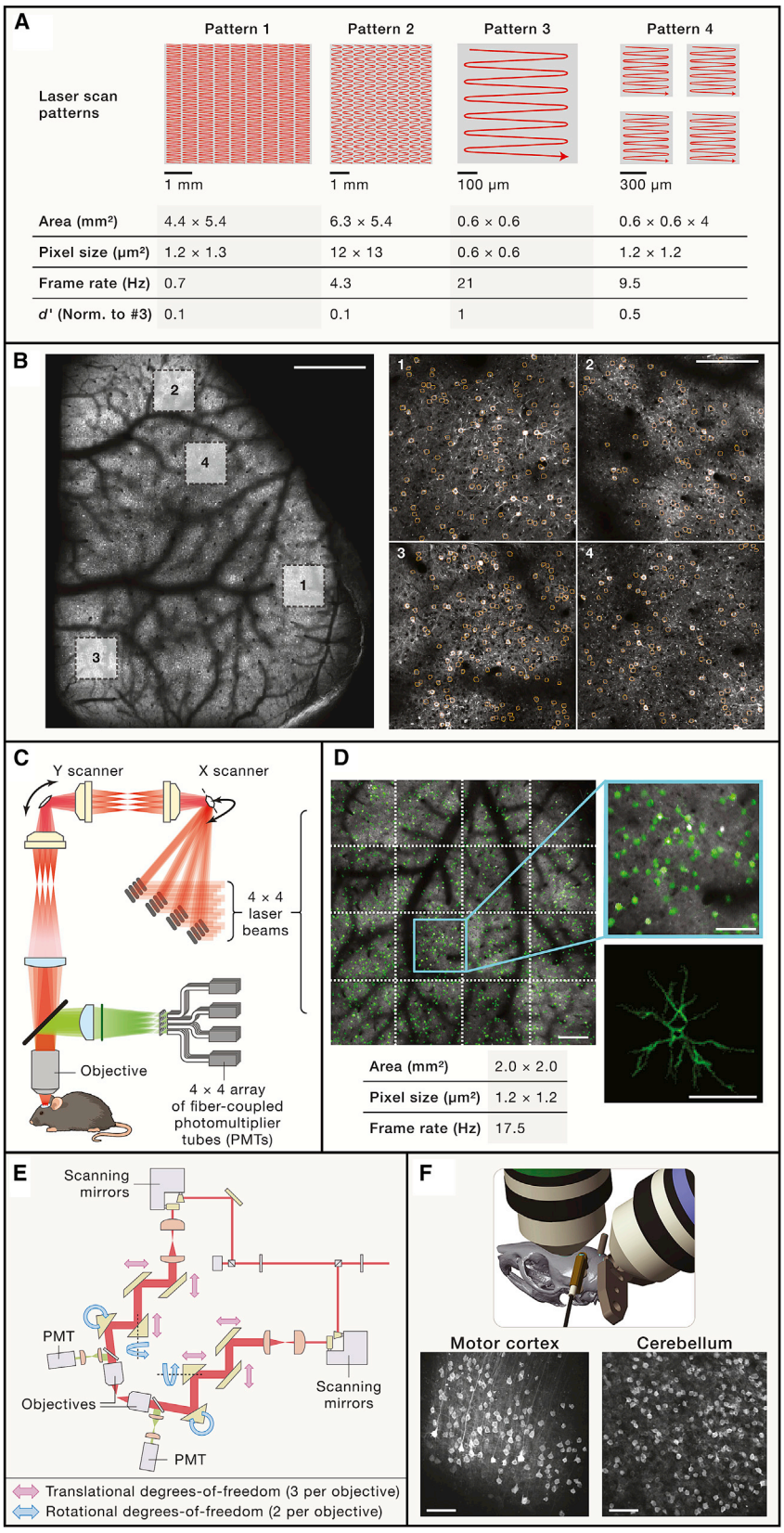

Figure 3. Two-photon mesoscopes and multi-arm microscopes for monitoring neural Ca^{2+} activity in multiple brain areas

(A) A two-photon mesoscope made by Sofroniew et al. (2016) has a ~5-mm-wide FOV. However, imaging with this system requires trade-offs between spatial and temporal sampling. Different patterns of laser scanning are feasible, yielding different combinations of FOV area, image pixel size, and frame-acquisition rate. Shown are 4 different laser-scanning patterns, in which each red trace denotes the laser beam trajectory. In patterns 1 and 2, the mesoscope acquires images across the entire accessible FOV, but at sub-1-Hz frame-acquisition rates or with coarse pixel spacing, as shown in the table entries below each pattern. Pattern 3 samples a conventional 600-µm-wide FOV with finer spatial resolution at a 21 Hz frame rate. Pattern 4 sequentially samples four sub-regions at a 9.5-Hz frame rate. In the table, d' values are normalized to those of pattern 3 with all other optical conditions held fixed.

(B) Example images from the neocortex of a Thy1-GCaMP6f transgenic mouse, taken with the mesoscope of (A). Left: an image of the brain acquired by sweeping the laser across much of the accessible FOV using scanning pattern 2 shown in (A). Highlighted are 4 sub-regions in which Ca^{2+} imaging was performed at higher spatiotemporal resolution. Scale bar, 1 mm. Right: images from each of the 4 regions highlighted at left, taken with scanning pattern 4 shown in (A). Orange circles indicate regions of interest corresponding to individual neurons. Scale bar is 200 µm and applies to all 4 images.

(C) A different two-photon mesoscope (Rumyantsev et al., 2020) uses a 4 × 4 array of laser illumination beams and a corresponding array of photodetectors (PMT, photomultiplier tube) to sample 16 different sub-portions of the specimen plane in parallel. Each beam sweeps across a 500-µm-wide area, enabling Ca^{2+} imaging over a 2 × 2 mm area with micron-scale pixel resolution at frame rates up to 20 Hz.

(D) Fluorescence image of the primary visual cortex (V1) of a triple transgenic mouse (Rasgrf2-2A-dCre/CaMKIIa-tTA/Ai93) expressing GCaMP6f in layer 2/3 cortical pyramidal cells, taken using the mesoscope of (C). Identified neurons are shown in green. Dotted white lines demarcate the 16 image tiles. Acquisition parameters are listed below the image. Scale bar, 250 µm. Top inset: a magnified view of the image portion outlined in blue. Scale bar, 100 µm. Bottom inset: spatial profile of one GCaMP6f-expressing neuron, demonstrating sub-cellular spatial resolution. Scale bar, 100 µm.

(E) Schematic of a dual-axis two-photon microscope for imaging a pair of distally separated brain areas. Each microscope arm has 3 translational and 2 rotational mechanical degrees of freedom (DOFs), enabling flexible positioning of 2 microscope objectives. Illumination beams are simultaneously scanned in the two FOVs using two independent sets of scanning mirrors. This system can image pairs of brain areas that are separated by as little as ~1 mm (Lecoq et al., 2014) or >9.5 mm apart (as in F).

(F) Concurrently acquired pair of images of motor cortical layer 5 neurons and cerebellar granule cells, obtained using the dual-axis microscope of (E) and the multi-port surgical preparation of Figure 2D. GCaMP6f was expressed in the 2 brain regions using a quadruple transgenic mouse (Rbp4-Cre/Math1-Cre/Ai93/ztTA). Scale bars, 100 µm (motor cortex) and 50 µm (cerebellum).

(A) and (B) are adapted from Sofroniew et al. (2016). (C) and (D) are adapted from Rumyantsev et al. (2020). (E) is adapted from Lecoq et al. (2014). (F) is adapted from Wagner et al. (2019).

rather than distinct lateral sub-areas (Amir et al., 2007; Beaulieu et al., 2020; Cheng et al., 2011), a recently described mesoscope used a laser with 5 MHz repetition rate to generate 30 interleaved pulse trains that were each focused to different depths and swept together across the tissue (Demas et al., 2021).

Another strategy to scan large tissue areas uses paired arrays of beams and photodetectors to sample multiple adjoining tissue regions in parallel. Exemplifying this approach, a recent mesoscope used 4 × 4 arrays of beams and detectors for two-photon Ca^{2+} imaging at 17.5 Hz with 1.2-μm-wide pixels across a 4 mm^2 FOV (Figures 3C and 3D) (Rumyantsev et al., 2020), which a single-beam approach cannot match (Sofroniew et al., 2016). At any instant in time, only 4 of the 16 beams were active; this boosts two-photon excitation 4-fold relative to a scenario in which all 16 beams were always active. Further, with all 16 photodetectors continuously on, the modest amount of fluorescence scattering between active and inactive image tiles can be computationally unmixed. Given the advent of high-quality microfabricated photodetector arrays and high-power ultrafast lasers, this spatiotemporal multiplexing strategy is scalable to even larger FOVs. As it is also compatible with the use of temporally interleaved pulse trains, we expect that future two-photon mesoscopes may incorporate both approaches.

Whereas large cranial windows are naturally paired with two-photon mesoscopes, animal preparations with multiple optical ports over non-contiguous brain areas are better served by imaging systems that follow a different design philosophy: one that emphasizes mechanical flexibility when positioning multiple objective lenses or microendoscopes about a single subject (Figure 3E) (Lecoq et al., 2014). Such "multi-axis" microscopes are complementary to large-area two-photon mesoscopes, as many brain areas that interact closely together cannot be contained within the FOV of one objective lens. To understand global brain dynamics, it is vital to have systems that can image activity in two or more brain areas concurrently, regardless of their anatomic locations. For instance, a dual-axis two-photon microscope enabled joint recordings in premotor cortex and cerebellum via concurrent ≥30 Hz Ca^{2+} imaging across 600- and 250-μm-wide FOVs, respectively (Figure 3F) (Wagner et al., 2019). Another dual-axis system combined two-photon microscopy along one optical axis with wide-field epi-fluorescence imaging along the other axis, to relate single-cell dynamics in one brain area to mesoscale cortical activity across the brain (Barson et al., 2020). We expect that future multi-axis microscopes will incorporate even more optical pathways to image larger sets of anatomically distributed but interconnected brain areas.

EVALUATING A TWO-PHOTON MICROSCOPE'S SENSITIVITY TO NEURAL ACTIVITY

When assessing a two-photon microscope's utility for imaging neural activity, users commonly consider the FOV size and frame rate. However, due to its influence on spike detection sensitivity, the cellular duty ratio is equally important. This point came to the fore as several groups (Brondi et al., 2020; Huang et al., 2020) noted that FOVs and frame rates used for GECI evaluation (Chen et al., 2013) often differ from those of large-scale Ca^{2+} imaging studies, which usually have larger FOVs and slower frame rates that lead to underreporting of single spikes (Figure 4A).

To examine how laser-scanning parameters affect spike sensitivity in Ca^{2+} imaging, Huang et al. (2020) made concurrent optical and electrical recordings from the same cells in two different imaging configurations while maintaining the same illumination power (Figures 4A and 4B). In mice expressing GCaMP6f in cortical neurons, the rate at which isolated, single action potentials were detected by two-photon Ca^{2+} imaging fell from 54% ± 27% when imaging a 20-μm-wide area at 158 Hz, to 15% ± 10% when imaging a 400-μm-wide area at 30 Hz (Figure 4C), given a constant 5% false-positive detection rate. In both configurations, Ca^{2+} transient detection rates were higher when multiple spikes arose in rapid succession, showing that Ca^{2+} transients more faithfully convey spike bursts. Below we use signal detection theory to explain these findings (Brondi et al., 2020; Huang et al., 2020) and discuss the implications for large-scale Ca^{2+} imaging studies.

For a raster-scanning microscope operating at a fixed illumination power, Figure 4D plots how d' varies with the imaging frame rate and FOV width, based on the data of Huang et al. (2020). When the frame rate is sufficiently high (≳10 Hz for GCaMP6f), the sensitivity to single spikes depends on the FOV size but not the frame rate. In this regime, $d' \approx (\Delta F/F) \cdot \sqrt{(F_0 \tau/2)} \propto \frac{1}{\sqrt{A_{FOV}}}$, where A_{FOV} is the FOV area, showing how the sensitivity declines for larger FOVs. This scaling fits with measured single-spike detection rates for FOVs of different sizes (Huang et al., 2020).

These considerations are critical when evaluating laser-scanning patterns for large-scale two-photon Ca^{2+} imaging. Given a fixed illumination power, the different scanning patterns in Figure 3A lead to distinct d' values. Scan patterns 1 and 2, which cover the full ~5 mm FOV, yield d' values that are one-tenth that of pattern 3, which covers a 0.6-mm-wide FOV. As one samples multiple regions of this size (pattern 4), d' falls with the square root of the number of regions. Thus, a key challenge for two-photon Ca^{2+} imaging is how to scale the technology to larger FOVs without reducing frame rates or spike detection sensitivity, while also avoiding brain heating and tissue damage due to increases in illumination power (Podgorski and Ranganathan, 2016).

A power-efficient strategy to increase the numbers of neurons that can be reliably monitored is to deliver illumination selectively to cells of interest, rather than uniformly across the FOV. Initial implementations of this concept in two-photon microscopy involved random-access scanning, typically using fast acousto-optic deflectors to scan a sequence of point targets in the sample while minimizing the laser's transition times between the targets (Grewe et al., 2010; Duemani Reddy et al., 2008). Since random-access scanning illuminates only pixels of interest, it can attain much higher cellular duty ratios than raster scanning. However, initial random-access scanning microscopes acquired fluorescence from sets of discrete point targets, making the data susceptible to brain motion. More recent versions of random-access scanning enable 3D imaging and allow the user to scan a sequence of small image patches or volumes that each contain an individual cell (Figure 4E), thereby enabling correction of brain motion artifacts with standard image

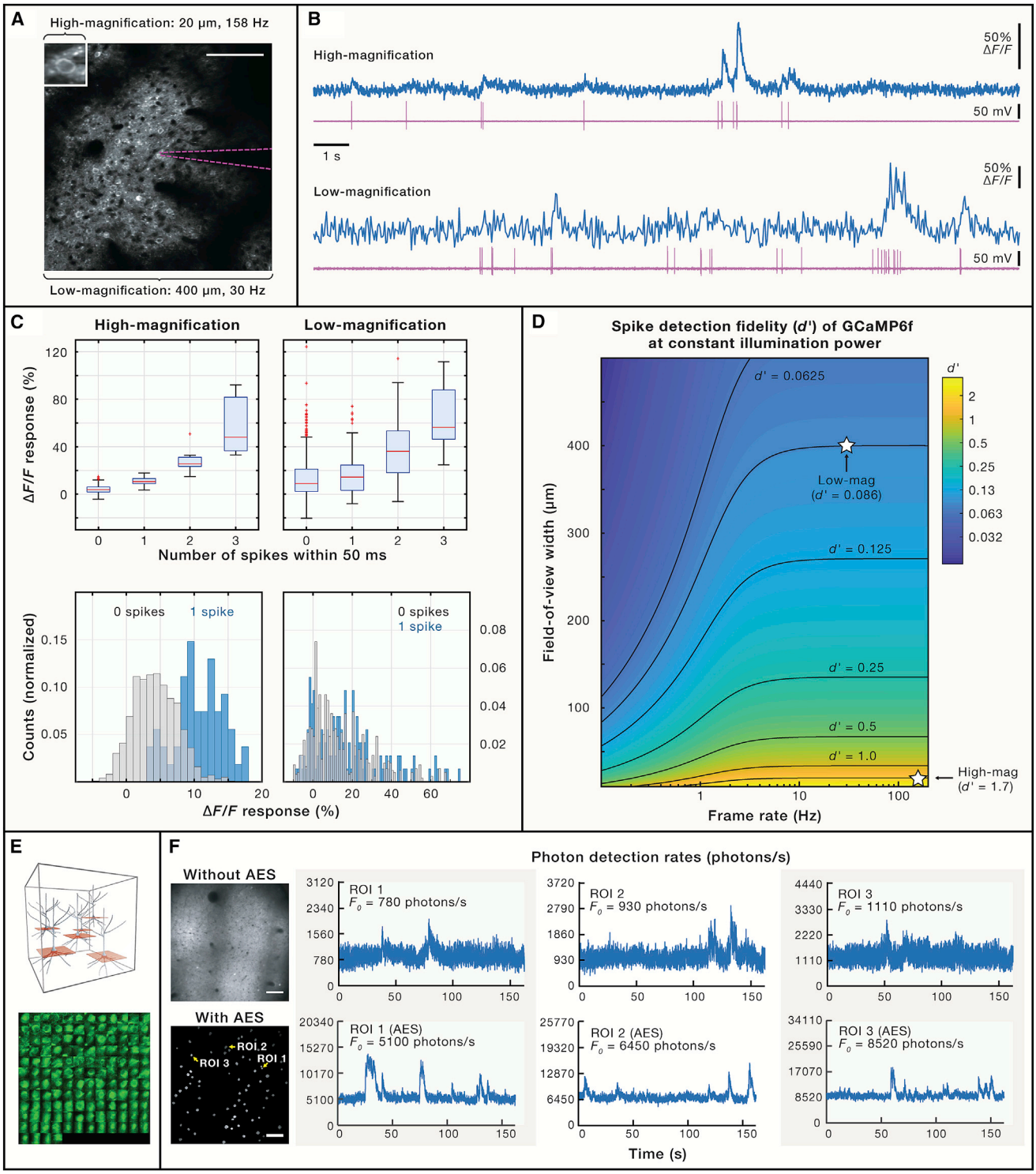

Figure 4. Photon detection rate per cell is a key determinant of single-spike sensitivity

In two-photon microscopy, the rate at which fluorescence is captured from individual cells varies with the illumination power and the time per image frame that the laser dwells on each cell (cellular duty ratio). In a raster-scanning microscope, when a user increases the total area in tissue that is scanned with the laser at a fixed laser power, the sampling time per neuron and thus the spike sensitivity both decline.

(A) To study how the ability to detect single action potentials varies with the scanning parameters of two-photon Ca^{2+} imaging, Huang et al. (2020) performed simultaneous loose-patch electrical and optical Ca^{2+} recordings of neural activity in transgenic mice (Cux2-CreER^{T2}/CaMKIIa-tTA/Ai93) expressing the Ca^{2+} indicator GCaMP6f in layer 2/3 visual cortical pyramidal cells. (A)–(C) compare results from two different imaging configurations, a low-magnification

(legend continued on next page)

registration algorithms (Nadella et al., 2016; Szalay et al., 2016) or even real-time optical corrections for the brain's 3D movements (Griffiths et al., 2020). Despite their potential for boosting the cellular duty ratio and increasing d' values, acousto-optic scanners have not become commonplace in two-photon microscopy, perhaps due to the sophisticated electronic systems that are needed to control fast, 3D acousto-optic laser scanning (Griffiths et al., 2020; Nadella et al., 2016; Szalay et al., 2016).

An alternative means of selectively sampling neurons in the FOV involves an adaptive excitation source (AES), a laser whose output power can be rapidly modulated based on the image content (Li et al., 2020). For example, when imaging a 700-μm-wide FOV at 30 Hz, an AES was gated to emit light pulses only when they would illuminate the sample in the vicinity of neuronal somata (Figure 4F); with this approach, fluorescence detection rates per cell (F_0) were ~7-times higher than with conventional laser scanning, even with 4.5-times less mean illumination power. Although AES lasers are not yet commercially available, in principle they could be retrofitted onto many existing two-photon microscopes with relatively minor changes to the instrumentation control software.

Another way to boost F_0 takes advantage of the nonlinear nature of multiphoton absorption. Conventional two-photon microscopes typically use $N \approx 10$ or more pulses per pixel for neural Ca^{2+} imaging. Given a fixed illumination energy for each pixel, concentrating all of it in a single pulse raises F_0 by N-fold, due to the quadratic dependence of two-photon excitation on pulse energy (Theer et al., 2003; Weisenburger et al., 2019). New techniques such as fast, "all-optical" laser scanning within single planes (Wu et al., 2020) and multiplexing schemes in which sequential pulses sample distinct axial planes in tissue (Beaulieu et al., 2020; Demas et al., 2021) have led to microscopes that operate at or near the one-pulse-per-pixel limit. Illuminating each pixel with more energetic pulses that arrive less frequently might also reduce photobleaching (Donnert et al., 2007) but could increase nonlinear photodamage (Hopt and Neher, 2001). These effects should be explored in more detail for one-pulse-per-pixel imaging, but overall, this mode of imaging is promising and will likely become more widespread.

More broadly, as spike detection rates improve faster than exponentially with increases in d' (Wilt et al., 2013), there is strong theoretical motivation for continued, incremental progress in both optical instruments and indicators. By combining next-generation activity indicators with instruments that are expressly engineered to boost d', single-spike sensitivity may ultimately become routine in large-scale Ca^{2+} imaging studies.

IMAGING NEURAL ACTIVITY USING PARALLEL READOUT STRATEGIES

To monitor neural activity across broader tissue areas, researchers have sought to increase the FOV of one-photon epifluorescence microscopes used for Ca^{2+} or voltage imaging studies. Achieving this while retaining cellular resolution hinges on the availability of scientific-grade cameras with large pixel counts, high quantum efficiency of photon capture, low read noise, and frame-acquisition rates fast enough to capture the neural events of interest. Today, scientific-grade cameras usually have pixel counts of ~10 megapixels or less; if each pixel covers a ~5-μm-wide area in the specimen plane (about the maximum feasible pixel width while retaining the possibility of cellular resolution, according to the Nyquist criterion and given ~10-μm-wide cell bodies), this roughly corresponds to ~1.6 cm of coverage across the brain.

configuration in which a 400-μm-wide area of tissue was scanned at 30 Hz, representative of conventional two-photon Ca^{2+} imaging of neural population activity (A) and a high-magnification configuration in which a 20-μm-wide area containing only a single cell was scanned at 158 Hz (A, inset). Dashed purple lines outline the glass microelectrode. Scale bar, 100 μm.

(B) Simultaneously acquired traces of Ca^{2+} (blue) and electrical (purple) activity from an individual neuron under the two different imaging configurations shown in (A), at the same illumination power. Action potentials are visible in the electrical traces as discrete impulses.

(C) Assessment of spike sensitivity in the 2 imaging configurations of (A) and (B). Top: box-and-whisker plots showing the fractional change in [Ca^{2+}]-related fluorescence, $\Delta F/F$, as a function of the number of spikes that an example cell fired in a 50 ms interval. For a given number of spikes, median values of the $\Delta F/F$ response (horizontal red lines) are comparable in the 2 configurations, but variances are greater in the low-magnification case due to fewer detected photons per cell. Boxes span 25th to 75th percentiles; whiskers extend to 1.5 times the interquartile distance; red data points are outliers. Bottom: normalized histograms showing the number of instances in which a given $\Delta F/F$ response value was observed in a 50 ms interval with no spikes (gray data) or a single spike (blue data). The spike detection fidelity (d') depends on the separation between the pair of histograms. The distributions are modestly different in the high-magnification configuration (bottom left) but are nearly indistinguishable in the low-magnification configuration (bottom right).

(D) Signal detection theory provides predictions of the spike detection fidelity d' under different imaging conditions. The graph shows a contour plot of d' for GCaMP6f as a function of the two-photon imaging FOV and frame-acquisition rate, with the illumination power held constant. Black lines are equicontours of d'. Points marked with ☆ symbols correspond to the two different imaging configurations of (A)–(C). To produce this plot, we set the single-spike $\Delta F/F$ response and the fluorescence decay time-constant of GCaMP6f to be 19% and 200 ms, per Chen et al. (2013). We then scaled the d' values to fit the true positive rate (TPR) of single-spike detection (~54%) found by Huang et al. (2020) in the high-magnification imaging configuration, given a 5% false-positive rate (FPR). Signal detection theory then predicts a greatly diminished, ~6% TPR for single-spike detection in the low-magnification configuration, consistent with the experimental results in (C).

(E) In conventional two-photon microscopy in which the laser is scanned in a raster pattern, the laser samples many points in the image without labeled neurons, lowering the cellular duty ratio. To improve the duty ratio, random-access scanning selectively addresses a set of user-selected cells. Top: a schematic depiction of a form of random-access scanning ("chessboard" scanning), in which a pair of acousto-optic deflectors scans small, discontiguous patches of tissue (red planes) that each contain an individual cell body. Bottom: single-frame chessboard image of GCaMP6f-expressing pyramidal cells from mouse visual cortex. The 136 neurons shown were imaged at 11.14 Hz. Each image patch is 20 μm wide.

(F) An alternative means of increasing the fluorescence flux per cell in multiphoton Ca^{2+} imaging involves an adaptive excitation source (AES), a laser that allows variation of the illumination power based on the image content. By gating laser emission such that only regions-of-interest (ROIs) with cell bodies are illuminated (bottom left), one can increase the efficiency with which the illumination power generates productive fluorescence, as compared to conventional two-photon imaging of the same specimen (top left). For the 3 ROIs in the bottom left, the right 6 graphs show GCaMP6s fluorescence traces with (bottom row) and without (top row) the use of the AES. When using the AES, the fluorescence per frame per cell, F_0, increased about 7-fold on average, even though the net illumination power delivered to the brain was ~4.5 times lower (18 mW with AES). Frame rate was 30 Hz in both cases. Scale bars, 100 μm.

(A)–(C) are adapted from Huang et al. (2020), using datasets #103920 and #103922 from the Allen Institute for Brain Science (https://portal.brain-map.org/explore/circuits/oephys). (E) is adapted from Szalay et al. (2016). (F) is adapted from Li et al. (2020).

To image a wide area of tissue at high resolution, Fan et al. (2019) built a 5 × 7 array of cameras (193.5 megapixel total) that tiled a 1 cm × 1.2 cm FOV at micron-scale resolution (0.8 μm per pixel in the sample plane), for 30 Hz imaging over most of the mouse dorsal cortex (Figure 5A). This system yields data at >10 GBytes per second, necessitating a cluster of computers to handle data transmission, storage, and real-time stitching of the images on a >1 PByte distributed file system. This tour de force seems out of reach, for now, for most neuroscience labs but shows the feasibility of video-rate imaging with micron-scale pixel resolution over a 1-cm-wide FOV and may be a harbinger of more accessible systems in the future. On the other hand, as larger camera chips arise, it may become unnecessary to use arrays of cameras to cover wide FOVs.

In addition to expanding the lateral spatial coverage, large-pixel-count cameras also enable computational imaging approaches, such as fluorescence light-field microscopy (LFM), which aim to capture volumetric information about the sample from single camera frames. Owing to a micro-lens array placed at an intermediate optical plane of the microscope, individual pixels in the raw data from LFM not only capture fluorescence photons from defined locations in the sample but also record their directions of propagation (Levoy et al., 2006). In transparent samples, these joint data permit computational reconstruction of the sample volume (Broxton et al., 2013; Cong et al., 2017; Prevedel et al., 2014), albeit with a trade-off between the lateral resolution and the number of axial planes in the reconstruction. Recent work has developed miniaturized LFMs for volumetric imaging in freely moving rodents (Skocek et al., 2018; Yanny et al., 2020). However, further studies are needed to validate volumetric neural Ca^{2+} imaging by LFM in mammalian brain tissue (Skocek et al., 2018) and evaluate its performance against other volumetric imaging approaches such as high-speed forms of *in vivo* light-sheet imaging (Voleti et al., 2019) and rapid adjustment of the focal plane using electrically tunable lenses (Grewe et al., 2011).

In both conventional and light-field imaging, one-photon readout of single cell Ca^{2+} or voltage activity appears limited to cells that are <300 μm from the brain surface or the face of an implanted endoscope or microprism, due to light scattering in tissue. The exact attainable depth is influenced by the density of labeled cell bodies, extent of background fluorescence from neuropil or out-of-focus tissues, and dynamic range of activity-related neural signals. For example, with GCaMP6f and cortical-layer-specific labeling, one can monitor neural activity in layer 2/3 cortical pyramidal cells through a cranial window by one-photon fluorescence imaging (Kim et al., 2016). Labeling methods in which indicator molecules are localized at or near the cell soma (Chen et al., 2020; Shemesh et al., 2020), as well as illumination patterns that selectively target cells of interest (Fan et al., 2020; Szabo et al., 2014), should improve imaging depths by reducing background fluorescence, which eases detection of neural activation.

As with one-photon imaging, two-photon imaging of neural activity can also benefit from parallel acquisition strategies. By using corresponding arrays of detectors and laser beams to tile the FOV, multifocal multiphoton imaging collects signals from multiple locations at once, allowing larger FOVs, faster frame rates, higher d' values, or combinations thereof (Bewersdorf et al., 1998; Kim et al., 2007; Rumyantsev et al., 2020). However, due to fluorescence scattering, signals excited at one laser focus can be captured by a detector corresponding to another laser beam, leading to crosstalk across image tiles. If the spatial separation between laser foci is sufficiently large (e.g., 1 mm), scattering across tiles is not too severe and can be computationally unmixed (Rumyantsev et al., 2020) (Figures 3C and 3D). However, scattering increases with depth, so the maximum depth will be less than with a single-beam system that is optimized for deep imaging. When more beams and/or a higher density of beams are used, the trade-offs become more severe. For example, a two-photon microscope with a 20 × 20 array of beamlets and a camera for detection could image 95,000–211,000 μm^2 areas at rates up to 1 kHz (Figure 5B). This microscope yielded a ~10-fold improvement in Ca^{2+} spike-timing precision, albeit with diminished imaging depth, as compared with conventional two-photon microscopy (Zhang et al., 2019). As new detector technologies emerge (Modi et al., 2019), two-photon microscopes that use semiconductor photodetector arrays, cameras, or multiple standalone detectors will further boost capabilities for parallel readout of neural activity.

Another strategy for boosting the speed and coverage of two-photon imaging is to superpose signals from multiple sample locations onto individual photodetectors. By engineering the form of laser illumination, one can excite fluorescence at multiple locations as part of such a parallel readout strategy. Some basic concepts about optical resolution are helpful for understanding this approach.

The point spread function (PSF) of a laser-scanning microscope specifies a weighted set of spatial locations, centered about the laser focus, at which fluorescence signals are excited and sampled. In a conventional two-photon microscope, a beam with an approximately Gaussian cross-sectional intensity profile is focused to a spot whose lateral and axial extents are jointly set by the numerical aperture (NA) of the focus (Figure 5C, left). To decouple the lateral and axial resolution and attain a PSF that is approximately isotropic and about the size of a cell body, temporal focusing supplements the normal geometric focusing achieved by the objective lens (Figure 5C, middle). Specifically, using a diffraction grating, the ~10 nm range of wavelengths in an ultrashort (~100 fs) laser pulse is spread out across the back aperture of the objective lens. The different colors of light reconverge at the geometric focal spot, where the pulse regains its original ~100 fs duration. At other planes in the sample, the pulse is broadened in time, because the pulse's brevity is contingent on the spatial overlap of light of different colors. This in turn reduces two-photon excitation outside the focal plane, which declines inversely with pulse duration, and leads to another form of optical sectioning (Oron et al., 2005; Zhu et al., 2005). The extent of this temporal focusing effect can be set independently of the beam's geometric NA, which allows one to make the axial sectioning from temporal focusing roughly comparable to the lateral width of the PSF. A recent microscope used this temporal focusing approach to create a PSF with a ~5 μm (FWHM) lateral width and ~15 μm axial sectioning (Weisenburger et al., 2019). This ~100-fold expansion in the focal volume over that in conventional two-photon microscopy allowed an

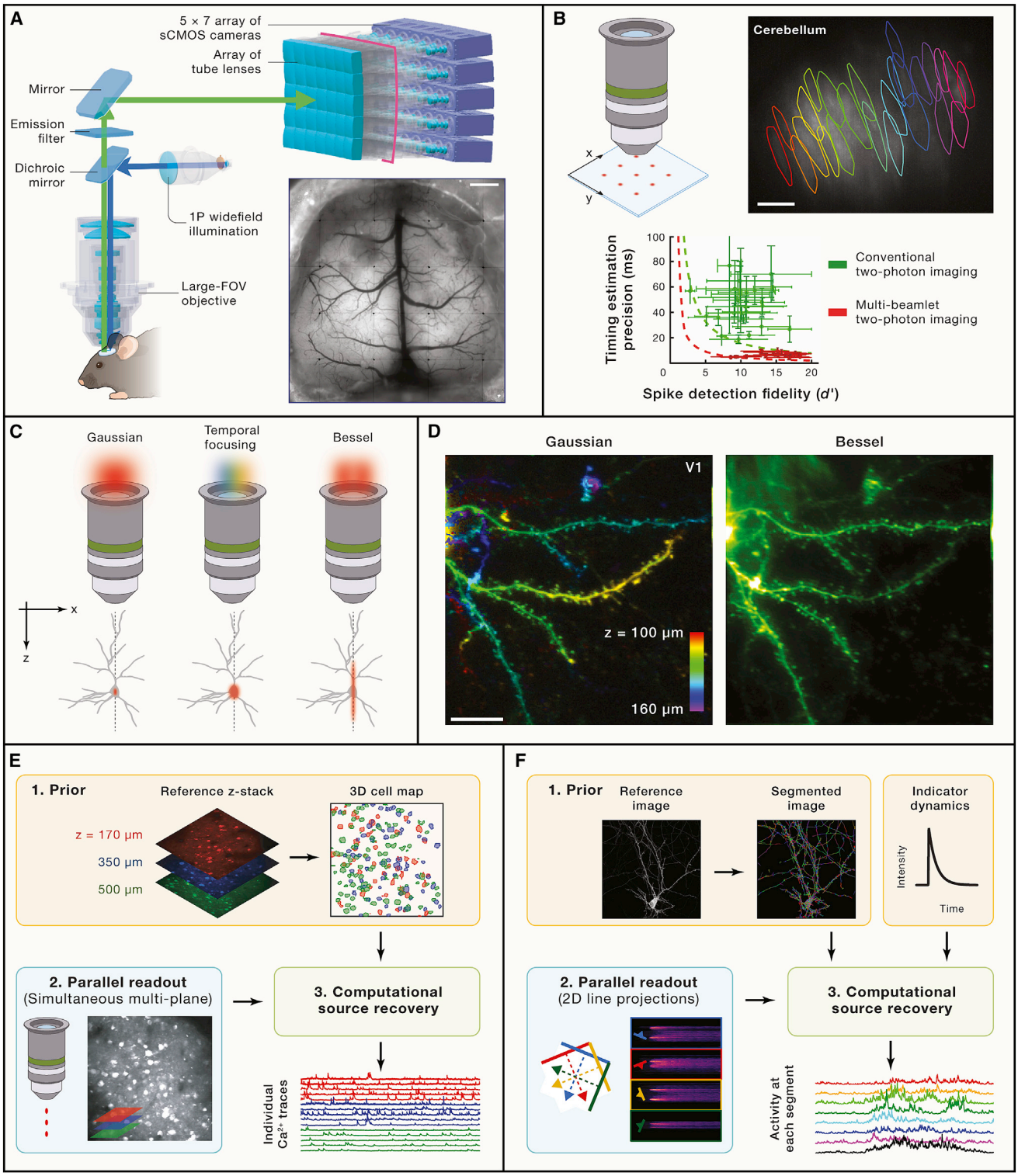

Figure 5. Imaging neural activity using parallel readout strategies

(A) Schematic of an epi-fluorescence mesoscope based on an array (5 × 7) of cameras. This system allowed 30-Hz imaging of neural Ca^{2+} activity across the neocortical surface (10 × 12 mm FOV) with 0.8-µm-wide pixels. Inset: Maximum projection image of the neocortex of a Thy1-GCaMP6s mouse; the boundaries between image tiles are just barely visible. Scale bar, 1 mm.

(B) Top left: a high-speed camera and an array of 400 laser focal spots that was swept laterally across the specimen plane allowed high-speed (0.1–1 kHz) two-photon imaging of neural activity. Top right: this approach enabled imaging of dendritic Ca^{2+} spiking by cerebellar Purkinje cells (colored outlines) at a 100-Hz

(legend continued on next page)

entire cell body to be sampled at once, for 5 Hz volumetric Ca^{2+} imaging of > 10,000 cell bodies in a 1 mm × 1 mm × 0.6 mm cortical region.

While engineering the PSF to sample an entire cell soma is one form of parallel readout, other strategies shape the laser illumination to cover multiple cells concurrently, such as by using elongated focal spots (Lu et al., 2020, 2017) or computer-generated holograms (Nikolenko et al., 2008; Papagiakoumou et al., 2008; Yang et al., 2016). Separating the signals from different cells makes use of an *a priori* assumption that neural activity is relatively sparse in space and time, allowing *a posteriori* computational reconstructions of the most likely neural activity patterns that gave rise to an observed fluorescence signal.

A simple way to create an axially elongated PSF for two-photon imaging while confining its lateral extent is to use an axicon lens to convert a Gaussian laser beam into a Bessel beam, namely a beam with a cross-sectional amplitude profile described by a Bessel function (Thériault et al., 2013). PSFs attained by focusing a Bessel beam into tissue can have sub-micron lateral breadth but extend ~50–100 μm axially (Figure 5C, right). When swept laterally, the elongated focal spot samples a volume that is far more extended in depth than the thin optical sections obtained with a conventional laser focal spot; images acquired with a Bessel beam retain high resolution in the lateral dimensions but are more like projections in the axial dimension. Using Bessel beam scanning, Lu et al. (2017) sampled Ca^{2+} activity in sparsely distributed dendritic spines across a 60 μm depth span (Figure 5D). A stereoscopic variant of this approach, which uses a pair of elongated laser foci that cross one another in the sample, encodes a cell's axial depth in the lateral displacement between the duplicate images of each cell generated by the two beams (Song et al., 2017).

When fluorescence photons arising from multiple locations are captured by a single pixel detector in the same data-acquisition cycle, in general it is not possible to disentangle the signal contributions without further information. However, given additional knowledge about the sample, one can computationally reconstruct the fluorescence contributions from the different sources. For instance, knowledge of cells' spatial locations can be very useful for separating signals from different neurons. A demonstration of this used conventional two-photon microscopy to first identify the locations and shapes of cortical neurons in 3 different axial planes. Neural activity in the 3 planes was then sampled concurrently using a holographic laser illumination pattern with 3 focal spots, one in each of the planes (Yang et al., 2016) (Figure 5E). The anatomic dataset then facilitated computational reconstructions of the cells' Ca^{2+} activity traces from the data in which signals from the 3 planes were superposed, allowing the cells' signals to be unmixed. In comparison to serial sampling of multiple planes, this scheme increases the volumetric imaging rate *N*-fold, where *N* is the number of focal spots in the hologram and thus the number of planes sampled concurrently. Prior knowledge of sample structure can also be used to boost imaging rates when sampling a single axial plane. By sweeping 4 lines of laser illumination in a horizontal plane, with the line orientations spaced at 45° intervals, one study reconstructed neurotransmitter release dynamics along cortical dendrites at a 1 kHz frame-acquisition rate over a 250-μm-wide FOV (Figure 5F) (Kazemipour et al., 2019).

In general, performance improvements attained by using prior knowledge of the sample structure hinge on the extent to which the set of activity sources is truly sparse (Yang et al., 2016); this criterion becomes harder to satisfy with dense labeling of cells and as more planes are sampled. Improved algorithms for disentangling signals from dense sets of overlapping cells, such as by using the temporal statistics of their dynamics (Inan et al., 2021), will drive continued progress in this area, for parallelized imaging using one- or two-photon excitation. Next-generation

frame rate across a 450 × 300 μm FOV. Scale bar, 50 μm. Bottom: In comparison to Ca^{2+} imaging data taken by conventional (10 Hz) two-photon microscopy (green data points), multi-beamlet (100 Hz) two-photon imaging (red data points) achieved ~10-fold better Ca^{2+}-spike-timing estimation precision (y axis), with comparable or better values of spike detection fidelity (x axis). Each data point shows results from an individual Purkinje neuron. Dashed curves represent theoretical limits on spike-timing accuracy for 100-Hz imaging (red curve) and 10-Hz imaging on the conventional two-photon microscope (green curve), computed using the Chapman–Robbins lower bound on the variance of an unbiased estimator (Wilt et al., 2013). Error bars, s.e.m. over all spikes recorded for each cell.

(C) The point-spread function (PSF) of a two-photon microscope describes the spatial distribution of two-photon excited fluorescence relative to the centroid of the laser focal spot. Left: in a conventional two-photon microscope, a laser beam with a cross-sectional intensity profile that is approximately Gaussian yields a PSF with sub-micron lateral width (x axis) and micron-scale axial (z axis) extent. Middle: by using a temporally focused beam for two-photon excitation, the PSF can be enlarged laterally while retaining micron-scale axial sectioning. Right: by using Bessel-beam illumination for two-photon excitation, the PSF can be axially elongated to the hundred-micron-scale while retaining sub-micron widths.

(D) Two-photon imaging of GCaMP6s activity in neural dendrites and spines in mouse visual cortex using Bessel-beam illumination. Left: mean projection image of a volumetric image stack spanning 60 μm in depth, in which each image slice was acquired sequentially using a Gaussian beam and a PSF with a 1.4 μm axial FWHM. Colors encode axial depths below the pial surface. Right: image of the same dendrites and spines obtained by scanning a Bessel beam that yielded a PSF with a 35 μm axial FWHM. Imaging with the Bessel beam led to ~20-fold higher temporal resolution than the conventional approach. Scale bar, 20 μm.

(E) One can track neural Ca^{2+} activity in multiple axial planes concurrently by first mapping neurons' locations and then using this information to unmix neural Ca^{2+} activity traces from superposed multi-plane Ca^{2+} data. (1) First, conventional two-photon microscopy is used to map the neurons' locations (3 planes denoted in different colors). (2) Holographic laser illumination provides multiple focal spots, one in each of the 3 axial planes. The 3 spots are laterally scanned in parallel, allowing the 3 planes to be simultaneously sampled. This yields superposed images of fluorescence from the different planes. (3) Ca^{2+} activity traces of individual cells are recovered from the superposed data using their previously determined shapes and locations. Overall, this strategy increases the volumetric imaging rate by a factor of *N*, where *N* is the number of planes sampled in parallel.

(F) Anatomic data and statistical estimation can also be used to boost the speed at which neural dynamics are tracked in one axial plane. (1) Using conventional two-photon microscopy, one acquires a high-resolution image of a specimen that is sparsely labeled with a neural activity indicator. Structures of interest, such as dendrites, are divided into discrete segments, each of which will be assigned an individual activity trace. (2) To acquire activity data, 4 lines of laser illumination with different orientations are swept sequentially across the specimen plane of interest. In this way, multiple neural segments are sampled in parallel. (3) Using a statistical estimator that accounts for the segments' morphology and indicator kinetics, activity traces are reconstructed for each segment. This approach allowed reconstructions of glutamate release dynamics in neocortical dendrites across a 250-μm-wide FOV.

(A) is adapted from Fan et al. (2019). (B) is adapted from Zhang et al. (2019). (D) is adapted from Lu et al. (2017). (E) is adapted from Yang et al. (2016). (F) is adapted from Kazemipour et al. (2019).

microscopes might also combine two or more of the parallel readout strategies discussed here, for instance by using spatiotemporally multiplexed arrays of beams, each with its own engineered PSF or holographic illumination pattern.

IMAGING DEEPER INTO TISSUE

In opaque tissue, photon propagation along ballistic trajectories is attenuated by both light scattering and light absorption. The former effect is generally far more severe than the latter across the visible to near-infrared wavelengths (400–1,300 nm). However, scattering declines with increases in wavelength, and for wavelengths >1,400 nm, absorption by water becomes significant (Wang et al., 2018b). Both scattering and absorption attenuate light as an exponential function of the distance into tissue; the attenuation length-constant denotes the penetration distance at which the intensity of incident ballistic illumination is reduced via both these processes by a factor $1/e$. Exact values vary between brain regions and as a function of the animal's age, but attenuation lengths in the adult mouse brain are about ~60 μm for 450–550 nm light (Al-Juboori et al., 2013), ~130 μm for 775 nm, and ~290 μm for 1,280 nm (Kobat et al., 2009). The reduced attenuation of light of longer wavelengths points to a basic strategy for imaging deeper into tissue.

In two-photon microscopy, the combination of infrared illumination and wide-field fluorescence detection enables greater imaging depths than those attainable with confocal fluorescence microscopy. Recent work has further improved the penetration of two-photon microscopy by addressing two impediments to deeper imaging.

One important line of research has sought to address the exponential loss of ballistic illumination photons, which are needed to excite two-photon fluorescence at the laser focus. This work has pursued red-shifted Ca^{2+} indicators (Dana et al., 2016; Inoue et al., 2019), which use longer excitation wavelengths that scatter less and thus allow deeper imaging. For example, use of an R-CaMP and 1,100 nm excitation enabled two-photon Ca^{2+} imaging to a depth of 1,100 μm in mouse prelimbic cortex at cellular resolution, though with high illumination powers (~180 mW) at the brain surface (Kondo et al., 2017). These power levels are notably higher than those used for two-photon imaging of prelimbic cortex with an implanted microendoscope (~50 mW) but still within tolerable levels (Podgorski and Ranganathan, 2016).

Another line of research has sought to address the limitation that, even with long excitation wavelengths, imaging at depth is compromised by aberrations of the illumination beam. These aberrations constitute distortions to the beam's optical wavefronts and arise from refractive index inhomogeneities that are intrinsic to tissue and because commercial objective lenses are engineered to minimize aberrations under a narrow set of optical conditions that do not include imaging ~1 mm into tissue. Brain tissue is a mixture of constituents (water, proteins, lipids, etc.) with varying refractive indices. Microscopic variations in refractive index distort the propagation of the illumination beam, broadening the focal spot and reducing the efficiency of two-photon excitation (Ji et al., 2012; Schwertner et al., 2004). Adaptive optical methods aim to correct these distortions. Microscopes with adaptive optical capabilities measure the wavefront distortions of the illumination beam and then impose a compensatory distortion, using a programmable correction element such as a deformable mirror (Ji, 2017). To date, adaptive optical two-photon microscopes have succeeded more at improving the spatial resolution and signal-to-noise ratio when imaging at depth than at extending the attainable depths for imaging neural ensemble activity. Successes include imaging of Ca^{2+} and glutamate activity at the resolution of single dendritic spines up to 850 μm deep in cortex (Liu et al., 2019; Wang et al., 2015). However, adaptive optics does not mitigate the exponential decline of ballistic illumination with depth, the chief obstacle to imaging deeper.

To further boost two-photon excitation for deep imaging, one can use a regenerative laser amplifier that provides comparable time-averaged illumination powers to a typical ultrashort-pulsed laser but with ~1,000-fold higher pulse energies and ~1,000-fold lower emission rates (Theer et al., 2003). This strategy works only up to a point (~800–1,000 μm in depth), since beyond these depths the intense illumination needed for deep imaging excites substantial background fluorescence near the brain surface, overwhelming the fluorescence signals generated by the exponentially attenuated laser focus (Theer and Denk, 2006). To overcome this limitation, researchers have turned to three-photon microscopy, another form of laser-scanning multiphoton fluorescence imaging.

Three-photon microscopy relies on coincident absorption of three photons for fluorescence excitation (Wang and Xu, 2020). Compared to two-photon microscopy, three-photon imaging has steeper optical sectioning, which suppresses background fluorescence arising at the brain surface. Further, three-photon imaging uses longer-wavelength illumination than two-photon microscopy, which reduces scattering and allows three-photon microscopy to penetrate deeper. It can even reach the adult mouse hippocampus through an intact neocortex (Horton et al., 2013; Ouzounov et al., 2017). Notably, this entails imaging past the highly scattering white matter atop the hippocampus, which was not possible with two-photon excitation of R-CaMP (Kondo et al., 2017).

Notwithstanding its virtues for deep imaging, three-photon microscopy involves challenges related to the difficulty of generating three-photon excitation (Wang and Xu, 2020; Yildirim et al., 2019). The miniscule cross-sections for three-photon absorption (~10^{-75} $m^6 \cdot s^2$) necessitate the use of light sources with shorter pulse durations (35–60 fs) and higher pulse energies than those typically used for two-photon imaging. The longer wavelength illumination (~1,300–1,700 nm) is also absorbed more by tissue than that for two-photon imaging, which increases brain heating and limits illumination powers. To keep the net illumination power at tolerable levels, the higher pulse energies necessitate lower pulse emission rates, which in turn limits three-photon imaging frame rates to <10 Hz in most cases (Ouzounov et al., 2017; Wang and Xu, 2020; Yildirim et al., 2019).

To evaluate how the above factors—attenuation of illumination, fluorescence signal excitation, and suppression of background fluorescence—influence multiphoton Ca^{2+} imaging, signal detection theory provides a framework to calculate d' values for detection of neural Ca^{2+} transients. These analyses

indicate that, when using GCaMP6s, three-photon Ca^{2+} imaging with 1,300 nm illumination provides superior d' values than two-photon imaging with 920 nm illumination at depths >600 μm (Wang et al., 2020; Wang and Xu, 2020). The results also suggest ways to enhance imaging at different tissue depths by identifying an optimal combination of pulse energy, emission rate, and average illumination power for each depth.

Notably, recent work has sought to optimize nearly every aspect of three-photon microscopy with short, energetic pulses (Yildirim et al., 2019), make head-mounted three-photon microscopes for use in freely behaving rats (Klioutchnikov et al., 2020), and create novel light sources that increase the frame rate and detection fidelity of three-photon Ca^{2+} imaging (Li et al., 2020). The use of an adaptive excitation laser source and modest illumination levels (~35 mW; 1,700 nm light) recently enabled three-photon Ca^{2+} imaging of jRGECO1a at a frame-rate of 30 Hz across a 620-μm-wide FOV at 750 μm deep in tissue (Li et al., 2020). Thus, commercial availability of such lasers could make video-rate Ca^{2+} imaging in the infragranular layers of the mouse cortex routinely feasible. Improvements in red-shifted Ca^{2+} indicators will also benefit the signal quality and depth in tissue that are attainable with multiphoton Ca^{2+} imaging.

MONITORING AND MANIPULATING NEURAL ACTIVITY WITH SINGLE-CELL RESOLUTION

To establish the causal significance of neural population codes, neuroscientists need methods for manipulating subsets of cells chosen based on their coding properties. The combination of neural Ca^{2+} imaging and two-photon optogenetics fulfills this need, as it enables concurrent readout and manipulation of neural activity in behaving animals at single-cell resolution.

Along with the growing toolkit of activity indicators, the set of optogenetic actuators for control of neural activity has also expanded in recent years. Nearly all optogenetic actuators are based on proteins of the opsin family (Zhang et al., 2011). An exciting development of recent years has been the combined use of imaging and optogenetics, to monitor and manipulate neural activity concurrently in live animals (Emiliani et al., 2015). However, concurrent imaging and optogenetic manipulations necessitate careful consideration of possible crosstalk.

Namely, illumination intended for imaging may also excite the opsin, perturbing the very neural activity that one aims to monitor. To achieve spectral separation, opsin engineering has yielded red-shifted opsins that have peak one-photon absorption wavelengths near ~600 nm (Chuong et al., 2014; Klapoetke et al., 2014; Lin et al., 2013; Marshel et al., 2019) rather than 450–490 nm typical of channelrhodopsin-2 (ChR2) (Boyden et al., 2005). To date, most studies combining Ca^{2+} imaging and optogenetics have utilized red-shifted opsins and green GECIs. However, opsins' absorption spectra typically extend far into the blue part of the visible spectrum, leading to proposals that it might be better to combine blue opsins with red-shifted GECIs instead (Forli et al., 2018). In either spectral arrangement, minimizing the power of the imaging illumination laser and its dwell time at individual locations within the FOV are both important to reduce opsin excitation. Restricting the spatial spread of opsin expression via soma-targeting sequences in the opsin transgene has also helped to reduce crosstalk (Baker et al., 2016; Mardinly et al., 2018; Shemesh et al., 2017).

Integration of optogenetics and imaging is aided by the compatibility of opsins with either one- or two-photon excitation. The former allows bulk actuation of genetically or projection-defined neural populations, in the same FOV as two-photon Ca^{2+} imaging (Otis et al., 2019) or at separate anatomic sites (Wagner et al., 2019). The latter permits precise targeting of cells that are user selected according to their activity patterns, enabling all-optical two-photon Ca^{2+} imaging and two-photon optogenetics studies that both monitor and manipulate a neural ensemble's dynamics (Packer et al., 2015; Rickgauer et al., 2014). Since two-photon optogenetics uses tabletop optical hardware, these studies have been limited to head-fixed mice. By comparison, the integration of one-photon optogenetics and Ca^{2+} imaging has been achieved in freely moving mice (Owen et al., 2018; Stamatakis et al., 2018; Szabo et al., 2014).

Constraints from opsin photophysics guide the design of illumination strategies for two-photon optogenetics. Crucially, opsins' two-photon absorption cross-sections are greater than those of many fluorophores, but the photocurrents from each opsin molecule are miniscule (Rickgauer and Tank, 2009). When photoactivated, a single ChR2 molecule passes ~1–10 fA (Feldbauer et al., 2009). To alter a cell's spiking activity, which typically requires evoked currents of >1 nA (Mattis et al., 2011), many ChR2 molecules must be activated at once. Initial work in two-photon optogenetics identified two illumination strategies, spiral scanning and whole-cell illumination, for eliciting spikes from individual cells expressing excitatory opsins (Andrasfalvy et al., 2010; Packer et al., 2012; Papagiakoumou et al., 2010; Rickgauer and Tank, 2009). Later work extended these illumination methods to optogenetic inhibition (Forli et al., 2018; Mardinly et al., 2018; Prakash et al., 2012). Both methods use infrared, ultrashort-pulsed lasers similar to those typically used for two-photon Ca^{2+} imaging, except that the lasers used for two-photon optogenetics now commonly have higher pulse energies and lower pulse emission rates than those for two-photon imaging (Figure 6A).

In the spiral-scanning approach, a micron-sized laser focus is rapidly swept in a spiral pattern over the soma of an excitatory opsin-expressing neuron (Rickgauer and Tank, 2009). To evoke spiking, the pattern must cover all or most of the cell body in a time interval that is briefer than the opsin's deactivation time-constant, which is typically ~1–100 ms (Mattis et al., 2011; Sridharan et al., 2021). In contrast, whole-cell illumination uses a broad laser focal spot (~10 μm wide) to simultaneously excite opsins across the cell body. Because such expanded foci compromise optical sectioning, whole-cell illumination is usually combined with temporal focusing, which confines opsin excitation to an axial section <5 μm thick (Andrasfalvy et al., 2010; Papagiakoumou et al., 2010; Rickgauer et al., 2014).

The two illumination approaches have complementary strengths and limitations, and each can be applied serially or in parallel across multiple neurons. Spiral scanning is typically used with opsins with prolonged deactivation time-constants (>30 ms) but is generally more power efficient than whole-cell illumination, allowing more cells to be stimulated at once given a fixed average power (Picot et al., 2018; Yang et al., 2018). In

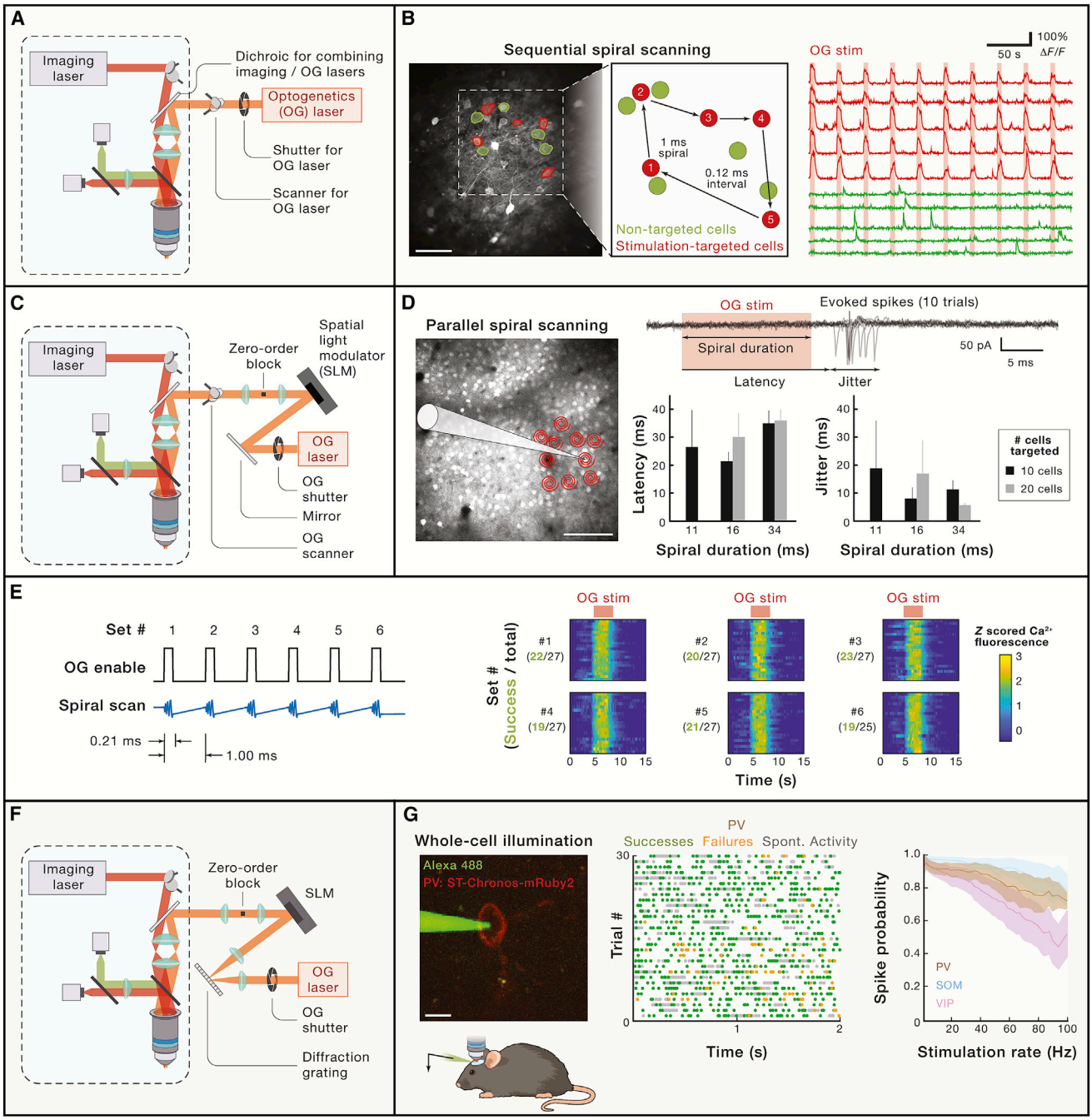

Figure 6. Integrated two-photon optogenetics and two-photon Ca^{2+} imaging

(A) Diagram of an instrument that combines conventional two-photon microscopy with basic two-photon optogenetics (OG) capabilities. Separate lasers provide illumination for imaging and optogenetic control, and there are two different pairs of laser scanners for steering each focal spot. In (A), (C), and (G), the dashed boxes enclose components comprising a standard two-photon microscope. Key components needed for optogenetic studies are shown outside the boxes.

(B) Using the system of (A), Jennings et al. (2019) stimulated up to 20 neurons selected based on their Ca^{2+} activity patterns. Left: a two-photon image of mouse orbitofrontal cortical (OFC) neurons expressing the Ca^{2+} indicator, GCaMP6m, and a red-shifted excitatory opsin, bReaChES. Red outlines mark cells chosen for optogenetic stimulation; green outlines mark nearby cells that were not targeted. Scale bar, 100 μm. Middle: a schematic of the boxed region shown at left, with cells depicted as colored circles. The scanner controlling the optogenetics beam sequentially targeted each of the numbered cells and applied a 1-ms-duration spiral scan of the focal spot to each cell body. During the ~0.12 ms time needed for the scanners to switch between cells, the optogenetic illumination was electro-optically shuttered. Right: Ca^{2+} activity traces of targeted (red) and non-targeted (green) cells. Red shading denotes intervals when optogenetic stimulation was applied.

(C) Schematic of a two-photon imaging system that can optogenetically manipulate multiple cells in parallel by applying spiral laser scans to each of them concurrently. In addition to the apparatus of (A), the system includes a programmable spatial light modulator (SLM) that splits the optogenetics laser beam into multiple beamlets, each of which targets one user-selected cell. The zero-order block blocks undiffracted light from the SLM.

(legend continued on next page)

contrast, whole-cell illumination is compatible with the fastest opsins (e.g., Chronos; ~4 ms deactivation time-constant), which allows generation of high-frequency, temporally precise spike trains and manipulations of cells with high basal spiking rates while also reducing occurrences of spurious, extra spikes that can occur following optogenetic activation of cells expressing slower opsins (Mardinly et al., 2018; Ronzitti et al., 2017). In both cases, however, the inability to reliably detect single action potentials by Ca^{2+} imaging implies that one can only infer statistically that cells show the desired spiking patterns, since optically evoked spiking can only be directly confirmed by electrical recordings, which cannot be done for every targeted cell. Thus, in most studies to date that utilize two-photon optogenetics, researchers have simply aimed to excite a burst of spikes, and the exact number and timing of evoked spikes have remained variable from trial to trial.

When using two-photon optogenetics, one must specify the timing with which different cells are illuminated. A simple approach is to illuminate individual cells sequentially, with the order typically set by the cells' proximities to one another (Figure 6B). This approach has revealed neurons' causal influence on animal behavior and interactions among neural ensembles. For example, sequential activation of up to 20 orbitofrontal cortical cells with a spirally scanned laser focal spot modulated the feeding patterns of food-restricted mice, in a bi-directional manner that depended on the coding properties of the cells chosen for illumination (Figures 6A and 6B) (Jennings et al., 2019). Optogenetic activation of hippocampal place cells with sequential, whole-cell illumination led to activity changes in non-targeted cells with place fields similar to those of the illuminated cells (Rickgauer et al., 2014).

A drawback of sequential targeting is that activating one cell at a time limits the temporal precision with which activity can be synchronously evoked across multiple cells, and this constraint grows more severe with the number of targeted cells. Parallel illumination allows greater synchrony, even across cells lying in different axial planes, but it usually requires laser beams of higher power that can be split and directed to multiple cells at once. In one parallel illumination strategy, based on principles of computer-generated holography, an excitation laser beam diffracts off a digitally controlled, spatial light modulator (SLM) that splits the beam into multiple beamlets (Nikolenko et al., 2008; Packer et al., 2012); each beamlet is focused onto one cell and spirally scanned by a pair of scanning mirrors that is shared by all the beamlets (Figures 6C and 6D) (Packer et al., 2015). This approach can synchronously stimulate a targeted cell population with a timing precision that is bounded by the kinetics of the opsin, illumination power, and spiraling parameters (Figure 6D).

Recent implementations of such parallel spiral scanning have used laser sources with lower repetition rates and higher pulses energies than those typically used for two-photon imaging, allowing the energy to be split across ~50 stimulated cells at once (Yang et al., 2018). However, concurrent illumination of many cells does not guarantee responses in every cell, as only ~80% of targeted cells showed measurable Ca^{2+} activation in response to each illumination bout (Yang et al., 2018). By rapidly updating the SLM to target the beamlets to distinct subsets of cells, even more cells can be addressed in near simultaneity. By illuminating sets of 20–30 cortical cells in parallel using spiral scans of 210 μs duration, and by using an SLM system that could be updated in 1 ms to create a new beamlet pattern, Marshel et al. (2019) stimulated up to 6 different sets of cells (~100–160 cells total) within intervals as brief as ~5 ms for studies of visual coding (Figure 6E).

Whole-cell illumination has also been parallelized to address sets of up to ~50 cells that are distributed in three dimensions in brain tissue (Figure 6F) (Hernandez et al., 2016; Pégard et al., 2017), with greater cell counts likely coming soon (Sridharan et al., 2021). The joint use of a fast, soma-targeted opsin and whole-cell illumination allowed stimulation of 80 Hz spike trains in cortical interneurons (Figure 6G), in which individual neurons fired a spike with >50% probability in response to each burst of illumination (Mardinly et al., 2018).

Going forward, we expect that mesoscopes for two-photon Ca^{2+} imaging will increasingly include two-photon optogenetic capabilities across FOVs a millimeter wide or more (Marshel et al., 2019). Increasing the numbers of cells that can be manipulated simultaneously may require ultrashort-pulsed lasers of

(D) Using the system of (C), Packer et al. (2015) stimulated 10–20 neurons at once. Cell-attached electrical recordings revealed the temporal precision with which two-photon optogenetics evoked spiking. Left: a two-photon image of somatosensory cortex in which layer 2/3 pyramidal cells expressed GCaMP6s and the red-shifted excitatory opsin C1V1. Red spirals mark cells that were optogenetically targeted with parallel spiral scanning. A glass microelectrode was used to perform a loose patch electrical recording of one of the targeted neurons. Scale bar, 100 μm. Top right: a set of electrical traces of neural activity from 10 trials in which the cell was optogenetically stimulated using spiral scanning (red-shaded interval). Bottom right: the electrical traces permit quantification of the mean latency to spike and the timing jitter across trials, for different durations of spiral scanning and either 10 or 20 targeted cells.
(E) Using a soma-targeted variant of the excitatory opsin ChRmine and a larger version of the instrument in (C) capable of activating more cells, Marshel et al. (2019) stimulated >100 user-selected neurons by rapidly switching between different sets of 20–30 cells. Left: timing protocol for targeting 6 different sets of neurons. Each set of cells was stimulated with a 0.21-ms-duration spiral scan, and a different set was targeted every millisecond. Right: Z scored Ca^{2+} activity traces for the 6 different sets of cells, with each line showing an optogenetically evoked response of an individual cell that was successfully activated. The number of cells that were successfully activated out of the total targeted is shown for each set. In total, 124 of 160 cells targeted were successfully activated.
(F) Schematic of a two-photon microscope in which holography and temporal focusing allow two-photon optogenetic control of multiple cells that are each illuminated with a disk of laser light. Note the lack of a scanner in the optogenetics illumination pathway. Using this system, Mardinly et al. (2018) optogenetically manipulated up to ~50 neurons at once.
(G) Electrophysiological validation of the system of (F). Left: using a loose-patch electrical recording (glass microelectrode filled with green dye) of a parvalbumin-positive (PV) interneuron expressing the fast excitatory opsin Chronos and the red fluor mRuby2, Mardinly et al. (2018) measured the reliability with which they could optogenetically evoke single spikes. Scale bar, 10 μm. Middle: raster plots of activity from an individual PV neuron that was stimulated at time points separated by Poisson-distributed intervals (mean rate of stimulation: 30 Hz). Green dots mark instances in which stimulation evoked an action potential. Orange dots mark failures to spike. Grey dots mark spontaneously emitted spikes. Right: probability of successful spiking per stimulation attempt in PV, somatostatin (SOM), and vasoactive-peptide (VIP) interneurons, as a function of the stimulation rate.
(A) and (B) are adapted from Jennings et al. (2019). (C) and (D) are adapted from Packer et al. (2015). (E) is adapted from Marshel et al. (2019). (F) and (G) are adapted from Mardinly et al. (2018). (C) and (F) were redrawn using graphical elements from Jennings et al. (2019).

even higher pulse energies than are used today, enabling this energy to be distributed across a greater number of targeted cells. Unlike two-photon imaging, two-photon optogenetics typically involves only brief periods of illumination so that brain heating is usually less of a problem. However, as one optogenetically manipulates more cells for sustained periods and within a limited tissue volume, local rises in brain temperature become more of a concern.

A key issue for all-optical studies combining large-scale Ca^{2+} imaging and two-photon optogenetics is the inability to reliably detect single action potentials by Ca^{2+} imaging. Attaining single-spike sensitivity in Ca^{2+} imaging would enable highly precise optogenetics experiments in which one could verify with high confidence the spiking patterns imposed across many neurons. This in turn would allow detailed studies of how even small differences in spike numbers, timing, and synchrony may impact downstream brain areas and animal behavior (Mardinly et al., 2018). As GECIs and microscopes covering multiple brain areas progress, the integration of optogenetics and imaging will facilitate causal studies of such issues across interconnected brain regions.

VOLTAGE IMAGING AT SINGLE-SPIKE RESOLUTION IN LIVE ANIMALS

While Ca^{2+} imaging has not yet achieved reliable, single-spike resolution in live mammals, the attainment of this capability with genetically encoded voltage indicators (GEVIs) and high-speed one-photon fluorescence imaging was a major milestone (Gong et al., 2015). This has opened the door to voltage imaging studies of spiking patterns in genetically defined or projection-targeted neuron classes that would be infeasible with electrophysiological methods (Fan et al., 2020; Kannan et al., 2021; Piatkevich et al., 2019). Further, since GEVIs directly sense the transmembrane potential, unlike GECIs they can report hyperpolarizations and other sub-threshold voltage dynamics that are usually inaccessible by Ca^{2+} imaging. Major gains in GEVI performance over the past decade were enabled by increases in the speed, brightness, and signaling dynamic range of existing GEVI families (Barnett et al., 2012; Jin et al., 2012), new voltage-sensing mechanisms (Gong et al., 2014; Kralj et al., 2011; St-Pierre et al., 2014), optimized membrane localization (Dimitrov et al., 2007) and sub-cellular targeting (Baker et al., 2016), and the use of rapid screening platforms (Kannan et al., 2018; Piatkevich et al., 2018; Villette et al., 2019). In high-speed imaging studies (~0.5–1 kHz), multiple recent GEVIs can now capture high-frequency spike trains with ~1 ms resolution in live animals (Figure 7) (Abdelfattah et al., 2019; Adam et al., 2019; Fan et al., 2020; Gong et al., 2015; Huang et al., 2018; Kannan et al., 2018; Lin and Schnitzer, 2016; Piatkevich et al., 2019; Villette et al., 2019).

Historically, several factors made it challenging to design GEVIs of broad utility, and there were theoretical arguments as to whether voltage imaging with single-spike sensitivity would ever be feasible (Sjulson and Miesenböck, 2007). The challenges are several. To sense the transmembrane voltage, GEVIs must integrate into the cell membrane, limiting the source of useful fluorescence signals to a two-dimensional surface, in contrast to GECIs that fill the cytosolic volume. To report spikes with millisecond-scale precision, a GEVI must have voltage-dependent responses on this same timescale, usually leaving only from one to a few milliseconds for the fluorescence spike waveform. Due to these factors, detecting single spikes *in vivo* usually requires strong illumination that bleaches the GEVI much faster than bleaching in a typical Ca^{2+} imaging study. Adding to these challenges, most cameras and two-photon microscopes still lack the kilohertz image frame-acquisition rates needed to resolve single action potentials, so advances in optical instrumentation remain needed to bring voltage imaging to full fruition.

Key metrics for GEVIs include their brightness, dynamic range of voltage signaling (i.e., the relative changes in fluorescence per change in membrane voltage), kinetics (the time-constants of fluorescence changes in response to voltage increases or decreases), and photostability. While greater brightness and photostability are nearly always valuable, different biological experiments benefit from different forms of voltage sensitivity and kinetics. For example, signal detection theory dictates that a GEVI optimized purely for spike detection would be dark at voltages below the spike threshold and rise to a bright fluorescence maximum at voltages just above threshold. In neurons that spike sparsely in time, d' values for spike detection can be raised by prolonging the off time-constant of the fluorescence spike waveform, to boost the net count of fluorescence signal photons (Chamberland et al., 2017; Jin et al., 2012); however, this approach can also hinder resolution of individual spikes fired in rapid succession. To faithfully convert the electrical waveforms of action potentials into fluorescence waveforms, GEVIs with fast kinetics and linear sensitivity across the physiological voltage range are desirable (Hochbaum et al., 2014). To monitor sub-threshold dynamics, GEVIs with greater sensitivity near the resting potential are useful (Villette et al., 2019). In all cases, reducing background fluorescence, such as by improving GEVI localization to the cell membrane, improves signal detection. To image the somatic spiking dynamics of dense sets of neurons, it is generally important to target GEVI molecules to the cell soma and perisomatic region (Baker et al., 2016; Lim et al., 2000), since disentangling fluorescence signal sources from within densely labeled neuropil can be highly challenging. Further, as noted above in our discussion of signal detection theory, this targeting approach reduces background fluorescence and confines voltage indicator molecules near the portion of the cell where spiking signals are strongest, both of which increase spike detection fidelity.

Building on early efforts to create voltage-sensitive fluorescent proteins (Dimitrov et al., 2007; Sakai et al., 2001; Siegel and Isacoff, 1997), recent major strides have involved three main classes of GEVIs. One uses voltage-sensitive protein domains (VSDs), derived from voltage-gated ion channels or phosphatases, whose conformations depend on the transmembrane voltage. In early VSD-based GEVIs, one or a pair of fluorescent proteins was fused to an intracellular terminus of the VSD, such that voltage-dependent VSD movements modulate the activity of the fluorophore (Barnett et al., 2012; Jin et al., 2012) or the fluorescence resonance energy transfer (FRET) efficiency between a pair of fluorophores (Akemann et al., 2010). In newer designs, a circularly permuted GFP is inserted into an extracellular loop of

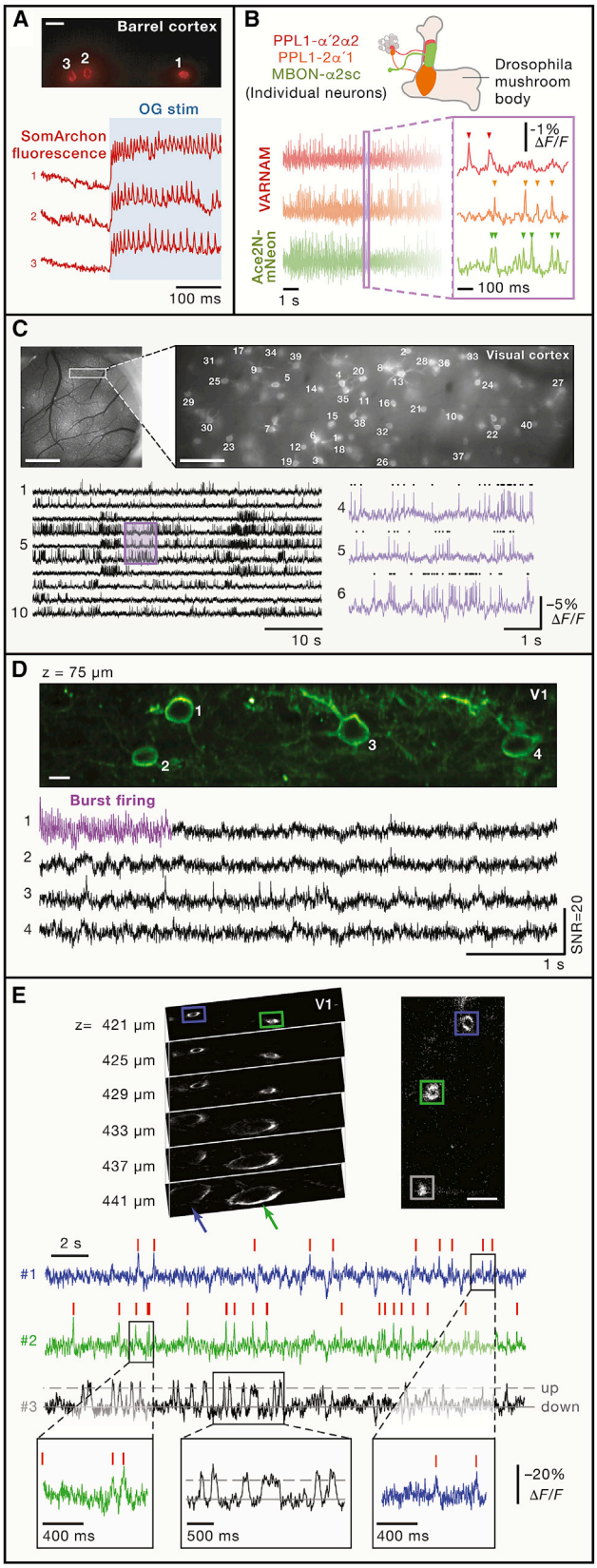

Figure 7. *In vivo* voltage imaging at single-spike resolution

(A) Simultaneous *in vivo* one-photon optogenetic (OG) stimulation and one-photon fluorescence voltage imaging. Top: fluorescence image of 3 interneurons in mouse neocortical layer 1 that co-express the near-infrared voltage-indicator SomArchon and the blue light-activated excitatory opsin SomCheRiff from a bicistronic AAV construct. Scale bar, 20 μm. Bottom: simultaneously acquired fluorescence traces from the 3 cells. Blue shading marks the period when optogenetic stimulation was applied. Images were taken at a 1 kHz frame rate.

(B) Top: in the mushroom body of adult *Drosophila melanogaster*, the PPL1-α′2α2 and PPL1-2α′1 neurons expressed the red fluorescent FRET-opsin voltage indicator, VARNAM. The MBON-α2sc neuron expressed the green fluorescent FRET-opsin, Ace2N-mNeon. Bottom: owing to the anatomic separation of the PPL1-α′2α2 and PPL1-2α′1 cells and the different emission wavelengths of the two indicators, optical voltage traces of spiking activity could be acquired concurrently from all 3 individual neurons. Images were acquired at 500 Hz.

(C) Epi-fluorescence voltage imaging of layer 1 neocortical interneurons in a NDNF-Cre driver mouse line using the soma-targeted (ST) version of the chemical genetic voltage-indicator Voltron$_{525}$. Top left: fluorescence image of Voltron$_{525}$-ST-expressing layer 1 interneurons in the visual cortex. Cortical expression of Voltron clearly exceeds the 1064 μm × 266 μm FOV (boxed area) allowed by the camera when operating at 400 Hz. Scale bar, 1 mm. Top right: magnified view of the area boxed at left. Scale bar, 100 μm. Numbers indicate cells whose voltage activity was imaged simultaneously at a 400 Hz frame rate. Bottom left: optical voltage traces for 10 cells from a portion of a 3 min recording. Bottom right: magnified view of the traces for cells 4–6, for the time period enclosed in the purple box at left. Black dots mark individual action potentials.

(D) Two-photon voltage imaging in the mouse visual cortex using a high-speed raster scanning. Top: 50 × 250 μm area of brain tissue showing 4 cells, 75 μm beneath the pial surface, that express a soma-targeted voltage indicator, ASAP3-Kv, under the control of the synapsin promoter. Scale bar, 10 μm. Bottom: optical voltage traces of spontaneous activity from the 4 cells, including a period of burst firing in one cell (highlighted in purple), taken at a 1 kHz frame rate.

(E) Two-photon voltage imaging of 3 pyramidal cells in mouse neocortical layer 5 that express ASAP3-Kv, performed using random-access laser scanning. Top left: a set of image slices acquired at different axial (z) depths in tissue. Boxed areas indicate apical dendrites, and the color-corresponding arrows mark cell bodies of the same neurons. Top right: a single image slice, showing apical dendrites of 3 individual neurons (colored boxes) at a depth of z = 421 μm. Scale bar, 10 μm. Bottom: traces show the voltage activity of the 3 color-corresponding neurons shown above, sampled at their apical dendrites (3.33 kHz per cell). Red ticks mark occurrences of dendritic spikes. For cell 3, the horizontal gray lines denote voltage levels corresponding to up- and down-voltage states.

(A) is adapted from Fan et al. (2020). (B) is adapted from Kannan et al. (2018). (C) is adapted from Abdelfattah et al. (2019). (D) is adapted from Wu et al. (2020). (E) is adapted from Villette et al. (2019).

a VSD, yielding a GEVI whose fluorescence decreases with membrane depolarization (St-Pierre et al., 2014). While early VSD-based GEVIs lacked the speed and dynamic range for *in vivo* use (Akemann et al., 2010; Jin et al., 2012), recent versions offer millisecond kinetics and high voltage sensitivity, especially near the resting membrane potential, allowing observations of both spiking and sub-threshold activity *in vivo* (Villette et al., 2019).

A second class of GEVIs exploits the voltage-sensitive absorption of light by membrane proteins of the bacteriorhodopsin family (Kralj et al., 2011; Maclaurin et al., 2013). These proteins, such as Archaerhodopsin (Arch), have a proton-pumping photocycle and undergo changes in light absorption upon proton translocation (Kralj et al., 2011; Lanyi, 2004). They are also weakly fluorescent (quantum yield $<10^{-3}$) and allow variations in proton-motive force, such as from membrane voltage changes, to be read out via fluorescence changes (Kralj et al., 2011). Protein engineering improved the kinetics and dynamic range of voltage-dependent signaling and removed the

rhodopsin proton current, enabling imaging of membrane voltage dynamics with millisecond-scale resolution and without the illumination affecting the membrane potential (Flytzanis et al., 2014; Gong et al., 2013; Hochbaum et al., 2014). Rhodopsin fluorescence rises with depolarization and lies in the far red and near infrared, which facilitates deeper imaging and integration with visible-light optogenetics (Figure 7A) (Fan et al., 2020; Hochbaum et al., 2014), but its dimness has necessitated extreme illumination intensities (1–12 W/mm^2) to generate sufficient fluorescence signals (Adam et al., 2019; Piatkevich et al., 2019). Although rhodopsins are highly photostable, wide-field illumination at these intensities can quickly lead to brain heating. Recent studies have targeted illumination selectively to cells of interest, reducing the net illumination power to ~3–30 mW per cell while also minimizing background fluorescence (Adam et al., 2019; Fan et al., 2020). Nonetheless, scaling voltage imaging to hundreds of individual neurons may be problematic with rhodopsin GEVIs due to the required illumination intensities.

GEVIs of a third class, the FRET-opsins, comprise a rhodopsin fused to a genetically encoded fluorescent protein and combine the former's voltage-sensitive light absorption coefficient with the latter's bright fluorescence (Abdelfattah et al., 2019; Gong et al., 2015, 2014; Kannan et al., 2018; Zou et al., 2014). In this design, the rhodopsin acts as a FRET acceptor that quenches the emissions of the bright fluorophore in a voltage-dependent manner. Like VSD-based GEVIs, FRET-opsins are ~2–3 orders of magnitude brighter than rhodopsin GEVIs and need much lower illumination intensities (10–25 mW/mm^2) that should scale to studies of hundreds or thousands of cells (Lin and Schnitzer, 2016; Villette et al., 2019). The modular design of the FRET-opsins and the broad absorption spectra of rhodopsins imply that a single rhodopsin species can be used with different FRET donor fluorophores of distinct colors (Abdelfattah et al., 2019; Gong et al., 2014; Zou et al., 2014). For example, the fast 'Ace' rhodopsin from *Acetabularia acetabulum* has been used as the voltage-sensitive component within green fluorescent Ace-mNeonGreen (Gong et al., 2015), red fluorescent Varnam (a fusion of Ace and mRuby3; Figure 7B) (Kannan et al., 2018), and the Voltron indicators, which are chemogenetic FRET-opsins that combine Ace and a synthetic fluorescent dye (Figure 7C) (Abdelfattah et al., 2019). Having FRET-opsins of different colors has facilitated the integration of optogenetics and voltage imaging and enabled dual-color voltage imaging as a way of tracking distinct neuron types concurrently in live animals (Kannan et al., 2018). Using a highly photostable dye as the FRET-donor can prolong imaging sessions but also brings technical issues regarding dye delivery in live animals (Abdelfattah et al., 2019). Most FRET-opsins have negative polarity in that their fluorescence declines with increasing depolarization, which implies higher background fluorescence levels that are unfavorable for spike detection. However, creating positive polarity FRET-opsins is also feasible (Abdelfattah et al., 2020). Since neurons expressing positive and negative polarity FRET-opsins of the same color can be distinguished via the opposite directionalities of their optical spike waveforms, a suite of 4 mutually compatible GEVIs comprising red and green fluorescent variants of positive and negative polarity FRET-opsins in principle allows voltage imaging studies of up to 4 different neuron types at once using dual-color fluorescence microscopy (Kannan et al., 2021).

Notably, to date only the VSD-based GEVIs have been successfully used for two-photon voltage imaging in live animals (Akemann et al., 2013; Chamberland et al., 2017; Villette et al., 2019; Wu et al., 2020). Some rhodopsin-based GEVIs produce measurable voltage-sensitive responses *in vitro* under two-photon imaging but with much less dynamic range than with one-photon imaging (Brinks et al., 2015). Part of the challenge with rhodopsin GEVIs may concern temporal mismatches between the kinetics of the voltage-sensitive steps of the photocycle, pulse emission rates of lasers typically used for two-photon excitation, and the speed with which the cell membrane is sampled (Maclaurin et al., 2013), but further work on these issues is warranted. As with Ca^{2+} imaging, two-photon voltage imaging offers prospects for imaging deeper into tissue and superior resolution of fine neural processes such as dendrites and spines (Cornejo et al., 2021), but a notable hurdle has been the $\geq$1 kHz sampling rate needed to capture millisecond-scale voltage transients.

Recently, two studies demonstrated two-photon voltage imaging at single-spike resolution in awake mice expressing a soma-targeted GEVI (ASAP3) in neocortical neurons. In one study, high-speed raster scanning with a single beam enabled 1–3 kHz imaging rates over a 50 μm × 250 μm area (Figure 7D) (Wu et al., 2020). The other performed random-access scanning of up to 3 cells at once up to ~450 μm deep in cortex (Figure 7E), using an expanded two-photon excitation volume designed to fully cover individual cell bodies and to mitigate artifactual changes in fluorescence from brain motion (Villette et al., 2019). These approaches revealed spiking and sub-threshold dynamics in single neurons, although the latter method led to less photobleaching and penetrated more deeply into tissue. We expect continued progress in two-photon microscopy methods tailored for voltage imaging, such as by further development of high-speed two-photon microscopes, methods for selectively illuminating the cell-body membrane, and modes of illumination that are better matched to the photophysics of opsin-based GEVIs.

A bottleneck for one-photon voltage imaging remains a lack of scientific-grade cameras with full-frame acquisition rates of $\geq$1 kHz. Only a fraction of camera pixels (~5%–25%) are typically used when imaging at 0.40–1 kHz, which severely limits the number of cells that can be jointly monitored at cellular resolution (see, e.g., Figure 7C). Instrumentation for 1 kHz imaging of a $\geq$1 mm^2 FOV at cellular resolution would propel voltage-imaging studies of large neural ensembles. High-speed voltage imaging of deep brain areas with microendoscopes should also be feasible, but to maximize light collection it will be important to use microendoscopes of higher numerical apertures than those typically employed for Ca^{2+} imaging (Barretto et al., 2009).

Further improvements in GEVIs will also be important. Identifying high brightness GEVIs with reduced resting fluorescence and greater dynamic range would not only improve spike detection (d') but also allow illumination levels to be lowered while maintaining high-fidelity spike detection, thereby extending imaging sessions. Since both rhodopsins and the fluors used for

FRET-opsin and recent VSD-based GEVIs already have excellent within-class photostability, improving GEVI signaling in these ways might be a route to longer imaging sessions, as a complementary alternative to seeking further gains in photostability. In the meantime, researchers can perform long-term studies with repeated voltage-imaging sessions by selectively illuminating neurons during multiple, brief behavioral trials that constitute only a fraction of each session's total duration (Huang et al., 2018).

OPTICAL BRAIN IMAGING IN NON-HUMAN PRIMATES

Non-human primates (NHPs) are important model species in neuroscience due to their sophisticated behavioral capabilities and the greater similarity of the human nervous system to that of NHPs than rodents. Thus, studies of NHPs are central to several ongoing, national brain research initiatives including the Japan Brain-MINDS Project, the U.S. BRAIN Initiative, and the China Brain Project, and the optical methods discussed in preceding sections pertain directly to the success of these initiatives. We examine recent progress in imaging studies of the macaque and marmoset monkey brains and highlight challenges and opportunities specific to NHPs.

Early optical imaging studies of the monkey brain lacked cellular resolution and relied on intrinsic optical signatures of brain activity or synthetic voltage-sensitive dyes (Grinvald et al., 1991; Lieke et al., 1989). As the use of fluorescent proteins and optogenetic actuators has revolutionized neuroscience, application of these tools in NHPs has generally required development of customized viral expression methods, animal preparations, and optical apparatus. Initial studies in macaques used AAVs to express fluorophores, surgical installation of an artificial dura to gain optical access (Arieli et al., 2002; Chen et al., 2002), and one- or two-photon fluorescence microscopy to image neural morphologies (Stettler et al., 2006; Yamahachi et al., 2009) or Ca^{2+} dynamics (Heider et al., 2010; Seidemann et al., 2016).

While efforts are underway to develop transgenic marmosets (Okano, 2021), including those that express GECIs (Park et al., 2016), most optical studies in NHPs use AAVs to deliver an indicator or opsin. Foundational work explored different AAV serotypes and promoters to identify gene delivery approaches that allow long-term imaging of Ca^{2+} activity in primates (Seidemann et al., 2016; Watakabe et al., 2015). Notably, AAV1 encoding GCaMP via the synapsin promoter led to expression levels suitable for two-photon Ca^{2+} imaging in macaques (Li et al., 2017a; Tang et al., 2018) and marmosets (Yamada et al., 2016). The same viral delivery approach allowed imaging of glutamate release in macaques (Ju et al., 2020). Another successful method uses two AAVs to express GCaMP via the tetracycline-inducible (TET-Off) gene expression system (Sadakane et al., 2015). In this approach, GCaMP expression levels are controllable by doxycycline administration and amplified by the tetracycline-controlled transactivator (tTA), enabling large-scale Ca^{2+} imaging studies in the sensory (Garg et al., 2019; Zeng et al., 2019) and motor cortices (Bollimunta et al., 2021; Ebina et al., 2018; Kondo et al., 2018) of marmosets and macaques.

To date, there have been two main approaches to image cellular level Ca^{2+} responses in NHPs. The first involves benchtop two-photon microscopy, customized for use in primates, and installation of a glass cranial window (Li et al., 2017a; Sadakane et al., 2015). The second involves head-mounted miniature microscopes and implanted microendoscopes (Bollimunta et al., 2021; Kondo et al., 2018). In both cases, the glass implant seems to facilitate imaging at cellular resolution by stabilizing brain motion more than the artificial duras used in earlier studies (Heider et al., 2010). Due to the thickness and opacity of the primate dura, it must be removed for cortical imaging (Chen et al., 2002; Sadakane et al., 2015), which has motivated surgical protocols and implant geometries to prevent dural regrowth within the FOV (Bollimunta et al., 2021; Li et al., 2017a).

In addition to leaving the brain intact, in the NHP the cranial window can readily expose a wide area of tissue (e.g., 8 mm wide) (Li et al., 2017a). The ~1 mm spread of locally injected AAV makes it hard to express a GECI uniformly over a large cortical area, although retrograde viral labeling (Weiss et al., 2020) and viral approaches for labeling the whole NHP brain (Flytzanis et al., 2020) may ameliorate this limitation.

Two-photon imaging in head-fixed NHPs generally requires mechanical customization. First, to ensure micron-scale stability of the FOV during animal behavior, stringent mechanical constraints for stabilizing the head and body have been needed (Ebina et al., 2018; Trautmann et al., 2021; Yamada et al., 2016). Second, to provide flexible access to an arbitrary portion of the cortical surface, microscopes for primates have needed 5 mechanical degrees of freedom and large travel ranges for objective placement (Choi et al., 2018; Heider et al., 2010; Trautmann et al., 2021). To date, two-photon Ca^{2+} imaging with subcellular resolution has been achieved in head-fixed macaques and marmosets during active behavior (Ebina et al., 2018; Li et al., 2017a; Trautmann et al., 2021). Two-photon Ca^{2+} imaging has also been integrated with one- and two-photon optogenetics for studies in macaques (Ju et al., 2018).

The use of head-mounted miniature microscopes obviates the need for head fixation, allowing studies of a greater range of behaviors (Bollimunta et al., 2021; Kondo et al., 2018). This may be especially useful for studies in marmosets, which need extensive habituation to head fixation (Ebina et al., 2018; Yamada et al., 2016) and can be imaged while exploring their enclosures in three dimensions, such as during climbing (Kondo et al., 2018). Further, the small size of a miniature microscope relative to that of an NHP brain enables the use of two or more microscopes concurrently for studies of brain area interactions (Bollimunta et al., 2021). The greater weight-bearing capacity of NHPs also opens the door to larger, custom-designed miniature microscopes, such as with larger FOVs (Scott et al., 2018) or wireless data transmission (Barbera et al., 2019).

In addition to these benefits of miniature microscopes, their joint use with implanted microendoscopes may further reduce brain motion artifacts and should allow studies of deeper cortical layers or sub-cortical regions. However, imaging systems using longer microendoscopes for reaching deep areas of the NHP brain may require more extensive engineering to correct optical aberrations within an extended GRIN microendoscope probe. Insertion of micro-optical elements into fissures or sulci, as done in the mouse (Low et al., 2014), may also expand the set of routes to access the NHP brain.

Looking ahead, we see several challenges and opportunities for studies in NHPs. On the one hand, the larger size of the primate brain presents unique opportunities for studies of multiple brain areas with multi-axis microscopes (Lecoq et al., 2014) or the joint use of several miniature microscopes. On the other hand, the cortical thickness in NHPs ($\lesssim$2 mm in marmosets and $\sim$2.5–3 mm in macaques) exceeds the penetration depth of two-photon imaging, and the gyrencephalic macaque brain complicates access to many cortical areas (Watakabe et al., 2015). Thus, the additional penetration of three-photon microscopy might be especially valuable for studies of NHPs. Due to its size, the monkey brain may tolerate greater amounts of heat than the rodent brain, potentially allowing higher illumination powers. As the repertoire of genetic tools and disease models expands in NHPs, we expect that customized imaging approaches for use in NHPs will become increasingly valuable for revealing insights about brain function and dysfunction that bear directly on human health.

OUTLOOK

As described above, cutting-edge imaging studies of large-scale neural dynamics involve techniques that have sprung from multiple disciplines, including protein engineering, virology, genetics, animal surgery, and optics. Methods from behavioral neuroscience and for computational analyses of large datasets, neither of which we covered here, are often equally important. Hence, mastery of all the approaches needed to conduct a large-scale neural imaging study is already challenging for individual researchers and laboratories. As imaging techniques steadily become more sophisticated, this challenge will grow more severe. The interdisciplinary nature of the field also makes it harder to advance sets of complementary technologies in a holistic fashion.

For example, the goal of imaging deeper in tissue might best be served by synergistic efforts to engineer new infrared indicators, lasers tailored to excite these indicators, and optics and photodetectors optimized for the appropriate wavelengths and large FOVs. Optimal integration of large-scale two-photon optogenetics and parallelized imaging strategies within next-generation mesoscopes, plus the adaptation of these technologies for use in primates, will require concerted engineering that might fit within the current national initiatives for neuroscience research. Without this level of coordinated effort, optical brain imaging may not achieve its full capabilities that are feasible in principle and attainable with appropriate engineering development. To this point, advances in many of the constituent optical components needed for microscopes in neuroscience are driven by needs and markets in other fields, not the needs of neuroscientists. Nor is this optical hardware easily developed, produced, and distributed by academic neuroscientists alone. Notably, only a modest number of neuroscience labs are actively creating novel optical hardware for brain imaging, and efforts to distribute open-source instruments have to date been far less successful in leading to published biological experiments than the open-source distribution of novel indicators and opsins.

To address these dilemmas, national brain observatory facilities have been proposed as research centers to jointly advance the multiple constituent technologies needed for large-scale brain imaging, democratize access to cutting-edge instrumentation under community oversight, and standardize experimental methods and analyses to improve the quality and reproducibility of optical studies (Alivisatos et al., 2015; Koch and Reid, 2012). The integration of spatially resolved transcriptomic and proteomic methods with large-scale optical brain imaging would also likely benefit from coordinated efforts to create merged experimental pipelines. Notably, there are presently major initiatives to classify all the neuron types in the mammalian brain based on their transcriptomic signatures. As these efforts progress, an understanding of how the large number of neuron types work together in the live brain might best be gained through direct comparisons between *in vivo* and post-mortem imaging datasets that have been cross-registered to single-cell precision. Accomplishing this for the largest achievable *in vivo* imaging datasets may require the involvement of dedicated facilities that have state-of-the-art instruments for both the *in vivo* and post-mortem imaging components, as well as validated procedures for processing the tissue through all phases of experimentation and then aligning the datasets. While the neuroscience community has not yet explored in detail what observatory facilities might encompass and how they might operate, the importance of optical brain imaging to an expanding set of basic and disease-related neuroscience sub-fields and the growing challenges of performing and validating each facet of an imaging study suggest that the creation of brain observatory facilities might ultimately be inevitable. The speed with which such facilities may arise is far less clear, but organized consortia and team projects are already becoming more common in neuroscience.

Certainly, optical studies and technology development performed in individual labs will remain crucial to the vitality of the field. Facilitating such research, mechanisms already exist to provide researchers access to transgenic mice, viruses, optical indicators, and opsins. Missing, however, is a mechanism to provide neuroscientists with access to state-of-the-art optical instrumentation. In other scientific fields, experimental time on large-scale, community-managed instrumentation is allocated through a peer review process, and brain observatories could also follow this practice. As innovations in brain imaging bring us closer to observing a million neurons at once (Demas et al., 2021), facilities that provide widespread access to such next-generation technologies would likely become popular resources. Much as synchrotron and large telescope facilities ushered in new eras of physics research, brain observatories would likely catalyze previously unimaginable experiments and spark a new age of neuroscience.

ACKNOWLEDGMENTS

Our work on brain imaging has been supported by funding from the NIH BRAIN Initiative, the NSF NeuroNex Program, DARPA, and HHMI. We thank H. Bito, R. Chrapkiewicz, S. Haziza, O. Hernandez, L. Huang, M. Inoue, M.Z. Lin, L. Luo, S. Sternson, M.J. Wagner, and Y. Zhang for helpful conversations.

DECLARATION OF INTERESTS

M.J.S. is a scientific co-founder of and consults for Inscopix Inc., which manufactures the integrated miniature microscope. The authors are inventors on multiple patents and patent applications pertaining to topics covered in this primer.

REFERENCES

Abdelfattah, A.S., Kawashima, T., Singh, A., Novak, O., Liu, H., Shuai, Y., Huang, Y.-C., Campagnola, L., Seeman, S.C., Yu, J., et al. (2019). Bright and photostable chemigenetic indicators for extended in vivo voltage imaging. Science *365*, 699–704.

Abdelfattah, A.S., Valenti, R., Zheng, J., Wong, A., Podgorski, K., Koyama, M., Kim, D.S., and Schreiter, E.R.; GENIE Project Team (2020). A general approach to engineer positive-going eFRET voltage indicators. Nat. Commun. *11*, 3444.

Adam, Y., Kim, J.J., Lou, S., Zhao, Y., Xie, M.E., Brinks, D., Wu, H., Mostajo-Radji, M.A., Kheifets, S., Parot, V., et al. (2019). Voltage imaging and optogenetics reveal behaviour-dependent changes in hippocampal dynamics. Nature *569*, 413–417.

Akemann, W., Mutoh, H., Perron, A., Rossier, J., and Knöpfel, T. (2010). Imaging brain electric signals with genetically targeted voltage-sensitive fluorescent proteins. Nat. Methods *7*, 643–649.

Akemann, W., Sasaki, M., Mutoh, H., Imamura, T., Honkura, N., and Knöpfel, T. (2013). Two-photon voltage imaging using a genetically encoded voltage indicator. Sci. Rep. *3*, 2231.

Akerboom, J., Chen, T.-W., Wardill, T.J., Tian, L., Marvin, J.S., Mutlu, S., Calderón, N.C., Esposti, F., Borghuis, B.G., Sun, X.R., et al. (2012). Optimization of a GCaMP calcium indicator for neural activity imaging. J. Neurosci. *32*, 13819–13840.

Al-Juboori, S.I., Dondzillo, A., Stubblefield, E.A., Felsen, G., Lei, T.C., and Klug, A. (2013). Light scattering properties vary across different regions of the adult mouse brain. PLoS ONE *8*, e67626.

Alivisatos, A.P., Chun, M., Church, G.M., Greenspan, R.J., Roukes, M.L., and Yuste, R. (2015). A National Network of Neurotechnology Centers for the BRAIN Initiative. Neuron *88*, 445–448.

Allen, W.E., Kauvar, I.V., Chen, M.Z., Richman, E.B., Yang, S.J., Chan, K., Gradinaru, V., Deverman, B.E., Luo, L., and Deisseroth, K. (2017). Global Representations of Goal-Directed Behavior in Distinct Cell Types of Mouse Neocortex. Neuron *94*, 891–907.e6.

Amir, W., Carriles, R., Hoover, E.E., Planchon, T.A., Durfee, C.G., and Squier, J.A. (2007). Simultaneous imaging of multiple focal planes using a two-photon scanning microscope. Opt. Lett. *32*, 1731–1733.

Andermann, M.L., Gilfoy, N.B., Goldey, G.J., Sachdev, R.N.S., Wölfel, M., McCormick, D.A., Reid, R.C., and Levene, M.J. (2013). Chronic cellular imaging of entire cortical columns in awake mice using microprisms. Neuron *80*, 900–913.

Andrasfalvy, B.K., Zemelman, B.V., Tang, J., and Vaziri, A. (2010). Two-photon single-cell optogenetic control of neuronal activity by sculpted light. Proc. Natl. Acad. Sci. USA *107*, 11981–11986.

Arieli, A., Grinvald, A., and Slovin, H. (2002). Dural substitute for long-term imaging of cortical activity in behaving monkeys and its clinical implications. J. Neurosci. Methods *114*, 119–133.

Baker, C.A., Elyada, Y.M., Parra, A., and Bolton, M.M. (2016). Cellular resolution circuit mapping with temporal-focused excitation of soma-targeted channelrhodopsin. eLife *5*, e14193.

Barbera, G., Liang, B., Zhang, L., Li, Y., and Lin, D.-T. (2019). A wireless miniScope for deep brain imaging in freely moving mice. J. Neurosci. Methods *323*, 56–60.

Barnett, L., Platisa, J., Popovic, M., Pieribone, V.A., and Hughes, T. (2012). A fluorescent, genetically-encoded voltage probe capable of resolving action potentials. PLoS ONE *7*, e43454.

Barretto, R.P.J., Messerschmidt, B., and Schnitzer, M.J. (2009). In vivo fluorescence imaging with high-resolution microlenses. Nat. Methods *6*, 511–512.

Barretto, R.P.J., Ko, T.H., Jung, J.C., Wang, T.J., Capps, G., Waters, A.C., Ziv, Y., Attardo, A., Recht, L., and Schnitzer, M.J. (2011). Time-lapse imaging of disease progression in deep brain areas using fluorescence microendoscopy. Nat. Med. *17*, 223–228.

Barson, D., Hamodi, A.S., Shen, X., Lur, G., Constable, R.T., Cardin, J.A., Crair, M.C., and Higley, M.J. (2020). Simultaneous mesoscopic and two-photon imaging of neuronal activity in cortical circuits. Nat. Methods *17*, 107–113.

Beaulieu, D.R., Davison, I.G., Kılıç, K., Bifano, T.G., and Mertz, J. (2020). Simultaneous multiplane imaging with reverberation two-photon microscopy. Nat. Methods *17*, 283–286.

Bedbrook, C.N., Deverman, B.E., and Gradinaru, V. (2018). Viral Strategies for Targeting the Central and Peripheral Nervous Systems. Annu. Rev. Neurosci. *41*, 323–348.

Bewersdorf, J., Pick, R., and Hell, S.W. (1998). Multifocal multiphoton microscopy. Opt. Lett. *23*, 655–657.

Blankvoort, S., Witter, M.P., Noonan, J., Cotney, J., and Kentros, C. (2018). Marked Diversity of Unique Cortical Enhancers Enables Neuron-Specific Tools by Enhancer-Driven Gene Expression. Curr. Biol. *28*, 2103–2114.e5.

Bollimunta, A., Santacruz, S.R., Eaton, R.W., Xu, P.S., Morrison, J.H., Moxon, K.A., Carmena, J.M., and Nassi, J.J. (2021). Head-mounted microendoscopic calcium imaging in dorsal premotor cortex of behaving rhesus macaque. Cell Rep. *35*, 109239.

Botcherby, E.J., Smith, C.W., Kohl, M.M., Débarre, D., Booth, M.J., Juškaitis, R., Paulsen, O., and Wilson, T. (2012). Aberration-free three-dimensional multiphoton imaging of neuronal activity at kHz rates. Proc. Natl. Acad. Sci. USA *109*, 2919–2924.

Boyden, E.S., Zhang, F., Bamberg, E., Nagel, G., and Deisseroth, K. (2005). Millisecond-timescale, genetically targeted optical control of neural activity. Nat. Neurosci. *8*, 1263–1268.

Brinks, D., Klein, A.J., and Cohen, A.E. (2015). Two-Photon Lifetime Imaging of Voltage Indicating Proteins as a Probe of Absolute Membrane Voltage. Biophys. J. *109*, 914–921.

Brondi, M., Moroni, M., Vecchia, D., Molano-Mazón, M., Panzeri, S., and Fellin, T. (2020). High-Accuracy Detection of Neuronal Ensemble Activity in Two-Photon Functional Microscopy Using Smart Line Scanning. Cell Rep. *30*, 2567–2580.e6.

Broxton, M., Grosenick, L., Yang, S., Cohen, N., Andalman, A., Deisseroth, K., and Levoy, M. (2013). Wave optics theory and 3-D deconvolution for the light field microscope. Opt. Express *21*, 25418–25439.

Cai, D.J., Aharoni, D., Shuman, T., Shobe, J., Biane, J., Song, W., Wei, B., Veshkini, M., La-Vu, M., Lou, J., et al. (2016). A shared neural ensemble links distinct contextual memories encoded close in time. Nature *534*, 115–118.

Chalfie, M., Tu, Y., Euskirchen, G., Ward, W.W., and Prasher, D.C. (1994). Green fluorescent protein as a marker for gene expression. Science *263*, 802–805.

Challis, R.C., Ravindra Kumar, S., Chan, K.Y., Challis, C., Beadle, K., Jang, M.J., Kim, H.M., Rajendran, P.S., Tompkins, J.D., Shivkumar, K., et al. (2019). Systemic AAV vectors for widespread and targeted gene delivery in rodents. Nat. Protoc. *14*, 379–414.

Chamberland, S., Yang, H.H., Pan, M.M., Evans, S.W., Guan, S., Chavarha, M., Yang, Y., Salesse, C., Wu, H., Wu, J.C., et al. (2017). Fast two-photon imaging of subcellular voltage dynamics in neuronal tissue with genetically encoded indicators. eLife *6*, e25690.

Chan, K.Y., Jang, M.J., Yoo, B.B., Greenbaum, A., Ravi, N., Wu, W.-L., Sánchez-Guardado, L., Lois, C., Mazmanian, S.K., Deverman, B.E., and Gradinaru, V. (2017). Engineered AAVs for efficient noninvasive gene delivery to the central and peripheral nervous systems. Nat. Neurosci. *20*, 1172–1179.

Chatterjee, S., Sullivan, H.A., MacLennan, B.J., Xu, R., Hou, Y., Lavin, T.K., Lea, N.E., Michalski, J.E., Babcock, K.R., Dietrich, S., et al. (2018). Nontoxic, double-deletion-mutant rabies viral vectors for retrograde targeting of projection neurons. Nat. Neurosci. *21*, 638–646.

Chen, L.M., Heider, B., Williams, G.V., Healy, F.L., Ramsden, B.M., and Roe, A.W. (2002). A chamber and artificial dura method for long-term optical imaging in the monkey. J. Neurosci. Methods *113*, 41–49.

Chen, T.-W., Wardill, T.J., Sun, Y., Pulver, S.R., Renninger, S.L., Baohan, A., Schreiter, E.R., Kerr, R.A., Orger, M.B., Jayaraman, V., et al. (2013). Ultrasensitive fluorescent proteins for imaging neuronal activity. Nature *499*, 295–300.

Chen, Y., Jang, H., Spratt, P.W.E., Kosar, S., Taylor, D.E., Essner, R.A., Bai, L., Leib, D.E., Kuo, T.-W., Lin, Y.-C., et al. (2020). Soma-Targeted Imaging of Neural Circuits by Ribosome Tethering. Neuron *107*, 454–469.e6.

Cheng, A., Gonçalves, J.T., Golshani, P., Arisaka, K., and Portera-Cailliau, C. (2011). Simultaneous two-photon calcium imaging at different depths with spatiotemporal multiplexing. Nat. Methods *8*, 139–142.

Choi, J., Goncharov, V., Kleinbart, J., Orsborn, A., and Pesaran, B. (2018). Monkey-MIMMS: Towards Automated Cellular Resolution Large- Scale Two-Photon Microscopy In The Awake Macaque Monkey. Annu Int Conf IEEE Eng Med Biol Soc *2018*, 3013–3016.

Chuong, A.S., Miri, M.L., Busskamp, V., Matthews, G.A.C., Acker, L.C., Sørensen, A.T., Young, A., Klapoetke, N.C., Henninger, M.A., Kodandaramaiah, S.B., et al. (2014). Noninvasive optical inhibition with a red-shifted microbial rhodopsin. Nat. Neurosci. *17*, 1123–1129.

Close, J.L., Long, B.R., and Zeng, H. (2021). Spatially resolved transcriptomics in neuroscience. Nat. Methods *18*, 23–25.

Condylis, C., Lowet, E., Ni, J., Bistrong, K., Ouellette, T., Josephs, N., and Chen, J.L. (2020). Context-Dependent Sensory Processing across Primary and Secondary Somatosensory Cortex. Neuron *106*, 515–525.e5.

Cong, L., Wang, Z., Chai, Y., Hang, W., Shang, C., Yang, W., Bai, L., Du, J., Wang, K., and Wen, Q. (2017). Rapid whole brain imaging of neural activity in freely behaving larval zebrafish (*Danio rerio*). eLife *6*, e28158.

Corder, G., Ahanonu, B., Grewe, B.F., Wang, D., Schnitzer, M.J., and Scherrer, G. (2019). An amygdalar neural ensemble that encodes the unpleasantness of pain. Science *363*, 276–281.

Cornejo, V.H., Ofer, N., and Yuste, R. (2021). Voltage compartmentalization in dendritic spines in vivo. Science. Published online November 11, 2021. https://doi.org/10.1126/science.abg0501.

da Silva, J.A., Tecuapetla, F., Paixão, V., and Costa, R.M. (2018). Dopamine neuron activity before action initiation gates and invigorates future movements. Nature *554*, 244–248.

Daigle, T.L., Madisen, L., Hage, T.A., Valley, M.T., Knoblich, U., Larsen, R.S., Takeno, M.M., Huang, L., Gu, H., Larsen, R., et al. (2018). A Suite of Transgenic Driver and Reporter Mouse Lines with Enhanced Brain-Cell-Type Targeting and Functionality. Cell *174*, 465–480.e22.

Dana, H., Mohar, B., Sun, Y., Narayan, S., Gordus, A., Hasseman, J.P., Tsegaye, G., Holt, G.T., Hu, A., Walpita, D., et al. (2016). Sensitive red protein calcium indicators for imaging neural activity. eLife *5*, e12727.

Dana, H., Sun, Y., Mohar, B., Hulse, B.K., Kerlin, A.M., Hasseman, J.P., Tsegaye, G., Tsang, A., Wong, A., Patel, R., et al. (2019). High-performance calcium sensors for imaging activity in neuronal populations and microcompartments. Nat. Methods *16*, 649–657.

de Groot, A., van den Boom, B.J., van Genderen, R.M., Coppens, J., van Veldhuijzen, J., Bos, J., Hoedemaker, H., Negrello, M., Willuhn, I., De Zeeuw, C.I., and Hoogland, T.M. (2020). NINscope, a versatile miniscope for multi-region circuit investigations. eLife *9*, e49987.

Demas, J., Manley, J., Tejera, F., Barber, K., Kim, H., Traub, F.M., Chen, B., and Vaziri, A. (2021). High-speed, cortex-wide volumetric recording of neuroactivity at cellular resolution using light beads microscopy. Nat. Methods *18*, 1103–1111.

Denk, W., Strickler, J.H., and Webb, W.W. (1990). Two-photon laser scanning fluorescence microscopy. Science *248*, 73–76.

Dimitrov, D., He, Y., Mutoh, H., Baker, B.J., Cohen, L., Akemann, W., and Knöpfel, T. (2007). Engineering and characterization of an enhanced fluorescent protein voltage sensor. PLoS ONE *2*, e440.

Dombeck, D.A., Harvey, C.D., Tian, L., Looger, L.L., and Tank, D.W. (2010). Functional imaging of hippocampal place cells at cellular resolution during virtual navigation. Nat. Neurosci. *13*, 1433–1440.

Dong, A., He, K., Dudok, B., Farrell, J.S., Guan, W., Liput, D.J., Puhl, H.L., Cai, R., Wang, H., Duan, J., et al. (2021). A fluorescent sensor for spatiotemporally resolved imaging of endocannabinoid dynamics in vivo. Nat Biotechnol. Published online November 11, 2021. https://doi.org/10.1038/s41587-021-01074-4.

Donnert, G., Eggeling, C., and Hell, S.W. (2007). Major signal increase in fluorescence microscopy through dark-state relaxation. Nat. Methods *4*, 81–86.

Drew, P.J., Shih, A.Y., Driscoll, J.D., Knutsen, P.M., Blinder, P., Davalos, D., Akassoglou, K., Tsai, P.S., and Kleinfeld, D. (2010). Chronic optical access through a polished and reinforced thinned skull. Nat. Methods *7*, 981–984.

Duemani Reddy, G., Kelleher, K., Fink, R., and Saggau, P. (2008). Three-dimensional random access multiphoton microscopy for functional imaging of neuronal activity. Nat. Neurosci. *11*, 713–720.

Ebina, T., Masamizu, Y., Tanaka, Y.R., Watakabe, A., Hirakawa, R., Hirayama, Y., Hira, R., Terada, S.-I., Koketsu, D., Hikosaka, K., et al. (2018). Two-photon imaging of neuronal activity in motor cortex of marmosets during upper-limb movement tasks. Nat. Commun. *9*, 1879.

Emiliani, V., Cohen, A.E., Deisseroth, K., and Häusser, M. (2015). All-Optical Interrogation of Neural Circuits. J. Neurosci. *35*, 13917–13926.

Fan, J., Suo, J., Wu, J., Xie, H., Shen, Y., Chen, F., Wang, G., Cao, L., Jin, G., He, Q., et al. (2019). Video-rate imaging of biological dynamics at centimetre scale and micrometre resolution. Nat. Photonics *13*, 809–816.

Fan, L.Z., Kheifets, S., Böhm, U.L., Wu, H., Piatkevich, K.D., Xie, M.E., Parot, V., Ha, Y., Evans, K.E., Boyden, E.S., et al. (2020). All-Optical Electrophysiology Reveals the Role of Lateral Inhibition in Sensory Processing in Cortical Layer 1. Cell *180*, 521–535.e18.

Feldbauer, K., Zimmermann, D., Pintschovius, V., Spitz, J., Bamann, C., and Bamberg, E. (2009). Channelrhodopsin-2 is a leaky proton pump. Proc. Natl. Acad. Sci. USA *106*, 12317–12322.

Fenno, L.E., Ramakrishnan, C., Kim, Y.S., Evans, K.E., Lo, M., Vesuna, S., Inoue, M., Cheung, K.Y.M., Yuen, E., Pichamoorthy, N., et al. (2020). Comprehensive Dual- and Triple-Feature Intersectional Single-Vector Delivery of Diverse Functional Payloads to Cells of Behaving Mammals. Neuron *107*, 836–853.e11.

Flusberg, B.A., Nimmerjahn, A., Cocker, E.D., Mukamel, E.A., Barretto, R.P.J., Ko, T.H., Burns, L.D., Jung, J.C., and Schnitzer, M.J. (2008). High-speed, miniaturized fluorescence microscopy in freely moving mice. Nat. Methods *5*, 935–938.

Flytzanis, N.C., Bedbrook, C.N., Chiu, H., Engqvist, M.K.M., Xiao, C., Chan, K.Y., Sternberg, P.W., Arnold, F.H., and Gradinaru, V. (2014). Archaerhodopsin variants with enhanced voltage-sensitive fluorescence in mammalian and Caenorhabditis elegans neurons. Nat. Commun. *5*, 4894.

Flytzanis, N.C., Goeden, N., Goertsen, D., Cummins, A., Pickel, J., and Gradinaru, V. (2020). Broad gene expression throughout the mouse and marmoset brain after intravenous delivery of engineered AAV capsids. bioRxiv. https://doi.org/10.1101/2020.06.16.152975.

Forli, A., Vecchia, D., Binini, N., Succol, F., Bovetti, S., Moretti, C., Nespoli, F., Mahn, M., Baker, C.A., Bolton, M.M., et al. (2018). Two-Photon Bidirectional Control and Imaging of Neuronal Excitability with High Spatial Resolution In Vivo. Cell Rep. *22*, 3087–3098.

Gao, P., and Ganguli, S. (2015). On simplicity and complexity in the brave new world of large-scale neuroscience. Curr. Opin. Neurobiol. *32*, 148–155.

Garg, A.K., Li, P., Rashid, M.S., and Callaway, E.M. (2019). Color and orientation are jointly coded and spatially organized in primate primary visual cortex. Science *364*, 1275–1279.

Gerfen, C.R., Paletzki, R., and Heintz, N. (2013). GENSAT BAC cre-recombinase driver lines to study the functional organization of cerebral cortical and basal ganglia circuits. Neuron *80*, 1368–1383.

Ghosh, K.K., Burns, L.D., Cocker, E.D., Nimmerjahn, A., Ziv, Y., Gamal, A.E., and Schnitzer, M.J. (2011). Miniaturized integration of a fluorescence microscope. Nat. Methods *8*, 871–878.

Gong, Y., Li, J.Z., and Schnitzer, M.J. (2013). Enhanced Archaerhodopsin Fluorescent Protein Voltage Indicators. PLoS ONE *8*, e66959.

Gong, Y., Wagner, M.J., Zhong Li, J., and Schnitzer, M.J. (2014). Imaging neural spiking in brain tissue using FRET-opsin protein voltage sensors. Nat. Commun. *5*, 3674.

Gong, Y., Huang, C., Li, J.Z., Grewe, B.F., Zhang, Y., Eismann, S., and Schnitzer, M.J. (2015). High-speed recording of neural spikes in awake mice and flies with a fluorescent voltage sensor. Science *350*, 1361–1366.

Gonzalez, W.G., Zhang, H., Harutyunyan, A., and Lois, C. (2019). Persistence of neuronal representations through time and damage in the hippocampus. Science *365*, 821–825.

Graybuck, L.T., Daigle, T.L., Sedeño-Cortés, A.E., Walker, M., Kalmbach, B., Lenz, G.H., Nguyen, T.N., Garren, E., Kim, T.K., Siverts, L.A., et al. (2019). Enhancer viruses and a transgenic platform for combinatorial cell subclass-specific labeling. bioRxiv. https://doi.org/10.1101/525014.

Grewe, B.F., Langer, D., Kasper, H., Kampa, B.M., and Helmchen, F. (2010). High-speed in vivo calcium imaging reveals neuronal network activity with near-millisecond precision. Nat. Methods *7*, 399–405.

Grewe, B.F., Voigt, F.F., van 't Hoff, M., and Helmchen, F. (2011). Fast two-layer two-photon imaging of neuronal cell populations using an electrically tunable lens. Biomed. Opt. Express *2*, 2035–2046.

Grewe, B.F., Gründemann, J., Kitch, L.J., Lecoq, J.A., Parker, J.G., Marshall, J.D., Larkin, M.C., Jercog, P.E., Grenier, F., Li, J.Z., et al. (2017). Neural ensemble dynamics underlying a long-term associative memory. Nature *543*, 670–675.

Grienberger, C., and Konnerth, A. (2012). Imaging calcium in neurons. Neuron *73*, 862–885.

Griffiths, V.A., Valera, A.M., Lau, J.Y., Roš, H., Younts, T.J., Marin, B., Baragli, C., Coyle, D., Evans, G.J., Konstantinou, G., et al. (2020). Real-time 3D movement correction for two-photon imaging in behaving animals. Nat. Methods *17*, 741–748.

Grinvald, A., Frostig, R.D., Siegel, R.M., and Bartfeld, E. (1991). High-resolution optical imaging of functional brain architecture in the awake monkey. Proc. Natl. Acad. Sci. USA *88*, 11559–11563.

Gründemann, J., Bitterman, Y., Lu, T., Krabbe, S., Grewe, B.F., Schnitzer, M.J., and Lüthi, A. (2019). Amygdala ensembles encode behavioral states. Science *364*, eaav8736.

Haery, L., Deverman, B.E., Matho, K.S., Cetin, A., Woodard, K., Cepko, C., Guerin, K.I., Rego, M.A., Ersing, I., Bachle, S.M., et al. (2019). Adeno-Associated Virus Technologies and Methods for Targeted Neuronal Manipulation. Front. Neuroanat. *13*, 93.

Hamel, E.J.O., Grewe, B.F., Parker, J.G., and Schnitzer, M.J. (2015). Cellular level brain imaging in behaving mammals: an engineering approach. Neuron *86*, 140–159.

Harvey, C.D., Collman, F., Dombeck, D.A., and Tank, D.W. (2009). Intracellular dynamics of hippocampal place cells during virtual navigation. Nature *461*, 941–946.

Heider, B., Nathanson, J.L., Isacoff, E.Y., Callaway, E.M., and Siegel, R.M. (2010). Two-photon imaging of calcium in virally transfected striate cortical neurons of behaving monkey. PLoS ONE *5*, e13829.

Helmchen, F., and Denk, W. (2005). Deep tissue two-photon microscopy. Nat. Methods *2*, 932–940.

Helmchen, F., Imoto, K., and Sakmann, B. (1996). Ca2+ buffering and action potential-evoked Ca2+ signaling in dendrites of pyramidal neurons. Biophys. J. *70*, 1069–1081.

Helmchen, F., Fee, M.S., Tank, D.W., and Denk, W. (2001). A miniature head-mounted two-photon microscope. high-resolution brain imaging in freely moving animals. Neuron *31*, 903–912.

Hernandez, O., Papagiakoumou, E., Tanese, D., Fidelin, K., Wyart, C., and Emiliani, V. (2016). Three-dimensional spatiotemporal focusing of holographic patterns. Nat. Commun. *7*, 11928.

Hochbaum, D.R., Zhao, Y., Farhi, S.L., Klapoetke, N., Werley, C.A., Kapoor, V., Zou, P., Kralj, J.M., Maclaurin, D., Smedemark-Margulies, N., et al. (2014). All-optical electrophysiology in mammalian neurons using engineered microbial rhodopsins. Nat. Methods *11*, 825–833.

Holtmaat, A., Bonhoeffer, T., Chow, D.K., Chuckowree, J., De Paola, V., Hofer, S.B., Hübener, M., Keck, T., Knott, G., Lee, W.-C.A., et al. (2009). Long-term, high-resolution imaging in the mouse neocortex through a chronic cranial window. Nat. Protoc. *4*, 1128–1144.

Hopt, A., and Neher, E. (2001). Highly nonlinear photodamage in two-photon fluorescence microscopy. Biophys. J. *80*, 2029–2036.

Hornung, R., Pritchard, A., Kinchington, P.R., and Kramer, P.R. (2020). Reduced activity of GAD67 expressing cells in the reticular thalamus enhance thalamic excitatory activity and varicella zoster virus associated pain. Neurosci. Lett. *736*, 135287.

Horton, N.G., Wang, K., Kobat, D., Clark, C.G., Wise, F.W., Schaffer, C.B., and Xu, C. (2013). *In vivo* three-photon microscopy of subcortical structures within an intact mouse brain. Nat. Photonics *7*, 205–209.

Huang, C., Maxey, J.R., Sinha, S., Savall, J., Gong, Y., and Schnitzer, M.J. (2018). Long-term optical brain imaging in live adult fruit flies. Nat. Commun. *9*, 872.

Huang, L., Knoblich, U., Ledochowitsch, P., Lecoq, J., Reid, R.C., de Vries, S.E.J., Buice, M.A., Murphy, G.J., Waters, J., Koch, C., et al. (2020). Relationship between spiking activity and simultaneously recorded fluorescence signals in transgenic mice expressing GCaMP6. bioRxiv. https://doi.org/10.1101/788802.

Inan, H., Schmuckermair, C., Tasci, T., Ahanonu, B.O., Hernandez, O., Lecoq, J., Dinç, F., Wagner, M.J., Erdogdu, M.A., and Schnitzer, M.J. (2021). Fast and statistically robust cell extraction from large-scale neural calcium imaging datasets. bioRxiv. https://doi.org/10.1101/2021.03.24.436279.

Inoue, M., Takeuchi, A., Manita, S., Horigane, S.-I., Sakamoto, M., Kawakami, R., Yamaguchi, K., Otomo, K., Yokoyama, H., Kim, R., et al. (2019). Rational Engineering of XCaMPs, a Multicolor GECI Suite for In Vivo Imaging of Complex Brain Circuit Dynamics. Cell *177*, 1346–1360.e24.

Jackman, S.L., Chen, C.H., Chettih, S.N., Neufeld, S.Q., Drew, I.R., Agba, C.K., Flaquer, I., Stefano, A.N., Kennedy, T.J., Belinsky, J.E., et al. (2018). Silk Fibroin Films Facilitate Single-Step Targeted Expression of Optogenetic Proteins. Cell Rep. *22*, 3351–3361.

Jarvie, B.C., Chen, J.Y., King, H.O., and Palmiter, R.D. (2021). Satb2 neurons in the parabrachial nucleus mediate taste perception. Nat. Commun. *12*, 224.

Jazayeri, M., and Ostojic, S. (2021). Interpreting neural computations by examining intrinsic and embedding dimensionality of neural activity. Curr. Opin. Neurobiol. *70*, 113–120.

Jennings, J.H., Kim, C.K., Marshel, J.H., Raffiee, M., Ye, L., Quirin, S., Pak, S., Ramakrishnan, C., and Deisseroth, K. (2019). Interacting neural ensembles in orbitofrontal cortex for social and feeding behaviour. Nature *565*, 645–649.

Jercog, P., Rogerson, T., and Schnitzer, M.J. (2016). Large-Scale Fluorescence Calcium-Imaging Methods for Studies of Long-Term Memory in Behaving Mammals. Cold Spring Harb. Perspect. Biol. *8*, a021824.

Ji, N. (2017). Adaptive optical fluorescence microscopy. Nat. Methods *14*, 374–380.

Ji, N., Sato, T.R., and Betzig, E. (2012). Characterization and adaptive optical correction of aberrations during in vivo imaging in the mouse cortex. Proc. Natl. Acad. Sci. USA *109*, 22–27.

Jin, L., Han, Z., Platisa, J., Wooltorton, J.R.A., Cohen, L.B., and Pieribone, V.A. (2012). Single action potentials and subthreshold electrical events imaged in neurons with a fluorescent protein voltage probe. Neuron *75*, 779–785.

Ju, N., Jiang, R., Macknik, S.L., Martinez-Conde, S., and Tang, S. (2018). Long-term all-optical interrogation of cortical neurons in awake-behaving nonhuman primates. PLoS Biol. *16*, e2005839.

Ju, N., Li, Y., Liu, F., Jiang, H., Macknik, S.L., Martinez-Conde, S., and Tang, S. (2020). Spatiotemporal functional organization of excitatory synaptic inputs onto macaque V1 neurons. Nat. Commun. *11*, 697.

Jung, J.C., and Schnitzer, M.J. (2003). Multiphoton endoscopy. Opt. Lett. *28*, 902–904.

Jung, J.C., Mehta, A.D., Aksay, E., Stepnoski, R., and Schnitzer, M.J. (2004). In vivo mammalian brain imaging using one- and two-photon fluorescence microendoscopy. J. Neurophysiol. *92*, 3121–3133.

Kalmbach, A.S., and Waters, J. (2012). Brain surface temperature under a craniotomy. J. Neurophysiol. *108*, 3138–3146.

Kannan, M., Vasan, G., Huang, C., Haziza, S., Li, J.Z., Inan, H., Schnitzer, M.J., and Pieribone, V.A. (2018). Fast, in vivo voltage imaging using a red fluorescent indicator. Nat. Methods *15*, 1108–1116.

Kannan, M., Vasan, G., Haziza, S., Huang, C., Chrapkiewicz, R., Luo, J., Cardin, J.A., Schnitzer, M.J., and Pieribone, V.A. (2021). Dual polarity voltage imaging reveals subthreshold dynamics and concurrent spiking patterns of multiple neuron-types. bioRxiv. https://doi.org/10.1101/2021.10.13.463730.

Kazemipour, A., Novak, O., Flickinger, D., Marvin, J.S., Abdelfattah, A.S., King, J., Borden, P.M., Kim, J.J., Al-Abdullatif, S.H., Deal, P.E., et al. (2019). Kilohertz frame-rate two-photon tomography. Nat. Methods *16*, 778–786.

Khan, A.G., Poort, J., Chadwick, A., Blot, A., Sahani, M., Mrsic-Flogel, T.D., and Hofer, S.B. (2018). Distinct learning-induced changes in stimulus selectivity and interactions of GABAergic interneuron classes in visual cortex. Nat. Neurosci. *21*, 851–859.

Kim, K.H., Buehler, C., Bahlmann, K., Ragan, T., Lee, W.-C.A., Nedivi, E., Heffer, E.L., Fantini, S., and So, P.T.C. (2007). Multifocal multiphoton microscopy based on multianode photomultiplier tubes. Opt. Express *15*, 11658–11678.

Kim, T.H., Zhang, Y., Lecoq, J., Jung, J.C., Li, J., Zeng, H., Niell, C.M., and Schnitzer, M.J. (2016). Long-Term Optical Access to an Estimated One Million Neurons in the Live Mouse Cortex. Cell Rep. *17*, 3385–3394.

Klapoetke, N.C., Murata, Y., Kim, S.S., Pulver, S.R., Birdsey-Benson, A., Cho, Y.K., Morimoto, T.K., Chuong, A.S., Carpenter, E.J., Tian, Z., et al. (2014). Independent optical excitation of distinct neural populations. Nat. Methods *11*, 338–346.

Klaus, A., Martins, G.J., Paixao, V.B., Zhou, P., Paninski, L., and Costa, R.M. (2017). The Spatiotemporal Organization of the Striatum Encodes Action Space. Neuron *96*, 949.

Klioutchnikov, A., Wallace, D.J., Frosz, M.H., Zeltner, R., Sawinski, J., Pawlak, V., Voit, K.-M., Russell, P.S.J., and Kerr, J.N.D. (2020). Three-photon head-mounted microscope for imaging deep cortical layers in freely moving rats. Nat. Methods *17*, 509–513.

Kobat, D., Durst, M.E., Nishimura, N., Wong, A.W., Schaffer, C.B., and Xu, C. (2009). Deep tissue multiphoton microscopy using longer wavelength excitation. Opt. Express *17*, 13354–13364.

Koch, C., and Reid, R.C. (2012). Neuroscience: Observatories of the mind. Nature *483*, 397–398.

Kondo, M., Kobayashi, K., Ohkura, M., Nakai, J., and Matsuzaki, M. (2017). Two-photon calcium imaging of the medial prefrontal cortex and hippocampus without cortical invasion. eLife *6*, e26839.

Kondo, T., Saito, R., Otaka, M., Yoshino-Saito, K., Yamanaka, A., Yamamori, T., Watakabe, A., Mizukami, H., Schnitzer, M.J., Tanaka, K.F., et al. (2018). Calcium Transient Dynamics of Neural Ensembles in the Primary Motor Cortex of Naturally Behaving Monkeys. Cell Rep. *24*, 2191–2195.e4.

Kong, L., Tang, J., Little, J.P., Yu, Y., Lämmermann, T., Lin, C.P., Germain, R.N., and Cui, M. (2015). Continuous volumetric imaging via an optical phase-locked ultrasound lens. Nat. Methods *12*, 759–762.

Kralj, J.M., Douglass, A.D., Hochbaum, D.R., Maclaurin, D., and Cohen, A.E. (2011). Optical recording of action potentials in mammalian neurons using a microbial rhodopsin. Nat. Methods *9*, 90–95.

Lanyi, J.K. (2004). Bacteriorhodopsin. Annu. Rev. Physiol. *66*, 665–688.

Lecca, S., Namboodiri, V.M.K., Restivo, L., Gervasi, N., Pillolla, G., Stuber, G.D., and Mameli, M. (2020). Heterogeneous Habenular Neuronal Ensembles during Selection of Defensive Behaviors. Cell Rep. *31*, 107752.

Lecoq, J., and Schnitzer, M.J. (2011). An infrared fluorescent protein for deeper imaging. Nat. Biotechnol. *29*, 715–716.

Lecoq, J., Savall, J., Vučinić, D., Grewe, B.F., Kim, H., Li, J.Z., Kitch, L.J., and Schnitzer, M.J. (2014). Visualizing mammalian brain area interactions by dual-axis two-photon calcium imaging. Nat. Neurosci. *17*, 1825–1829.

Lee, D., Kume, M., and Holy, T.E. (2019). Sensory coding mechanisms revealed by optical tagging of physiologically defined neuronal types. Science *366*, 1384–1389.

Levene, M.J., Dombeck, D.A., Kasischke, K.A., Molloy, R.P., and Webb, W.W. (2004). In vivo multiphoton microscopy of deep brain tissue. J. Neurophysiol. *91*, 1908–1912.

Levoy, M., Ng, R., Adams, A., Footer, M., and Horowitz, M. (2006). Light field microscopy. ACM Transactions on Graphics *25*, 924–934.

Li, M., Liu, F., Jiang, H., Lee, T.S., and Tang, S. (2017a). Long-Term Two-Photon Imaging in Awake Macaque Monkey. Neuron *93*, 1049–1057.e3.

Li, Y., Mathis, A., Grewe, B.F., Osterhout, J.A., Ahanonu, B., Schnitzer, M.J., Murthy, V.N., and Dulac, C. (2017b). Neuronal Representation of Social Information in the Medial Amygdala of Awake Behaving Mice. Cell *171*, 1176–1190.e17.

Li, B., Wu, C., Wang, M., Charan, K., and Xu, C. (2020). An adaptive excitation source for high-speed multiphoton microscopy. Nat. Methods *17*, 163–166.

Lieke, E.E., Frostig, R.D., Arieli, A., Ts'o, D.Y., Hildesheim, R., and Grinvald, A. (1989). Optical imaging of cortical activity: real-time imaging using extrinsic dye-signals and high resolution imaging based on slow intrinsic-signals. Annu. Rev. Physiol. *51*, 543–559.

Lim, S.T., Antonucci, D.E., Scannevin, R.H., and Trimmer, J.S. (2000). A novel targeting signal for proximal clustering of the Kv2.1 K+ channel in hippocampal neurons. Neuron *25*, 385–397.

Lin, M.Z., and Schnitzer, M.J. (2016). Genetically encoded indicators of neuronal activity. Nat. Neurosci. *19*, 1142–1153.

Lin, J.Y., Knutsen, P.M., Muller, A., Kleinfeld, D., and Tsien, R.Y. (2013). ReaChR: a red-shifted variant of channelrhodopsin enables deep transcranial optogenetic excitation. Nat. Neurosci. *16*, 1499–1508.

Liu, R., Li, Z., Marvin, J.S., and Kleinfeld, D. (2019). Direct wavefront sensing enables functional imaging of infragranular axons and spines. Nat. Methods *16*, 615–618.

Low, R.J., Gu, Y., and Tank, D.W. (2014). Cellular resolution optical access to brain regions in fissures: imaging medial prefrontal cortex and grid cells in entorhinal cortex. Proc. Natl. Acad. Sci. USA *111*, 18739–18744.

Lu, R., Sun, W., Liang, Y., Kerlin, A., Bierfeld, J., Seelig, J.D., Wilson, D.E., Scholl, B., Mohar, B., Tanimoto, M., et al. (2017). Video-rate volumetric functional imaging of the brain at synaptic resolution. Nat. Neurosci. *20*, 620–628.

Lu, R., Liang, Y., Meng, G., Zhou, P., Svoboda, K., Paninski, L., and Ji, N. (2020). Rapid mesoscale volumetric imaging of neural activity with synaptic resolution. Nat. Methods *17*, 291–294.

Maclaurin, D., Venkatachalam, V., Lee, H., and Cohen, A.E. (2013). Mechanism of voltage-sensitive fluorescence in a microbial rhodopsin. Proc. Natl. Acad. Sci. USA *110*, 5939–5944.

Madisen, L., Garner, A.R., Shimaoka, D., Chuong, A.S., Klapoetke, N.C., Li, L., van der Bourg, A., Niino, Y., Egolf, L., Monetti, C., et al. (2015). Transgenic mice for intersectional targeting of neural sensors and effectors with high specificity and performance. Neuron *85*, 942–958.

Mardinly, A.R., Oldenburg, I.A., Pégard, N.C., Sridharan, S., Lyall, E.H., Chesnov, K., Brohawn, S.G., Waller, L., and Adesnik, H. (2018). Precise multimodal optical control of neural ensemble activity. Nat. Neurosci. *21*, 881–893.

Marshel, J.H., Kim, Y.S., Machado, T.A., Quirin, S., Benson, B., Kadmon, J., Raja, C., Chibukhchyan, A., Ramakrishnan, C., Inoue, M., et al. (2019). Cortical layer-specific critical dynamics triggering perception. Science *365*, eaaw5202.

Mattis, J., Tye, K.M., Ferenczi, E.A., Ramakrishnan, C., O'Shea, D.J., Prakash, R., Gunaydin, L.A., Hyun, M., Fenno, L.E., Gradinaru, V., et al. (2011). Principles for applying optogenetic tools derived from direct comparative analysis of microbial opsins. Nat. Methods *9*, 159–172.

McCall, J.G., Qazi, R., Shin, G., Li, S., Ikram, M.H., Jang, K.-I., Liu, Y., Al-Hasani, R., Bruchas, M.R., Jeong, J.-W., and Rogers, J.A. (2017). Preparation and implementation of optofluidic neural probes for in vivo wireless pharmacology and optogenetics. Nat. Protoc. *12*, 219–237.

Modi, M.N., Daie, K., Turner, G.C., and Podgorski, K. (2019). Two-photon imaging with silicon photomultipliers. Opt. Express *27*, 35830–35841.

Mohr, M.A., Bushey, D., Aggarwal, A., Marvin, J.S., Kim, J.J., Marquez, E.J., Liang, Y., Patel, R., Macklin, J.J., Lee, C.-Y., et al. (2020). jYCaMP: an optimized calcium indicator for two-photon imaging at fiber laser wavelengths. Nat. Methods *17*, 694–697.

Nadella, K.M.N.S., Roš, H., Baragli, C., Griffiths, V.A., Konstantinou, G., Koimtzis, T., Evans, G.J., Kirkby, P.A., and Silver, R.A. (2016). Random-access scanning microscopy for 3D imaging in awake behaving animals. Nat. Methods *13*, 1001–1004.

Nakai, J., Ohkura, M., and Imoto, K. (2001). A high signal-to-noise Ca(2+) probe composed of a single green fluorescent protein. Nat. Biotechnol. *19*, 137–141.

Nandy, A., Nassi, J.J., Jadi, M.P., and Reynolds, J. (2019). Optogenetically induced low-frequency correlations impair perception. eLife *8*, e35123.

Nikolenko, V., Watson, B.O., Araya, R., Woodruff, A., Peterka, D.S., and Yuste, R. (2008). SLM Microscopy: Scanless Two-Photon Imaging and Photostimulation with Spatial Light Modulators. Front. Neural Circuits *2*, 5.

Okano, H. (2021). Current Status of and Perspectives on the Application of Marmosets in Neurobiology. Annu. Rev. Neurosci. *44*, 27–48.

Oron, D., Tal, E., and Silberberg, Y. (2005). Scanningless depth-resolved microscopy. Opt. Express *13*, 1468–1476.

Ota, K., Oisi, Y., Suzuki, T., Ikeda, M., Ito, Y., Ito, T., Uwamori, H., Kobayashi, K., Kobayashi, M., Odagawa, M., et al. (2021). Fast, cell-resolution, contiguous-wide two-photon imaging to reveal functional network architectures across multi-modal cortical areas. Neuron *109*, 1810–1824.e9.

Otis, J.M., Zhu, M., Namboodiri, V.M.K., Cook, C.A., Kosyk, O., Matan, A.M., Ying, R., Hashikawa, Y., Hashikawa, K., Trujillo-Pisanty, I., et al. (2019). Paraventricular Thalamus Projection Neurons Integrate Cortical and Hypothalamic Signals for Cue-Reward Processing. Neuron *103*, 423–431.e4.

Ouzounov, D.G., Wang, T., Wang, M., Feng, D.D., Horton, N.G., Cruz-Hernández, J.C., Cheng, Y.-T., Reimer, J., Tolias, A.S., Nishimura, N., and Xu, C. (2017). In vivo three-photon imaging of activity of GCaMP6-labeled neurons deep in intact mouse brain. Nat. Methods *14*, 388–390.

Owen, S.F., Berke, J.D., and Kreitzer, A.C. (2018). Fast-Spiking Interneurons Supply Feedforward Control of Bursting, Calcium, and Plasticity for Efficient Learning. Cell *172*, 683–695.e15.

Packer, A.M., Peterka, D.S., Hirtz, J.J., Prakash, R., Deisseroth, K., and Yuste, R. (2012). Two-photon optogenetics of dendritic spines and neural circuits. Nat. Methods *9*, 1202–1205.

Packer, A.M., Russell, L.E., Dalgleish, H.W.P., and Häusser, M. (2015). Simultaneous all-optical manipulation and recording of neural circuit activity with cellular resolution in vivo. Nat. Methods *12*, 140–146.

Papagiakoumou, E., de Sars, V., Oron, D., and Emiliani, V. (2008). Patterned two-photon illumination by spatiotemporal shaping of ultrashort pulses. Opt. Express *16*, 22039–22047.

Papagiakoumou, E., Anselmi, F., Bègue, A., de Sars, V., Glückstad, J., Isacoff, E.Y., and Emiliani, V. (2010). Scanless two-photon excitation of channelrhodopsin-2. Nat. Methods *7*, 848–854.

Park, J.E., Zhang, X.F., Choi, S.-H., Okahara, J., Sasaki, E., and Silva, A.C. (2016). Generation of transgenic marmosets expressing genetically encoded calcium indicators. Sci. Rep. *6*, 34931.

Parker, J.G., Marshall, J.D., Ahanonu, B., Wu, Y.-W., Kim, T.H., Grewe, B.F., Zhang, Y., Li, J.Z., Ding, J.B., Ehlers, M.D., and Schnitzer, M.J. (2018). Diametric neural ensemble dynamics in parkinsonian and dyskinetic states. Nature *557*, 177–182.

Patriarchi, T., Cho, J.R., Merten, K., Howe, M.W., Marley, A., Xiong, W.-H., Folk, R.W., Broussard, G.J., Liang, R., Jang, M.J., et al. (2018). Ultrafast neuronal imaging of dopamine dynamics with designed genetically encoded sensors. Science *360*, eaat4422.

Patriarchi, T., Mohebi, A., Sun, J., Marley, A., Liang, R., Dong, C., Puhger, K., Mizuno, G.O., Davis, C.M., Wiltgen, B., et al. (2020). An expanded palette of dopamine sensors for multiplex imaging in vivo. Nat. Methods *17*, 1147–1155.

Pégard, N.C., Mardinly, A.R., Oldenburg, I.A., Sridharan, S., Waller, L., and Adesnik, H. (2017). Three-dimensional scanless holographic optogenetics with temporal focusing (3D-SHOT). Nat. Commun. *8*, 1228.

Piatkevich, K.D., Bensussen, S., Tseng, H.-A., Shroff, S.N., Lopez-Huerta, V.G., Park, D., Jung, E.E., Shemesh, O.A., Straub, C., Gritton, H.J., et al. (2019). Population imaging of neural activity in awake behaving mice. Nature *574*, 413–417.

Piatkevich, K.D., Jung, E.E., Straub, C., Linghu, C., Park, D., Suk, H.-J., Hochbaum, D.R., Goodwin, D., Pnevmatikakis, E., Pak, N., et al. (2018). A robotic multidimensional directed evolution approach applied to fluorescent voltage reporters. Nat Chem Biol *14*, 352–360.

Picot, A., Dominguez, S., Liu, C., Chen, I.W., Tanese, D., Ronzitti, E., Berto, P., Papagiakoumou, E., Oron, D., Tessier, G., et al. (2018). Temperature Rise under Two-Photon Optogenetic Brain Stimulation. Cell Rep. *24*, 1243–1253.e5.

Pinto, L., and Dan, Y. (2015). Cell-Type-Specific Activity in Prefrontal Cortex during Goal-Directed Behavior. Neuron *87*, 437–450.

Piyawattanametha, W., Barretto, R.P.J., Ko, T.H., Flusberg, B.A., Cocker, E.D., Ra, H., Lee, D., Solgaard, O., and Schnitzer, M.J. (2006). Fast-scanning two-photon fluorescence imaging based on a microelectromechanical systems two- dimensional scanning mirror. Opt. Lett. *31*, 2018–2020.

Piyawattanametha, W., Cocker, E.D., Burns, L.D., Barretto, R.P., Jung, J.C., Ra, H., Solgaard, O., and Schnitzer, M.J. (2009). In vivo brain imaging using a portable 2.9 g two-photon microscope based on a microelectromechanical systems scanning mirror. Opt. Lett. *34*, 2309–2311.

Podgorski, K., and Ranganathan, G. (2016). Brain heating induced by near-infrared lasers during multiphoton microscopy. J. Neurophysiol. *116*, 1012–1023.

Prakash, R., Yizhar, O., Grewe, B., Ramakrishnan, C., Wang, N., Goshen, I., Packer, A.M., Peterka, D.S., Yuste, R., Schnitzer, M.J., and Deisseroth, K. (2012). Two-photon optogenetic toolbox for fast inhibition, excitation and bistable modulation. Nat. Methods *9*, 1171–1179.

Prevedel, R., Yoon, Y.-G., Hoffmann, M., Pak, N., Wetzstein, G., Kato, S., Schrödel, T., Raskar, R., Zimmer, M., Boyden, E.S., and Vaziri, A. (2014). Simultaneous whole-animal 3D imaging of neuronal activity using light-field microscopy. Nat. Methods *11*, 727–730.

Qian, Y., Piatkevich, K.D., Mc Larney, B., Abdelfattah, A.S., Mehta, S., Murdock, M.H., Gottschalk, S., Molina, R.S., Zhang, W., Chen, Y., et al. (2019). A genetically encoded near-infrared fluorescent calcium ion indicator. Nat. Methods *16*, 171–174.

Raymond, C.S., and Soriano, P. (2007). High-efficiency FLP and PhiC31 site-specific recombination in mammalian cells. PLoS ONE *2*, e162.

Remedios, R., Kennedy, A., Zelikowsky, M., Grewe, B.F., Schnitzer, M.J., and Anderson, D.J. (2017). Social behaviour shapes hypothalamic neural ensemble representations of conspecific sex. Nature *550*, 388–392.

Rickgauer, J.P., and Tank, D.W. (2009). Two-photon excitation of channelrhodopsin-2 at saturation. Proc. Natl. Acad. Sci. USA *106*, 15025–15030.

Rickgauer, J.P., Deisseroth, K., and Tank, D.W. (2014). Simultaneous cellular-resolution optical perturbation and imaging of place cell firing fields. Nat. Neurosci. *17*, 1816–1824.

Roberts, T.F., Hisey, E., Tanaka, M., Kearney, M.G., Chattree, G., Yang, C.F., Shah, N.M., and Mooney, R. (2017). Identification of a motor-to-auditory pathway important for vocal learning. Nat. Neurosci. *20*, 978–986.

Ronzitti, E., Conti, R., Zampini, V., Tanese, D., Foust, A.J., Klapoetke, N., Boyden, E.S., Papagiakoumou, E., and Emiliani, V. (2017). Sub-millisecond optogenetic control of neuronal firing with two-photon holographic photoactivation of Chronos. J. Neurosci. *37*, 10679–10689.

Rose, T., Goltstein, P.M., Portugues, R., and Griesbeck, O. (2014). Putting a finishing touch on GECIs. Front. Mol. Neurosci. *7*, 88.

Rumyantsev, O.I., Lecoq, J.A., Hernandez, O., Zhang, Y., Savall, J., Chrapkiewicz, R., Li, J., Zeng, H., Ganguli, S., and Schnitzer, M.J. (2020). Fundamental bounds on the fidelity of sensory cortical coding. Nature *580*, 100–105.

Rupprecht, P., Carta, S., Hoffmann, A., Echizen, M., Blot, A., Kwan, A.C., Dan, Y., Hofer, S.B., Kitamura, K., Helmchen, F., and Friedrich, R.W. (2021). A database and deep learning toolbox for noise-optimized, generalized spike inference from calcium imaging. Nat. Neurosci. *24*, 1324–1337.

Sabatini, B.L., and Tian, L. (2020). Imaging Neurotransmitter and Neuromodulator Dynamics In Vivo with Genetically Encoded Indicators. Neuron *108*, 17–32.

Sadakane, O., Masamizu, Y., Watakabe, A., Terada, S., Ohtsuka, M., Takaji, M., Mizukami, H., Ozawa, K., Kawasaki, H., Matsuzaki, M., and Yamamori, T. (2015). Long-Term Two-Photon Calcium Imaging of Neuronal Populations with Subcellular Resolution in Adult Non-human Primates. Cell Rep. *13*, 1989–1999.

Sakai, R., Repunte-Canonigo, V., Raj, C.D., and Knöpfel, T. (2001). Design and characterization of a DNA-encoded, voltage-sensitive fluorescent protein. Eur. J. Neurosci. *13*, 2314–2318.

Sawinski, J., Wallace, D.J., Greenberg, D.S., Grossmann, S., Denk, W., and Kerr, J.N.D. (2009). Visually evoked activity in cortical cells imaged in freely moving animals. Proc. Natl. Acad. Sci. USA *106*, 19557–19562.

Schwertner, M., Booth, M., and Wilson, T. (2004). Characterizing specimen induced aberrations for high NA adaptive optical microscopy. Opt. Express *12*, 6540–6552.

Scott, B.B., Thiberge, S.Y., Guo, C., Tervo, D.G.R., Brody, C.D., Karpova, A.Y., and Tank, D.W. (2018). Imaging Cortical Dynamics in GCaMP Transgenic Rats with a Head-Mounted Widefield Macroscope. Neuron *100*, 1045–1058.e5.

Scribner, J.L., Vance, E.A., Protter, D.S.W., Sheeran, W.M., Saslow, E., Cameron, R.T., Klein, E.M., Jimenez, J.C., Kheirbek, M.A., and Donaldson, Z.R. (2020). A neuronal signature for monogamous reunion. Proc. Natl. Acad. Sci. USA *117*, 11076–11084.

Seidemann, E., Chen, Y., Bai, Y., Chen, S.C., Mehta, P., Kajs, B.L., Geisler, W.S., and Zemelman, B.V. (2016). Calcium imaging with genetically encoded indicators in behaving primates. eLife *5*, e16178.

Sheintuch, L., Rubin, A., Brande-Eilat, N., Geva, N., Sadeh, N., Pinchasof, O., and Ziv, Y. (2017). Tracking the Same Neurons across Multiple Days in Ca^{2+} Imaging Data. Cell Rep. *21*, 1102–1115.

Shemesh, O.A., Tanese, D., Zampini, V., Linghu, C., Piatkevich, K., Ronzitti, E., Papagiakoumou, E., Boyden, E.S., and Emiliani, V. (2017). Temporally precise single-cell-resolution optogenetics. Nat. Neurosci. *20*, 1796–1806.

Shemesh, O.A., Linghu, C., Piatkevich, K.D., Goodwin, D., Celiker, O.T., Gritton, H.J., Romano, M.F., Gao, R., Yu, C.J., Tseng, H.-A., et al. (2020). Precision calcium imaging of dense neural populations via a cell body-targeted calcium indicator. Neuron *107*, 470–486.e11.

Shemetov, A.A., Monakhov, M.V., Zhang, Q., Canton-Josh, J.E., Kumar, M., Chen, M., Matlashov, M.E., Li, X., Yang, W., Nie, L., et al. (2021). A near-infrared genetically encoded calcium indicator for in vivo imaging. Nat. Biotechnol. *39*, 368–377.

Siegel, M.S., and Isacoff, E.Y. (1997). A genetically encoded optical probe of membrane voltage. Neuron *19*, 735–741.

Sjulson, L., and Miesenböck, G. (2007). Optical recording of action potentials and other discrete physiological events: a perspective from signal detection theory. Physiology (Bethesda) *22*, 47–55.

Skocek, O., Nöbauer, T., Weilguny, L., Martínez Traub, F., Xia, C.N., Molodtsov, M.I., Grama, A., Yamagata, M., Aharoni, D., Cox, D.D., et al. (2018). High-speed volumetric imaging of neuronal activity in freely moving rodents. Nat. Methods *15*, 429–432.

Sofroniew, N.J., Flickinger, D., King, J., and Svoboda, K. (2016). A large field of view two-photon mesoscope with subcellular resolution for in vivo imaging. eLife *5*, e14472.

Song, A., Charles, A.S., Koay, S.A., Gauthier, J.L., Thiberge, S.Y., Pillow, J.W., and Tank, D.W. (2017). Volumetric two-photon imaging of neurons using stereoscopy (vTwINS). Nat. Methods *14*, 420–426.

Soudais, C., Laplace-Builhe, C., Kissa, K., and Kremer, E.J. (2001). Preferential transduction of neurons by canine adenovirus vectors and their efficient retrograde transport in vivo. FASEB J. *15*, 2283–2285.

Sridharan, S., Gajowa, M., Ogando, M.B., Jagadisan, U., Abdeladim, L., Sadahiro, M., Bounds, H., Hendricks, W.D., Tayler, I., Gopakumar, K., et al. (2021). High performance microbial opsins for spatially and temporally precise perturbations of large neuronal networks. bioRxiv. https://doi.org/10.1101/2021.04.01.438134.

St-Pierre, F., Marshall, J.D., Yang, Y., Gong, Y., Schnitzer, M.J., and Lin, M.Z. (2014). High-fidelity optical reporting of neuronal electrical activity with an ultrafast fluorescent voltage sensor. Nat. Neurosci. *17*, 884–889.

Stamatakis, A.M., Schachter, M.J., Gulati, S., Zitelli, K.T., Malanowski, S., Tajik, A., Fritz, C., Trulson, M., and Otte, S.L. (2018). Simultaneous Optogenetics and Cellular Resolution Calcium Imaging During Active Behavior Using a Miniaturized Microscope. Front. Neurosci. *12*, 496.

Steinmetz, N.A., Aydin, C., Lebedeva, A., Okun, M., Pachitariu, M., Bauza, M., Beau, M., Bhagat, J., Böhm, C., Broux, M., et al. (2021). Neuropixels 2.0: A miniaturized high-density probe for stable, long-term brain recordings. Science *372*, eabf4588.

Stettler, D.D., Yamahachi, H., Li, W., Denk, W., and Gilbert, C.D. (2006). Axons and synaptic boutons are highly dynamic in adult visual cortex. Neuron *49*, 877–887.

Stirman, J.N., Smith, I.T., Kudenov, M.W., and Smith, S.L. (2016). Wide field-of-view, multi-region, two-photon imaging of neuronal activity in the mammalian brain. Nat. Biotechnol. *34*, 857–862.

Sun, F., Zhou, J., Dai, B., Qian, T., Zeng, J., Li, X., Zhuo, Y., Zhang, Y., Wang, Y., Qian, C., et al. (2020). Next-generation GRAB sensors for monitoring dopaminergic activity in vivo. Nat. Methods *17*, 1156–1166.

Szabo, V., Ventalon, C., De Sars, V., Bradley, J., and Emiliani, V. (2014). Spatially selective holographic photoactivation and functional fluorescence imaging in freely behaving mice with a fiberscope. Neuron *84*, 1157–1169.

Szalay, G., Judák, L., Katona, G., Ócsai, K., Juhász, G., Veress, M., Szadai, Z., Fehér, A., Tompa, T., Chiovini, B., et al. (2016). Fast 3D Imaging of Spine, Dendritic, and Neuronal Assemblies in Behaving Animals. Neuron *92*, 723–738.

Tang, S., Zhang, Y., Li, Z., Li, M., Liu, F., Jiang, H., and Lee, T.S. (2018). Large-scale two-photon imaging revealed super-sparse population codes in the V1 superficial layer of awake monkeys. eLife *7*, e33370.

Taniguchi, H., He, M., Wu, P., Kim, S., Paik, R., Sugino, K., Kvitsiani, D., Fu, Y., Lu, J., Lin, Y., et al. (2011). A resource of Cre driver lines for genetic targeting of GABAergic neurons in cerebral cortex. Neuron *71*, 995–1013.

Tervo, D.G.R., Hwang, B.-Y., Viswanathan, S., Gaj, T., Lavzin, M., Ritola, K.D., Lindo, S., Michael, S., Kuleshova, E., Ojala, D., et al. (2016). A Designer AAV Variant Permits Efficient Retrograde Access to Projection Neurons. Neuron *92*, 372–382.

Theer, P., and Denk, W. (2006). On the fundamental imaging-depth limit in two-photon microscopy. J. Opt. Soc. Am. A Opt. Image Sci. Vis. *23*, 3139–3149.

Theer, P., Hasan, M.T., and Denk, W. (2003). Two-photon imaging to a depth of 1000 microm in living brains by use of a Ti:Al2O3 regenerative amplifier. Opt. Lett. *28*, 1022–1024.

Thériault, G., De Koninck, Y., and McCarthy, N. (2013). Extended depth of field microscopy for rapid volumetric two-photon imaging. Opt. Express *21*, 10095–10104.

Thunemann, M., Lu, Y., Liu, X., Kılıç, K., Desjardins, M., Vandenberghe, M., Sadegh, S., Saisan, P.A., Cheng, Q., Weldy, K.L., et al. (2018). Deep 2-photon imaging and artifact-free optogenetics through transparent graphene microelectrode arrays. Nat. Commun. *9*, 2035.

Trautmann, E.M., O'Shea, D.J., Sun, X., Marshel, J.H., Crow, A., Hsueh, B., Vesuna, S., Cofer, L., Bohner, G., Allen, W., et al. (2021). Dendritic calcium signals in rhesus macaque motor cortex drive an optical brain-computer interface. Nat. Commun. *12*, 3689.

Tsai, P.S., Mateo, C., Field, J.J., Schaffer, C.B., Anderson, M.E., and Kleinfeld, D. (2015). Ultra-large field-of-view two-photon microscopy. Opt. Express *23*, 13833–13847.

Unger, E.K., Keller, J.P., Altermatt, M., Liang, R., Matsui, A., Dong, C., Hon, O.J., Yao, Z., Sun, J., Banala, S., et al. (2020). Directed Evolution of a Selective and Sensitive Serotonin Sensor via Machine Learning. Cell *183*, 1986–2002.e26.

Villette, V., Chavarha, M., Dimov, I.K., Bradley, J., Pradhan, L., Mathieu, B., Evans, S.W., Chamberland, S., Shi, D., Yang, R., et al. (2019). Ultrafast Two-Photon Imaging of a High-Gain Voltage Indicator in Awake Behaving Mice. Cell *179*, 1590–1608.e23.

Voigt, F.F., Chen, J.L., Krueppel, R., and Helmchen, F. (2015). A modular two-photon microscope for simultaneous imaging of distant cortical areas in vivo (Multiphoton Microscopy in the Biomedical Sciences XV).

Voleti, V., Patel, K.B., Li, W., Perez Campos, C., Bharadwaj, S., Yu, H., Ford, C., Casper, M.J., Yan, R.W., Liang, W., et al. (2019). Real-time volumetric microscopy of in vivo dynamics and large-scale samples with SCAPE 2.0. Nat. Methods *16*, 1054–1062.

Wagner, M.J., Kim, T.H., Kadmon, J., Nguyen, N.D., Ganguli, S., Schnitzer, M.J., and Luo, L. (2019). Shared Cortex-Cerebellum Dynamics in the Execution and Learning of a Motor Task. Cell *177*, 669–682.e24.

Wang, T., and Xu, C. (2020). Three-photon neuronal imaging in deep mouse brain. Optica *7*, 947.

Wang, K., Sun, W., Richie, C.T., Harvey, B.K., Betzig, E., and Ji, N. (2015). Direct wavefront sensing for high-resolution in vivo imaging in scattering tissue. Nat. Commun. *6*, 7276.

Wang, H., Jing, M., and Li, Y. (2018a). Lighting up the brain: genetically encoded fluorescent sensors for imaging neurotransmitters and neuromodulators. Curr. Opin. Neurobiol. *50*, 171–178.

Wang, M., Wu, C., Sinefeld, D., Li, B., Xia, F., and Xu, C. (2018b). Comparing the effective attenuation lengths for long wavelength *in vivo* imaging of the mouse brain. Biomed. Opt. Express *9*, 3534–3543.

Wang, T., Wu, C., Ouzounov, D.G., Gu, W., Xia, F., Kim, M., Yang, X., Warden, M.R., and Xu, C. (2020). Quantitative Analysis of 1300-nm Three-photon Calcium Imaging in the Mouse Brain. eLife *9*, e53205.

Watakabe, A., Ohtsuka, M., Kinoshita, M., Takaji, M., Isa, K., Mizukami, H., Ozawa, K., Isa, T., and Yamamori, T. (2015). Comparative analyses of adeno-associated viral vector serotypes 1, 2, 5, 8 and 9 in marmoset, mouse and macaque cerebral cortex. Neurosci. Res. *93*, 144–157.

Weisenburger, S., Tejera, F., Demas, J., Chen, B., Manley, J., Sparks, F.T., Martínez Traub, F., Daigle, T., Zeng, H., Losonczy, A., and Vaziri, A. (2019). Volumetric Ca^{2+} Imaging in the Mouse Brain Using Hybrid Multiplexed Sculpted Light Microscopy. Cell *177*, 1050–1066.e14.

Weiss, A.R., Liguore, W.A., Domire, J.S., Button, D., and McBride, J.L. (2020). Intra-striatal AAV2.retro administration leads to extensive retrograde transport in the rhesus macaque brain: implications for disease modeling and therapeutic development. Sci. Rep. *10*, 6970.

Wickersham, I.R., Lyon, D.C., Barnard, R.J.O., Mori, T., Finke, S., Conzelmann, K.-K., Young, J.A.T., and Callaway, E.M. (2007). Monosynaptic restriction of transsynaptic tracing from single, genetically targeted neurons. Neuron *53*, 639–647.

Wilt, B.A., Fitzgerald, J.E., and Schnitzer, M.J. (2013). Photon shot noise limits on optical detection of neuronal spikes and estimation of spike timing. Biophys. J. *104*, 51–62.

Wu, J., Liang, Y., Chen, S., Hsu, C.-L., Chavarha, M., Evans, S.W., Shi, D., Lin, M.Z., Tsia, K.K., and Ji, N. (2020). Kilohertz two-photon fluorescence microscopy imaging of neural activity in vivo. Nat. Methods *17*, 287–290.

Xu, H.-T., Pan, F., Yang, G., and Gan, W.-B. (2007). Choice of cranial window type for in vivo imaging affects dendritic spine turnover in the cortex. Nat. Neurosci. *10*, 549–551.

Xu, S., Yang, H., Menon, V., Lemire, A.L., Wang, L., Henry, F.E., Turaga, S.C., and Sternson, S.M. (2020). Behavioral state coding by molecularly defined paraventricular hypothalamic cell type ensembles. Science *370*, eabb2494.

Yamada, Y., Matsumoto, Y., Okahara, N., and Mikoshiba, K. (2016). Chronic multiscale imaging of neuronal activity in the awake common marmoset. Sci. Rep. *6*, 35722.

Yamahachi, H., Marik, S.A., McManus, J.N.J., Denk, W., and Gilbert, C.D. (2009). Rapid axonal sprouting and pruning accompany functional reorganization in primary visual cortex. Neuron *64*, 719–729.

Yang, W., and Yuste, R. (2017). In vivo imaging of neural activity. Nat. Methods *14*, 349–359.

Yang, G., Pan, F., Parkhurst, C.N., Grutzendler, J., and Gan, W.-B. (2010). Thinned-skull cranial window technique for long-term imaging of the cortex in live mice. Nat. Protoc. *5*, 201–208.

Yang, W., Miller, J.-E.K., Carrillo-Reid, L., Pnevmatikakis, E., Paninski, L., Yuste, R., and Peterka, D.S. (2016). Simultaneous Multi-plane Imaging of Neural Circuits. Neuron *89*, 269–284.

Yang, W., Carrillo-Reid, L., Bando, Y., Peterka, D.S., and Yuste, R. (2018). Simultaneous two-photon imaging and two-photon optogenetics of cortical circuits in three dimensions. eLife *7*, e32671.

Yang, M., Zhou, Z., Zhang, J., Jia, S., Li, T., Guan, J., Liao, X., Leng, B., Lyu, J., Zhang, K., et al. (2019). MATRIEX imaging: multiarea two-photon real-time in vivo explorer. Light Sci. Appl. *8*, 109.

Yanny, K., Antipa, N., Liberti, W., Dehaeck, S., Monakhova, K., Liu, F.L., Shen, K., Ng, R., and Waller, L. (2020). Miniscope3D: optimized single-shot miniature 3D fluorescence microscopy. Light Sci. Appl. *9*, 171.

Yao, S., Yuan, P., Ouellette, B., Zhou, T., Mortrud, M., Balaram, P., Chatterjee, S., Wang, Y., Daigle, T.L., Tasic, B., et al. (2020). RecV recombinase system for in vivo targeted optogenomic modifications of single cells or cell populations. Nat. Methods *17*, 422–429.

Yildirim, M., Sugihara, H., So, P.T.C., and Sur, M. (2019). Functional imaging of visual cortical layers and subplate in awake mice with optimized three-photon microscopy. Nat. Commun. *10*, 177.

Yuste, R. (2015). From the neuron doctrine to neural networks. Nat. Rev. Neurosci. *16*, 487–497.

Zeng, H.-H., Huang, J.-F., Chen, M., Wen, Y.-Q., Shen, Z.-M., and Poo, M.-M. (2019). Local homogeneity of tonotopic organization in the primary auditory cortex of marmosets. Proc. Natl. Acad. Sci. USA *116*, 3239–3244.

Zhang, Y., Rózsa, M., Liang, Y., Bushey, D., Wei, Z., Zheng, J., Reep, D., Broussard, G.J., Tsang, A., Tsegaye, G., et al. (2021). Fast and sensitive GCaMP calcium indicators for imaging neural populations. bioRxiv. https://doi.org/10.1101/2021.11.08.467793.

Zhang, F., Vierock, J., Yizhar, O., Fenno, L.E., Tsunoda, S., Kianianmomeni, A., Prigge, M., Berndt, A., Cushman, J., Polle, J., et al. (2011). The microbial opsin family of optogenetic tools. Cell *147*, 1446–1457.

Zhang, T., Hernandez, O., Chrapkiewicz, R., Shai, A., Wagner, M.J., Zhang, Y., Wu, C.-H., Li, J.Z., Inoue, M., Gong, Y., et al. (2019). Kilohertz two-photon brain imaging in awake mice. Nat. Methods *16*, 1119–1122.

Zhao, Y., Araki, S., Wu, J., Teramoto, T., Chang, Y.-F., Nakano, M., Abdelfattah, A.S., Fujiwara, M., Ishihara, T., Nagai, T., and Campbell, R.E. (2011). An expanded palette of genetically encoded Ca^{2+} indicators. Science *333*, 1888–1891.

Zhu, G., van Howe, J., Durst, M., Zipfel, W., and Xu, C. (2005). Simultaneous spatial and temporal focusing of femtosecond pulses. Opt. Express *13*, 2153–2159.

Zingg, B., Chou, X.-L., Zhang, Z.-G., Mesik, L., Liang, F., Tao, H.W., and Zhang, L.I. (2017). AAV-Mediated Anterograde Transsynaptic Tagging: Mapping Corticocollicular Input-Defined Neural Pathways for Defense Behaviors. Neuron *93*, 33–47.

Zipfel, W.R., Williams, R.M., and Webb, W.W. (2003). Nonlinear magic: multiphoton microscopy in the biosciences. Nat. Biotechnol. *21*, 1369–1377.

Ziv, Y., Burns, L.D., Cocker, E.D., Hamel, E.O., Ghosh, K.K., Kitch, L.J., El Gamal, A., and Schnitzer, M.J. (2013). Long-term dynamics of CA1 hippocampal place codes. Nat. Neurosci. *16*, 264–266.

Zong, W., Wu, R., Li, M., Hu, Y., Li, Y., Li, J., Rong, H., Wu, H., Xu, Y., Lu, Y., et al. (2017). Fast high-resolution miniature two-photon microscopy for brain imaging in freely behaving mice. Nat. Methods *14*, 713–719.

Zong, W., Wu, R., Chen, S., Wu, J., Wang, H., Zhao, Z., Chen, G., Tu, R., Wu, D., Hu, Y., et al. (2021). Miniature two-photon microscopy for enlarged field-of-view, multi-plane and long-term brain imaging. Nat. Methods *18*, 46–49.

Zou, P., Zhao, Y., Douglass, A.D., Hochbaum, D.R., Brinks, D., Werley, C.A., Harrison, D.J., Campbell, R.E., and Cohen, A.E. (2014). Bright and fast multicoloured voltage reporters via electrochromic FRET. Nat. Commun. *5*, 4625.